Alma Mater Studiorum · Università di Bologna

SCUOLA DI SCIENZE

Corso di Laurea Magistrale in Fisica

EFFICIENCY LIMITS FOR SILICON/PEROVSKITE TANDEM SOLAR CELLS: A THEORETICAL MODEL

Relatore:

Chiar.ma Prof.ssa
Beatrice Fraboni

Presentata da:

Lisa Redorici

Corelatore:

Chiar.mo Prof.
Lucio Claudio Andreani

Sessione II
Anno Accademico 2014/2015

To Mara and Roberto

Sommario

L'obiettivo della presente tesi di laurea magistrale è studiare l'estensione di un modello elettro-ottico analitico, nato per la descrizione di una cella solare costituita da un film sottile di silicio cristallino, alla descrizione della struttura tandem perovskite-silicio in presenza di light-trapping per determinarne i limiti di efficienza.
I materiali su cui si basa il modello analitico del presente lavoro sono silicio cristallino e una struttura a perovskite: metilammoniopiombotriiodato (MALI).
Le perovskiti sono tra i materiali più promettenti per il fotovoltaico, infatti la loro efficienza è cresciuta vertiginosamente dal loro primo utilizzo, nel 2009, al 2014, rendendole candidati ideali per le nuove sfide del solare fotovoltaico, oltre ai vantaggi forniti da una preparazione semplice e al basso costo con cui possono essere sintetizzate.
Inoltre, la texturizzazione delle strutture permette l'intrappolamento della radiazione nello strato di materiale attivo aumentando così l'assorbimento della luce.
Utilizzando il formalismo di Green si riesce a calcolare analiticamente il profilo di fotogenerazione di una struttura con un solo strato in presenza di light-trapping dovuto ad uno scatteratore Lambertiano. Qui se ne propone un avanzamento: lo studio analitico dell'accoppiamento ottico tra le due celle solari che costituiscono il tandem determinando il profilo di fotogenerazione nella struttura complessiva.
Si studia inoltre la modellizzazione elettronica del sistema, trattando la cella solare superiore in perovskite come un diodo ideale e descrivendo la cella di silicio risolvendo le equazioni di drift-diffusione. Per la struttura tandem è stata scelta una configurazione a 4 terminali.
L'obiettivo ultimo è il calcolo dei limiti di efficienza nel tandem, l'impatto dei vari meccanismi di ricombinazione e il ruolo del materiale della cella superiore (dipendenza dal band gap) per la progettazione di strutture ad alta efficienza: caratteristica imprescindibile per il futuro di questa tecnologia.
Il lavoro è supportato da una continua validazione dei risultati ottenuti tramite un confronto con il software numerico Silvaco-ATLAS nel tentativo di sviluppare un modello analitico indipendente e corretto per poi essere utilizzato per lo studio di strutture di questa tipologia.

Contents

Abstract

The primary goal of this work is related to the extension of an analytic electro-optical model. It will be used to describe single-junction crystalline silicon solar cells and a silicon/perovskite tandem solar cell in the presence of light-trapping in order to calculate efficiency limits for such a device.
In particular, our tandem system is composed by crystalline silicon and a perovskite structure material: metilammoniumleadtriiodide (MALI).
Perovskite are among the most convenient materials for photovoltaics thanks to their reduced cost and increasing efficiencies. Solar cell efficiencies of devices using these materials increased from 3.8% in 2009 to a certified 20.1% in 2014 making this the fastest-advancing solar technology to date.
Moreover, texturization increases the amount of light which can be absorbed through an active layer. Using Green's formalism it is possible to calculate the photogeneration rate of a single-layer structure with Lambertian light trapping analytically. In this work we go further: we study the optical coupling between the two cells in our tandem system in order to calculate the photogeneration rate of the whole structure. We also model the electronic part of such a device by considering the perovskite top cell as an ideal diode and solving the drift-diffusion equation with appropriate boundary conditions for the silicon bottom cell. We have a four terminal structure, so our tandem system is totally unconstrained.
Then we calculate the efficiency limits of our tandem including several recombination mechanisms such as Auger, SRH and surface recombination. We focus also on the dependence of the results on the band gap of the perovskite and we calculare an optimal band gap to optimize the tandem efficiency.
The whole work has been continuously supported by a numerical validation of out analytic model against Silvaco ATLAS which solves drift-diffusion equations using a finite elements method. Our goal is to develop a simpler and cheaper, but accurate model to study such devices.

Introduction

What are *solar cells*? The name refers to a technological device which is able to convert light into electrical power.
Nowadays there are several kinds of solar cells, which are based on different physical or chemical phenomena. Nevertheless, the most common kind of solar cell is based on semiconductors and in particular on silicon. Thanks to industrial improvements of microelectronics, silicon technology is the most competitive on a large scale; that is also why it is the most employed material as a semiconductor for photovoltaics.
Solar cells are based on the *photovoltaic effect* which was first reported by Edmund Bequerel in 1839 when he observed that the action of light on a silver coated platinum electrode immersed in electrolyte produced a potential difference. It is closely related to the photoelectric effect, whose explanation gave Einstein the Nobel prize in 1921. The latter consists of the extraction of electrons from a material as a consequence of the absorption of electromagnetic radiation. On the other hand, as far as the former is concerned, electrons and holes remain inside the material, they are not extracted, but they are just separated and this generates a potential difference. However, driving a current through a load after electron-hole pair generation requires an asymmetric structure. It took up to 1940 for the realisation of the first p-n junction with ultra pure Silicon, although the first solid state photovoltaic device, a Selenium cell with a very low efficiency ($\approx 1\%$), has already been realized in 1930-32 [1].
This kind of solar cells are known as *first generation* photovoltaic cells. They present a serious disadvantage connected with the Silicon's indirect gap: in order to maximize light absorption they should be very thick, around a few hundreds microns with a high impact on the final device cost.
To solve this problem, the *second generation* solar cells were born. They are typically based on thin-film materials with direct band gap, like $a - Si, CdTe, CuIn_{1-x}Ga_xSe_2$ [2] [3]. Despite their reduced thickness, they are not so efficient as the first generation cells because of a weaker absorption [4].
Nowadays the *third generation* solar cells are under investigation. They consist of multi-

junctions cells and other solutions to overcome the Shockley-Queisser limit[5] for single junction. The main idea is connected with different gap materials, allowing to absorb radiation selectively [6] [7] [8]. In particular, the top cell is required to absorb high-energy photons, whilst the other cells deal only with low frequency radiation. These are *tandem cells* and they allow us to go beyond the theoretical limit of Shockley-Queisser which is around 32.9% without losses for single junction [5] and around 42% without losses for double junction. New low cost materials with a higher band gap than Silicon are required to overcome the Shockley-Queisser limit for double junction solar cells giving new life to photovoltaic technology [9].

This entire work has been realized at the Department of Physics of the University of Pavia, in particular in cooperation with the Photonics and Nanostructures research group head by Professor Lucio Claudio Andreani.

In this thesis, an analytic electro-optical model to study solar cells is presented. It is used to describe both solar cells and tandem solar cells [10], although some modifications are required. Both single junction cells and tandem cells are studied including Lambertian light trapping [11] [12]. In addition several recombination mechanisms are taken into account in order to calculate the efficiency limits for tandems and to identify the principal sources of losses.
In chapter 1, general transport properties in semiconductors and silicon in particular are described. Several basic concepts on *pn* junctions and solar cells are also presented. At the end of this chapter there is a brief review on efficiency limits for solar cells.
In chapter 2 the analytic model is introduced to study the Silicon bottom cell. We start from the optical model of light harvesting the cell using the Poiynting vector's approach to calculate the carrier generation rate [13] and the Green's formalism is widely applied. Moreover, the drift-diffusion equations with such a source term are solved analytically and then the external quantum efficiency and the short-circuit current are calculated [14]. The dark current of such a device is obtained by considering the ideal diode equation, modified by taking into account both the finite thickness of the p-n solar cell and surface recombination. Then carrier densities, open circuit voltage and efficiency are calculated and their behaviour as a function of thickness is shown in several plots.
In the chapter 3 we move to tandem solar cells and also the perovskite top cell is presented [15]. Perovskite materials such as the methylammonium lead halides are cheap to produce and simple to manufacture. Solar cell efficiencies of devices using these materials have increased rapidly from 6% in 2009 to 20 % in 2014, making this the fastest-advancing solar technology to date. Their high efficiencies and low production costs make perovskite solar cells a commercially attractive option. The perovskite top cell is treated with a simple semi-empirical model,

which essentially follows ideal diode equation developed by Loper *et al.* [15] and using some experimental data published by Liu *et al.* [16] in 2014.
The optical coupling between the two cells is provided by applying the Green's formalisms to such a multilayered structure and using the same approach presented for the Silicon bottom cell [14]. In the this last chapter, this structure is deeply studied, providing the efficiency limits including finite thickness, SRH recombination, Auger recombination, surface recombination, band gap narrowing and the dependence of the efficiency on perovskite band gap.
In the very last chapter, we also developed a new analytic model for the silicon bottom cell which takes into account the effects of a finite voltage when we solve drift-diffusion equation to obtain the short-circuit current. It has already been implemented and its agreement with Silvaco becomes even better. This makes us confident in applying such a new improvement to the tandem model in order to get clearer and more precise results for efficiency limits.

Chapter 1

The physics of solar cells

In this first chapter there are two different sections: in the first one we present some basic definitions, properties for semiconductor transport and for p-n junctions, while in the second one we focus more on solar cells in general.

1.1 Semiconductor transport equations

1.1.1 Basic definition in semiconductor physics

At zero absolute temperature, a pure semiconductor is unable to conduct heat or electricity since all of its electrons are involved in bonding. As the temperature is raised, the electrons gain some kinetic energy from lattice vibrations and some of them are able to break free. The free electrons have been excited into the conduction band and now are able to travel and transport charge or energy. Meanwhile, the vacancies (holes) which they have left behind in the valence band are able to move and can also conduct. The higher the temperature, the higher the number of electrons and holes which are mobilised and the higher the conductivity. In a metal the current is due to the flow of negative charge (electrons), whereas the current in a semiconductor results from the motion of both electrons and holes, which appear as positive charges.
The minimum amount of energy which can promote an electron from the valence band to the conduction band is said *fundamental band gap* and it is indicated as E_g. There are two different situations: if the minimum of the conduction band (CB) and the maximum of valence band (VB) occur for the same $\mathbf{k}$, then a photon or a phonon of energy equal to E_g is sufficient to create an electron-hole pair. These materials are called *direct* band gap semiconductors and Gallium Arsenide is one of the most wide known examples [1].
Otherwise this mechanism is not possible, since promoting an electron to the bottom of the CB

will change its momentum, so a three-bodies interaction is needed in order to conserve momentum. This extra-amount of momentum is usually provided by a phonon, a lattice vibration, of the correct momentum value. This kind of semiconductor is called *indirect* band gap material and the most famous example is Silicon.
According to the Pauli exclusion principle, each quantum state can support only two electrons of different spin. Since each quantum state in a crystal is defined by a unique value of $\mathbf{k}$, there are only two electrons for each $\mathbf{k}$. Since for a wave function confined in a region of width L, $kL/2\pi$ must be an integer, a crystal of volume L^3 can support only $L/(2\pi)^3$ $\mathbf{k}$ states. Taking into account also spin degeneracy, the density of electrons states per unit crystal volume, $g(\mathbf{k})$ becomes:

$$g(\mathbf{k})d^3\mathbf{k} = \frac{2}{(2\pi)^3}d^3\mathbf{k} \tag{1.1.1}$$

If the band structure is isotropic, i.e. the dispersion relation only depends on the modulus of $\mathbf{k}$, the previous relation becomes:

$$g(\mathbf{k})d^3\mathbf{k} = g(\mathbf{k})4\pi\, k^2 dk \tag{1.1.2}$$

and in terms of energy it can be written as:

$$g(E)dE = g(\mathbf{k})4\pi\, k^2 \frac{dk}{dE}\, dE\ . \tag{1.1.3}$$

For the conduction band, the minimum of energy $E(\mathbf{k})$ occurs at $\mathbf{k} = 0$ or another vale of $\mathbf{k}$ corresponding to an important direction in the crystal.
Near to a minimum of energy at $\mathbf{k} = \mathbf{k}_{0c}$ it is convenient to expand the $E(\mathbf{k})$ in powers of $(\mathbf{k} - \mathbf{k}_{0c})$ so:

$$E(\mathbf{k}) = E_{c0} + \hbar^2 \frac{|\mathbf{k} - \mathbf{k}_{0c}|^2}{2m_c^*} \tag{1.1.4}$$

where $E_{c0} = E_c(\mathbf{k}_0)$ and m_c^* is a parameter with the dimensions of mass which is defined from the band structure by

$$\frac{1}{m_c^*} = \frac{1}{\hbar^2}\frac{\partial^2 E(k)}{\partial^2 k}\ . \tag{1.1.5}$$

This is the so called *parabolic approximation*. According to this, the density of states (DOS) in the conduction band is equal to

$$g(E_c) = \frac{1}{2\pi^2}\left(\frac{2m_c^*}{\hbar^2}\right)^{3/2}(E - E_{c0})^{1/2} \tag{1.1.6}$$

and in the same way we can obtain the valence band DOS

$$g(E_v) = \frac{1}{2\pi^2}\left(\frac{2m_v^*}{\hbar^2}\right)^{3/2}(E_{0v} - E)^{1/2} \ . \tag{1.1.7}$$

Following the previous definitions, the total density of electrons in a conduction band of minimum energy E_c is given by

$$n = \int_{E_c}^{\infty} g_c(E) f_0(E, E_F, T)\, dE \tag{1.1.8}$$

while the total density of holes in a valence band of maximum energy E_v is defined by

$$p = \int_{-\infty}^{E_v} g_v(E) f_0(E, E_F, T)\, dE \tag{1.1.9}$$

where $f_0(E, E_F, T)$ is the Fermi Dirac distribution function

$$f_0(E, E_F, T) = \frac{1}{e^{(E-E_F)/k_BT} + 1} \ . \tag{1.1.10}$$

For a semiconductor at absolute zero, the valence band is completely filled and the conduction band completely empty. This means that the Fermi level must lie somewhere in the band gap. At low temperature, k_bT is very small, thus, for the conduction band $E - E_F >> k_BT$ and $E_F - E >> k_BT$ in the valence band. Hence we can simply the Fermi Dirac distribution function as:

$$f_0(E, E_F, T) \approx e^{(E_F-E)/k_BT} \tag{1.1.11}$$

for the conduction band and

$$1 - f_0(E, E_F, T) \approx e^{(E-E_F)/k_BT} \tag{1.1.12}$$

for the valence band.
This is called *Boltzmann approximation* and it holds as long as $(E_c - E_F)/k_BT >> 1$ and $(E_F - E_v)/k_BT >> 1$, which are usually true for a semiconductor in equilibrium.
These approximations simplify the integrals in the expressions for n and p above. In the parabolic band approximation, using these relations n and p can be evaluated exactly and with a simple algebra, we find:

$$n(x) = N_c\, e^{(E_F(x)-E_c)/k_BT} \tag{1.1.13}$$

where N_c is called the effective conduction band density of states and it is given by

$$N_c = 2\left(\frac{m_c^* k_B T}{2\pi\hbar^2}\right)^{3/2} . \tag{1.1.14}$$

In the same way for hole density

$$p(x) = N_v\, e^{(E_v - E_F(x))/k_B T} \tag{1.1.15}$$

where N_v is called the effective valence band density of states and it is given by

$$N_v = 2\left(\frac{m_v^* k_B T}{2\pi\hbar^2}\right)^{3/2} . \tag{1.1.16}$$

These equations say that electron and hole densities vary exponentially according to the position of the Fermi level in the band gap.
Moreover, at a given temperature, the product between n and p is a constant

$$np = N_c N_v e^{-E_g/k_B T} \tag{1.1.17}$$

and this is used to define a specific constant property of the material, the *intrinsic carrier concentration* n_i

$$n_i^2 = np = N_c N_v e^{-E_g/k_B T} . \tag{1.1.18}$$

By definition, n_i is the density of electrons which are thermally excited into the CB of a pure semiconductor in thermal equilibrium.
Carrier transport in semiconductor devices, including pn junctions, can be described by the the following equations.
Poisson's equation:

$$\boldsymbol{\nabla} \cdot \epsilon \mathbf{E} = q(p - n + N_a - N_d) \tag{1.1.19}$$

and the set of drift-diffusion equations:
Continuity equations:

$$\frac{\partial n}{\partial t} = \frac{1}{q}\boldsymbol{\nabla} \cdot \boldsymbol{J}_n + G - R_n \tag{1.1.20}$$

$$\frac{\partial p}{\partial t} = -\frac{1}{q}\boldsymbol{\nabla} \cdot \boldsymbol{J}_p + G - R_p \tag{1.1.21}$$

where J_n is the electron current density, R_n is the electron recombination rate and q is the electronic charge. G is the carrier generation rate. The same quantities with p index refer to holes.

Transport equations:

$$\boldsymbol{J}_n = kT\mu_n \boldsymbol{\nabla} n + q\mu_n n\mathbf{E} \tag{1.1.22}$$

$$\boldsymbol{J}_p = -kT\mu_p \boldsymbol{\nabla} p + q\mu_p p\mathbf{E} \tag{1.1.23}$$

where μ_p and μ_n are the holes and electrons mobilities.
Current densities consist of two contributions: (1) the drift current (carriers are driven by the electric field $\mathbf{E}$), and (2) the diffusion current (carriers are driven by the concentration gradient).

1.1.2 Basic concepts on p-n junctions

The semiconductor which has been described so far is called *intrinsic*, a perfect crystal which does not contain any imperfection. The only energy levels permitted are related to the values of $\mathbf{k}$ which arise from the overlap of the atomic orbitals into crystal bands. These levels determine the position of the Fermi level in equilibrium and the density of carriers which can cross the band gap and conduce electricity. Conductivity is determined by

$$\sigma = q\mu_n n + q\mu_p p \tag{1.1.24}$$

where μ is the mobility of carriers and q is the electrical charge. At equilibrium $n = p = n_i$.
If the crystal is altered by introducing an impurity atom, this introduces bonds of different strength, hence it modifies the local distribution of the energy levels by inserting several localised electronic energy levels into the crystal. If these new energy levels are inside the band gap it can change the position of Fermi level and the carrier concentration. This tunable property is called *doping*.
For example, n type doping can be realized by inserting impurity atoms which possess excess electrons for the number of crystal bonds such as, for example, nitrogen and phosphorous in silicon. These impurities are called *donors* because they donate an extra electron to the lattice. This new electron is excluded from the strong directional covalent bonds hence it is much less bonded. The donor can be ionized easily and if at room temperature they are fully ionized $N_d >> n_i$, where N_d is the dopant density, the electron concentration is given by

$$n \approx N_d \tag{1.1.25}$$

and

$$p \approx n_i^2/N_d \tag{1.1.26}$$

following the mass action law.
The electron concentration has been rapidly increased and in this case the electrons are called *majority carriers* whereas holes are *minority carriers*.
On the other hand, if a crystal is doped with *acceptors* atoms such as B and Al, which have too few valence electrons, an additional electron is required to form covalent bonds. In this way one of these is excited and remove for the valence band leaving an additional hole. These p type semiconductors contain excess of positive carriers and, following the previous relations, we find:

$$p \approx N_a \tag{1.1.27}$$

and

$$n \approx n_i^2/N_a \tag{1.1.28}$$

and in this case holes are majority carriers.
The p-n homojunction is the most widely used device structure in photovoltaics. It consists of a single material layer with an inhomogeneous doping profile. It is usually grown on a metal substrate with a thin antireflection coating put on the top. Light enters from the top and in our case from the n-side, the emitter while on the bottom there is the p-side, called the base. The doping profile is the following:

$$\rho_{dop}(x) = N_d$$

in the n side and

$$\rho_{dop}(x) = N_a \tag{1.1.29}$$

in the p side.
By definition, a p-n junction is obtained when two different doped semiconductor layers are brought together. Mobile carriers can diffuse across the junction leaving a layer of fixed charges due to ionized fixed atoms. This gives rise to an electric field across the junction which opposes further diffusion of majority carriers. Equilibrium is obtained when diffusion of majority carriers is balanced by the drift of minority carriers in the electrostatic field.
In principle a p-n junction can be studied by solving a set of coupled differential equations for the electron and hole densities and for the electrostatic potential, but it is a complex problem which could be solved only numerically. On the other hand, with two approximations analytic solution can be obtained. These are the *depletion region approximation* and the approximation that recombination in the doped material is linear [1].
The built-in potential is due to the difference between the two work functions Φ_p and Φ_n of

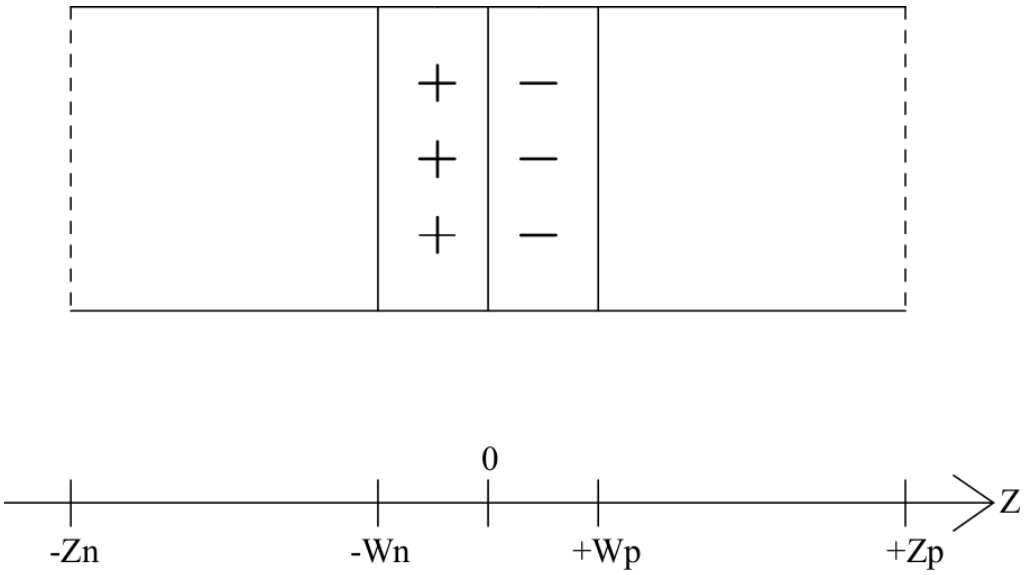

Figure 1.1.1: Infinite p-n junction

the p and n type materials and at this stage the junction region is depleted of carriers, the two Fermi levels are equal, whilst there is a step in the conduction and valence bands. Using some relations shown in the next section we can express V_{bi} as a function of the doping levels:

$$V_{bi} = \frac{1}{q}(\Phi_n - \Phi_p) = \frac{kT}{q} ln \left(\frac{N_a N_d}{n_i^2} \right) \tag{1.1.30}$$

If an external bias V is applied, it shifts the Fermi levels and the potential drop changes according to:

$$V_j = V_{bi} - V \ . \tag{1.1.31}$$

If V is a positive bias the potential barrier decreases and the depletion region is reduced until it is zero and then the asymmetry which gives rise to the photovoltaic effect is removed. On the other hand if there a negative applied bias it enhances the depletion layer. Now let us focus on the infinite p-n junction shown in fig. 1.1.1. According to Poisson's equation the electrostatic potential Φ must obey

$$\frac{d^2\Phi}{dz^2} = -\frac{q}{\epsilon_s} N_d \tag{1.1.32}$$

for $-w_n < z < 0$ and

$$\frac{d^2\Phi}{dz^2} = \frac{q}{\epsilon_s} N_a \tag{1.1.33}$$

for $0 < z < w_p$ and $z < W$, where ϵ_s is the permittivity of silicon.
According to the depletion region approximation, the potential varies only inside the space charge region, so the boundary conditions are:

$$\Phi = V_{bi} \tag{1.1.34}$$

at $z = -w_n$ and

$$\Phi = 0 \tag{1.1.35}$$

at $z = w_p$.
Integrating Poisson's equation then yields expression for the potential and eventually for the field:

$$\Phi = -\frac{N_a q}{2\epsilon_s}(z + w_n)^2 + V_{bi} \tag{1.1.36}$$

in the n side of the device and

$$\Phi = \frac{N_d q}{2\epsilon_s}(z - w_p)^2 \tag{1.1.37}$$

in the p side of the device. Imposing continuity we can calculate the width of the space charge region:

$$w_{scr} = w_p + w_n = \sqrt{\frac{2\epsilon_s V_{bi}}{q}\left(\frac{1}{N_a} + \frac{1}{N_d}\right)} \ . \tag{1.1.38}$$

Notice that the depleted width increases as either the p or the n doping is reduced.
In equilibrium there is no illumination and no applied bias, so the total current density must be equal to zero. The carrier populations obey

$$p(x) = N_a, \quad n(x) = n_0 \tag{1.1.39}$$

for the p side and

$$p(x) = p_0, \quad n(x) = N_d \tag{1.1.40}$$

for the n side, both with the condition $pn = n_i^2$.
If a positive bias is applied to the junction in the dark, the built in potential barrier is reduced and there is now a net current of electrons from n to p. There is also a net flux of holes from p to n. smaller amount of thermal energy is required to overcome the potential barrier across the junction, hence the flux of holes from p to n is increased and the same happens to electrons from the n side to the p side. In the dark we can make a reasonable assumption: there is no carrier generation and recombination in the SCR, hence the currents are constant here.
If this is so, in the steady state the total currents of electrons and holes, J_e and J_h will be constant across the depletion layer. Consequently, in the expression $J = -eJ_e + eJ_h$ for the

total current, we may separately evaluate the two contributions at whatever point along the depletion layer it is most convenient to do so. The most convenient point for the electron current is at the boundary between the depletion layer and the diffusion region on the p-side, and the most convenient point for the hole current is at the other boundary. We therefore write:

$$J = -eJ_e(w_n) + eJ_h(h) \tag{1.1.41}$$

This is useful because at the boundaries between the depletion layer and the diffusion regions the minority carrier currents are purely diffusive. Consequently, if we could calculate the position dependence of the minority carrier densities within the diffusion regions, we could immediately compute their currents, using (with $E = 0$ because according the depletion region approximation there is no electric field in the quasi neutral regions):

$$J_e = qD_e \frac{dn}{dx}|_{z=w_p} \tag{1.1.42}$$

and

$$J_h = -qD_h \frac{dp}{dx}|_{z=-w_n}. \tag{1.1.43}$$

Taking into account the continuity equation for steady states eq. 1.1.20 and eq. 1.1.21 and the modified mass action low under bias, which imposes (for electrons):

$$n \propto n_i^2 e^{qV/KT} \tag{1.1.44}$$

we can calculate the total current density and we obtain the well-known relation for infinite p-n junctions in the dark:

$$J_{dark} = J_0 \left(exp\left(\frac{qV}{kT}\right) - 1 \right) \tag{1.1.45}$$

where J_0 is called *reverse saturation current* and for infinite ideal diode equation it can be expressed as:

$$J_0 = qn_i^2 \left(\frac{D_e}{L_e N_a} + \frac{D_h}{L_h N_d} \right). \tag{1.1.46}$$

When the junction is illuminated, light creates electron-hole pairs in all three regions. The effect of illumination causes photogenerated holes to build up in the p side and electrons in the n side, shifting the Fermi levels in the same sense as a positive applied bias. Carrier densities n and p are then enhanced above their equilibrium values, and the electron and hole quasi Fermi levels are split. In low-level injection conditions, majority carriers density is almost unchanged by photogeneration, but minority carriers density is increased. Minority carriers diffuse along the quasi neutral region up to the space charge region edge, then the electric field

at the junction separates the pairs by driving minority carriers across the junction. In this way the reverse saturation current is increased because of minority carriers. If we connect a load to this device we could extract power according to $P = RI$ and in this way a p-n junction acts as a photovoltaic device.
Now we can move towards solar cells and we will see that a very useful approximation is applied to describe illuminated *pn* junction to study dark and illuminated current separately.
In the next chapter we will work on a finite p-n junction solar cell and we will present a new structure with a new reference frame.

1.2 Photovoltaic cells and power generation

1.2.1 General definitions

In order to study tandem cells, which are the object of this work, several definitions are required [1]. When the cell is illuminated, a potential different is produced and it gives rise to an electric current, the so-called *photo-generated* current. When a generic bias is applied, there is also a *dark current*. The former is due to electron-hole pairs which are generated in the whole active material and are drifted by the electric field created across the junction by different doping. The latter is created by the applied voltage, thanks to majority carriers from dopants. These two electric currents have two different signs: the photo generated current flows from the n-side to the p-side, on the contrary, under forward applied bias, the dark current flows from the p-side to the n-side. In solar cells technology, the *superposition principle* is supposed to be valid. Hence, the total current is equal to:

$$J_{tot}(V) = J_{pg}(V) - J_{dark}(V) \tag{1.2.1}$$

Since the photogenerated current is due to electric carriers generated by photon absorption, it is useful to define the *external quantum efficiency* as the probability that an incident photon of energy E will deliver one electron to the external circuit. It is implicitly defined by:

$$J_{pg}(V) = q \int b(E) QE(E, V)\, dE \tag{1.2.2}$$

where q is the elementary charge and $b(E)$ is the photon flux per unit energy. The photon flux per unit energy is obtained by the AM 1.5 spectrum [17] and it is reported in fig. 1.2.1. On passing through the atmosphere, light is absorbed and scattered by various atmospheric constituents, so that is the shape of the spectrum. Attenuating by the atmosphere is quantified by the 'air mass' factor. The standard 'air mass' is 1.5, corresponding to the sun being at

an angle of elevation of 42 degrees, for temperate latitudes. If the photogenerated current is

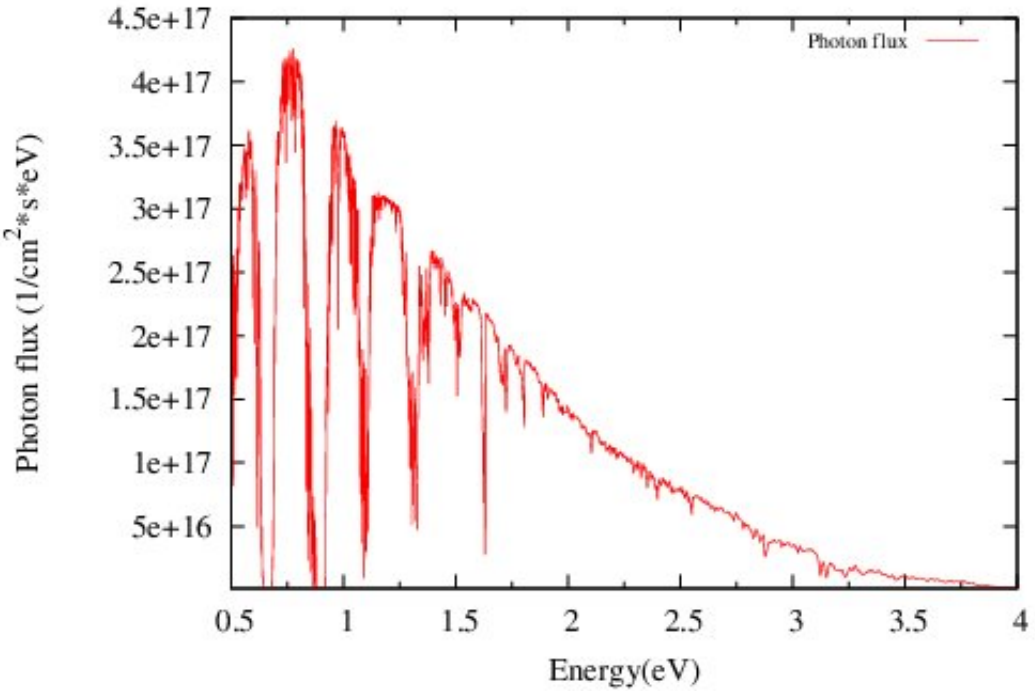

Figure 1.2.1: Photon flux.

calculated at $V = 0$, it is called *short circuit* current. Indeed, it is the current which flows in the electric circuit when the two terminals of the solar cell are connected together and there is no load. Moreover, there is an additional approximation: the J_{sc} is assumed to be bias independent. This is called *superposition approximation* and eq. 1.2.1 becomes:

$$J_{tot}(V) = J_{sc} - J_{dark}(V) \tag{1.2.3}$$

Since J_{sc} does not depend on bias, $QE(E)$ is bias-independent too. On the other hand, J_{dark} strongly depends on voltage. It can be interpreted as the current which flows in a solar cell when it is not illuminated. Although it is a dark current, it has an important role also under illumination. Several parameter like V_{oc}, FF and η are related to the J_{dark}, as we discuss now. It is clear that when the circuit is not connected to a bias the total current which flows must be equal to zero, then the following relation holds:

$$J_{pg}(V_{oc}) - J_{dark}(V_{oc}) = 0 \tag{1.2.4}$$

and V_{oc} is implicitly defined as the voltage developed by an illuminated solar cell with isolated terminals. To study the physics of a solar cell it is important to know the $J-V$ characteristic of such a device. By definition, the electrical power developed by an electronic device is:

$$P(V) = J(V)V \ . \tag{1.2.5}$$

Since we are interested in how to extract maximum power from a solar cell, the circuit's

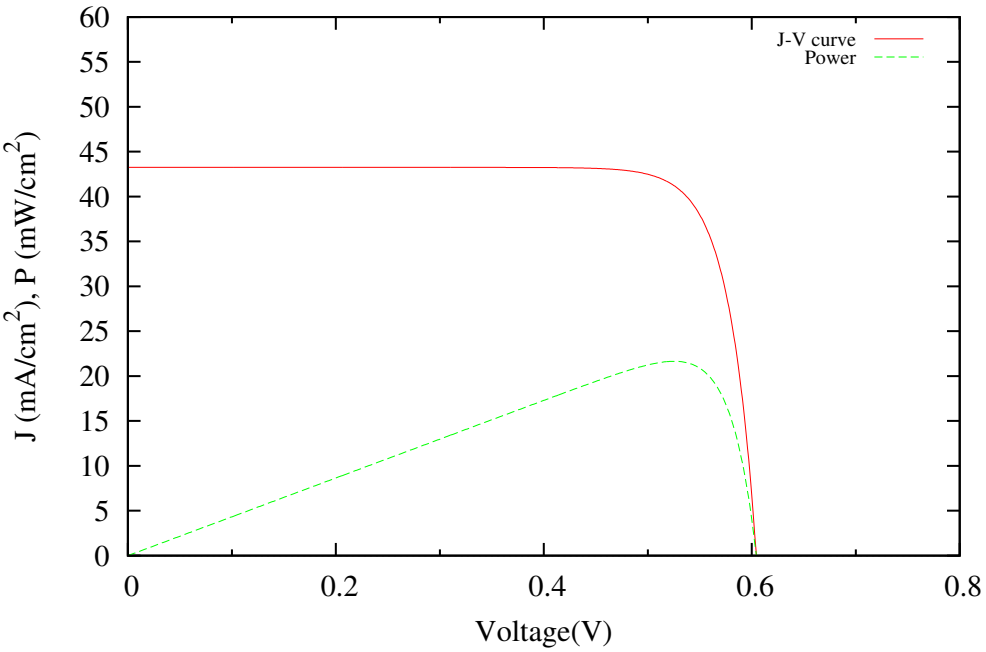

Figure 1.2.2: J-V curve and Power Density for a solar cell.

operating point must be the *maximum power point* $(J_m; V_m)$ (see fig. 1.2.2).
The J-V characteristic shows that the current-voltage product is positive and the cell generates power when voltage goes from 0 to V_{oc}. At $V < 0$ the illuminated device acts a photodetector, consuming power to generate a photocurrent. At $V > V_{oc}$ the device consumes power, this is the regime where light emitting diodes (LEDs) work.
Just to compare different cells' performances, there is another important quantity which should be defined: the *fill factor* FF. It is given by:

$$FF = \frac{J_m V_m}{J_{sc} V_{oc}} \ . \tag{1.2.6}$$

From a graphic point of view, it is defined as the ratio between the rectangle whose sides are set by the J_m and V_m (maximum power point coordinates) and another rectangle with J_{sc} and

V_{oc} instead of the previous values. The higher the fill factor, the higher the cell's performance. In conclusion, the *efficiency* can be defined as the ratio between the power at the operating point and the incident energy flux as follows:

$$\eta = \frac{J_m V_m}{P_s} \tag{1.2.7}$$

where P_s is given by:

$$P_s = \int b(E) E \, dE. \tag{1.2.8}$$

The spectral photons flux $b(E)$ is displayed in fig. 1.2.1.
In the theoretical limit of a device which absorbs every photon of energy equal or above the energy gap, all pairs are split and collected and do not recombine radiatively, the maximum efficiency is around 33% [5].
One method to increase the efficiency of a solar cell is to split the spectrum and use a solar cell that is optimised to each section of the spectrum. These are tandem solar cells which can either be individual cells with a mechanical stacking which can be connected in series. Series connected cells are simpler to fabricate but the current is the same though each cell so this constrain the band gaps that can be used. The most common arrangement for tandem cells is to grow them monolithically so that all the cells are grown as layers on the on substrate and tunnel junctions connect the individual cells. Currently, the best lab examples of traditional crystalline silicon solar cells have efficiencies between 20% and 25%,while lab examples of multi-junction solar cells based of III-V compounds have demonstrated performance over 45% according to the National Renewable Laboratories (NREL). Commercial examples of tandem, two layer, cells are widely available at 30% under one-sun illumination and improve to around 40% under concentrated sunlight. However, this efficiency is gained at the cost of increased complexity and manufacturing price.

1.2.2 Limits to energy conversion efficiency

Efficiency is a fundamental parameter to access the solar cell performance. In this work we are going to present the calculations of efficiency for a particular silicon/perovskite tandem solar cell, which is the goal of this thesis. To put these results into a context, in this subsection we derive the limits for energy conversion efficiency.
At first, we focus only on the efficiency limits for a single junction solar cell, but after that we will move toward tandem. We start by considering the Shockley-Queisser limit (derived from detailed balance [5]), which gives rise to the maximum efficiency as a function of the energy

band gap of the absorber. Then, we consider silicon solar cell and hence Auger losses, which are intrinsic mechanisms which impact on efficiency.

The Shockley-Queisser limit

In order to calculate the Shockley-Queisser limit we only assume radiative recombination as the only recombination mechanism. We also assume the superposition approximation so we can write:

$$J(V) = J_{sc} - J_{dark}(V) = J_{sc} - J_0 \left[exp\left(\frac{qV}{kT}\right) - 1 \right] \tag{1.2.9}$$

where $J_{dark}(V)$ is the $J - V$ characteristic of a solar cell in the dark, and J_0 is the reverse saturation current of an ideal diode. It is given by:

$$J_0 = qF_a \int_{E_g}^{\infty} A(E)b(E)QE(E)\, dE \tag{1.2.10}$$

where $F_a = \pi$ is the geometrical factor, which is related to the integration of the photon flux at the cell interface over a hemisphere. In addition, $b(E)$ is the photon flux density related to the black-body radiation of the cell in the dark

$$b(E) = \frac{2}{h^3c^2} \frac{E^2}{exp\left(\frac{E}{kT}\right) - 1}. \tag{1.2.11}$$

To obtain the Shockley-Queisser limit need making several assumptions to calculate the short-circuit current:

- step-like absorption, namely $A(E) = 0$ below the band gap and $A(E) = 1$ above the band gap, and the fact that
- all absorbed photons contribute to the photocurrent.

With these assumptions the only variable which efficiency depends on is the band gap, therefore in the short-circuit current, because of

$$\eta = \frac{J_m V_m}{P_s} \quad . \tag{1.2.12}$$

The ultimate limit to efficiency (without radiative recombination) as a function of the energy band gap is shown in the fig. 1.2.3. With all the assumptions made above, the power conversion efficiency is a function only of the energy gap and the incident spectrum. If the spectrum is

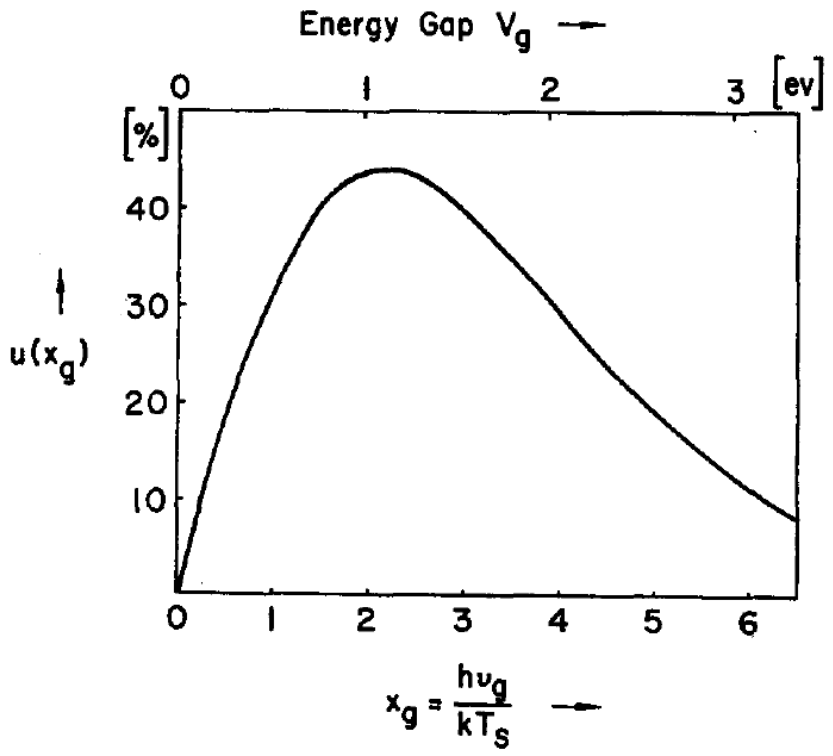

Figure 1.2.3: Shockley-Queisser curve for the ultimate limit to efficiency (no radiative recombination) [5].

fixed, the efficiency depends only on the band gap. Both very large and small energy gaps will lead to low efficiency: the former gives a too small photocurrent, the latter a too small open circuit voltage. For each spectrum there is an optimal band gap. Remembering that

$$V_{oc} = \frac{kT}{q} log\left(\frac{J_{sc}}{J_0} + 1\right) \tag{1.2.13}$$

the optimal band gap results from the opposite trends of J_{sc} and V_{oc}.
Following detailed balance calculations (including radiative recombination as imposed by thermodynamics), the efficiency for silicon solar cells ($E_g = 1.1eV$) is calculated to be 32.9%. This is usually called the detailed-balance or Shockley-Queisser limit to the conversion efficiency.

Efficiency limits including Auger recombination

In the previous subsection we quoted the SQ limit for silicon solar cells to be 32.9%. The current record efficiency (25.6%) [18] is below this limit. This is due to an additional intrinsic loss mechanism, Auger recombination, and to extrinsic losses. It will be described in details in

subsection 2.2.2, anyway here we will use a particular recombination rate to calculate the dark current and therefore the efficiency limits in the presence of Auger recombination. In order to reach our aim we change the way used to calculate J_{dark}

$$J(V) = J_{sc} - J_{dark}(V) = J_{sc} - qW \cdot R \tag{1.2.14}$$

where W is the thickness of the solar cell and R is the Auger recombination rate. It will be discussed in subsection 2.2.2. Moreover, the step function absorption is substituted by Lambertian limit, which we will discuss at the beginning of the next chapter.
Now efficiency is a function of the thickness and the maximum efficiency for silicon solar cell is reduced by nearly 3% and it drops to 30%. If several additional phenomena are included, such as Coulomb-enhanced Auger recombination and band gap narrowing [19], the maximum efficiency is further reduced to around $29.1 - 29.4\%$ [20].
A review of the efficiency limits of silicon solar cells is given in [21], [20], [22]. The limits reported in the literature are usually calculated using the idealized diode equation [1]. We know that the current efficiency record for silicon standalone solar cells is 25.6%, so quite close to the theoretical limit including radiative and Auger recombination [23] [24] [25] [26] [27].
That is why we are going to study silicon/perovskite tandem solar cells.
Therefore, in order to approach or overcome an efficiency target around 30%, it is not sufficient to improve the structure or the material properties of silicon solar cells and new approaches are required. This is why we are going to study silicon/perovskite tandem solar cells, which belong to the class of two-junction solar cells with thermodynamic efficiency limit around 42.9% according to detailed balance.
The most efficient tandem cell produced to date has an efficiency around 31.3% [28] and it is based on III-V compounds. This strongly suggests that complementing a high-efficiency silicon solar cell with a top cell made of a higher band gap material is a promising approach to overcome 30% efficiency using silicon-based technology.

Summary

In this first chapter, we have described the theory of an infinite p-n junction.
We have given a few basic definitions concerning solar cells such as the energy conversion efficiency.
We also have focused on what limits efficiency presenting two of the most significant limiting factors: thermodynamics and Auger intrinsic losses.n

Chapter 2

Silicon solar cell

2.1 Optics of textured solar cell and Lambertian limit

Managing light is one of the most interesting challenges related to photovoltaics of the last years [29] [18] [11]. The main reason is that by increasing the absorbed photon rate per unit volume, we decrease the amount of material needed for a certain absorption of light [30] [27] [31]. This means a significant reduction of costs per unit of energy converted, since the cost of the active material is one of the most important issues. About 30 years ago, light trapping by texturing surfaces has been introduced as a way of increasing the infrared absorption of thin silicon photodetectors. In the early 80s, Yablonovitch *et al* [32]. described schemes based on randomising light directions in solar cells, by using diffusely scattering (Lambertian) surface textures.

Although the Lambertian case can be precisely formulated, analytic solutions do not seem to have been described before [13] and [33]. In the past, approximations valid in the weak absorption limit have been used for Lambertian schemes. Exact analytical solutions are described in [13] and [33] and used to deduce a simple analytical formula that applies to both weakly and strongly absorbed light.

A possible Lambertian light-trapping [34] [35] [36] [37] scheme is shown in fig. 2.1.1. It is a p-n junction solar cell. The front surface is textured and it allows light to be randomized and thus it increases the absorption. There is also a silver back reflector to obtain a double light pass inside the device. In the surface region, it is possible to equate the difference between downward and upward fluxes, both outside and inside the device:

$$\Phi^{+} - \Phi^{-} = \Phi_{ext} - [R_{ext}\Phi_{ext} + (1 - R_f)\Phi^{-}] \tag{2.1.1}$$

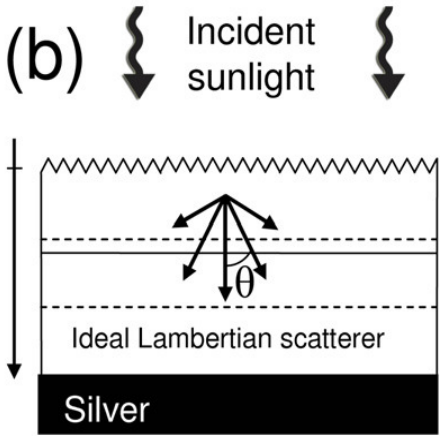

Figure 2.1.1: Lambertian light trapping configuration.

where R_{ext} is the appropriately weighted initial surface reflection of the external flux Φ_{ext} and R_f is that of the internal upward flux from the top surface. A second equation relates Φ^+ and Φ^-

$$\Phi^- = R_b T^+ T^- \Phi^+ \tag{2.1.2}$$

where R_b is the appropriately weighted rear surface reflectance, T^+ is the fraction of Φ^+ transmitted to the rear surface and T^- is the fraction of Φ^- reflected from the rear surface and transmitted to the front surface.

Carrier generation rate

As far as Lambertian light trapping is concerned, the Poynting vector in the structure is the sum of two contributions; a hemispherical, downward propagating power flux, and the other corresponding flux for upward propagation. As a consequence, interference terms do not appear in the carrier generation rate [13]. After averaging over the two polarization states and over all propagation directions inside the silicon, g may be written as [14]

$$g(z,E) = -[\frac{1}{\Phi_{ext}} \frac{d}{dz}(\Phi^+ - \Phi^-)]\Phi_{AM1.5}(E)\,. \tag{2.1.3}$$

If $R_{ext} = 0$ and considering $R_f = \dfrac{1}{n^2}$,

$$\Phi^+ - \Phi^- = \Phi_{ext} - (1 - R_f)\Phi^- = \Phi_{ext} - (1 - \frac{1}{n^2})\Phi^-\,. \tag{2.1.4}$$

In the limit of weakly absorbed light, the originally randomised angular light distribution retains its angular distribution in the double pass across the device, with the average ray travelling a distance equal to four times the device thickness W (there are the double pass and a factor 2 which arises from the integral of $\cos\theta$ over a hemisphere). This leads to the approximation [13]

$$T^+T^- = e^{4\alpha W}\Phi^+ \tag{2.1.5}$$

and with a very simple algebra we obtain:

$$\Phi_0^+ = \frac{\Phi_{ext}}{1 - R_b e^{4\alpha W}\left(1 - \frac{1}{n^2}\right)}$$

$$\Phi_0^- = \frac{R_b e^{4\alpha W}\Phi_{ext}}{1 - R_b e^{4\alpha W}\left(1 - \frac{1}{n^2}\right)} \tag{2.1.6}$$

at $z = 0$.
Considering the dependence on z

$$\Phi^+(z, E) = \Phi_0^+ e^{-\alpha z}$$

$$\Phi^-(z, E) = \Phi_0^- e^{\alpha z} \tag{2.1.7}$$

and according to eq. 2.1.3 we can now calculate the corresponding carrier generation rate. However, the light is increasingly concentrated in directions perpendicular to the surface as it propagates across the device. The average pathlength becomes less then $4W$ as absorption increases, hence, the above approximation always underestimates transmission and hence overestimates absorptance.

Analytic solution and Asymptotic behaviour

Instead of studying the exact lambertian limit numerically, we can determine the asymptotic behaviour by means of Green's improved approximated solution [13].
An effective optical thickness W_{op} can be defined:

$$T_a = e^{-\alpha W_{op}} \tag{2.1.8}$$

where the value of W_{op} can be obtained by taking into account the infinite sum of the optical events inside the layer which, for weak absorption, simplifies approaching twice the device thickness.

However, the asymptotic solution shows that W_{op} can be described by a relation of the form:

$$W_{op}/W = \frac{(2+x)}{(1+x)} \tag{2.1.9}$$

where x is a function of αW which is zero when αW is small and approaches infinity as αW becomes large. One of the simplest such functions takes the form:

$$x = a(\alpha W)^b \tag{2.1.10}$$

and a good fit to the analytic solution is obtained when $a = 0.935$ and $b = 0.67$.
In this way we obtain a different carrier generation rate which is:

$$g(z,E) = [\frac{\alpha_{lt}(R_b e^{2\alpha_{lt}W} e^{\alpha_{lt}z} + e^{-\alpha_{lt}z})\Phi_{AM1.5}(E)}{1 - R_b e^{2\alpha_{lt}W}\left(1 - \frac{1}{n^2}\right)}] \ . \tag{2.1.11}$$

where

$$\alpha_{lt} = \alpha \cdot \frac{W_{op}}{W} \tag{2.1.12}$$

which is called *light-trapping absorption coefficient.*
This is our carrier generation rate which will be used as the source term for diffusion equations. It takes into account both double pass absorption and randomizing light due to the texture of the front surface. In the next section we will present diffusion equations for electrons and holes including the effects of photogeneration which can be considered thanks to the carrier generation rate.

2.2 Charge transport

We have already shown that from the electronic point of view, the J-V chacteristic of a p-n junction can be calculated by assuming two approximations. The potential is dropped entirely across the junction which is free of carriers and the minority carrier recombination is linear in the carrier density. In this way the cell can be divided into three layers where the different contribution to the current can be treated separately. In both quasi-neutral regions the photocurrent comes from minority carriers and can be derived by solving the diffusion equations taking into account the continuity equation. Following our main approximation, these equations simplify when the electric field is equal to zero.
On the contrary, in the space charge region majority carriers produce current and generation and recombination should be taken into account.

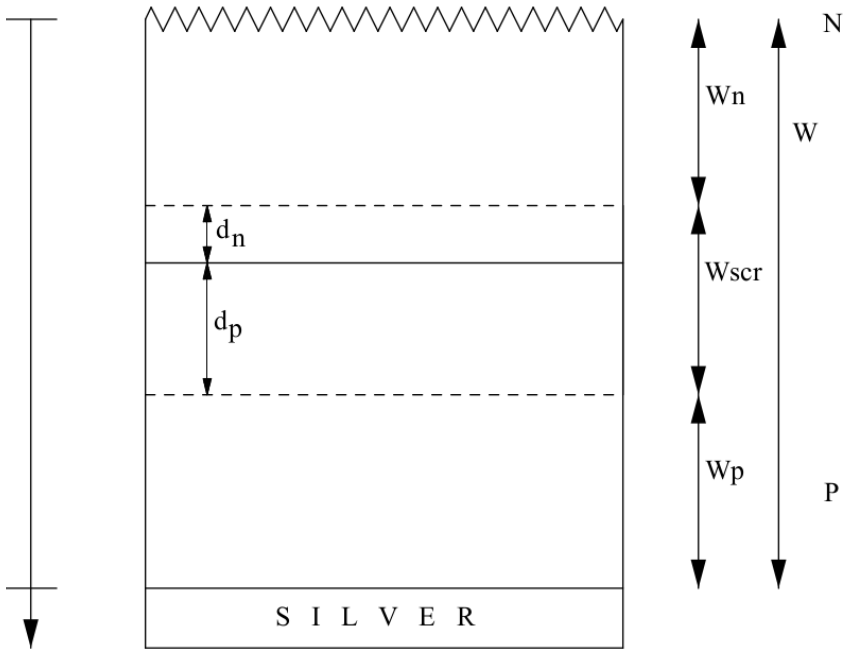

Figure 2.2.1: Solar cell with our reference frame. The total thickness of the cell is given by w, while w_{scr} refers to the thickness of the space charge region. W_n and W_p are the thickness of the quasi neutral n and p region respectively. With d_p and d_n we refer to the thickness of the p-side and n-side space charge region.

Following the superposition approximation, the total current voltage characteristic is the sum of two contributions: illumination and dark current. We already know how to calculate the J_{dark} for an infinite pn junction, so our primary goal is to calculate the J_{sc}. Then we should modify the dark current for a finite size junction.

2.2.1 Analytic solution of the drift-diffusion equations

Let us first present the structure of our solar cell and fix a specific reference frame. In fig. 2.2.1 a schematic representation of a p-n junction solar cell with textured front surface and silver back reflector is shown. The origin of the reference frame is put at the interface between air and silicon. The space charge region is shown between dotted lines whilst the other two layers are the quasi neutral n and p regions. With d_p and d_n we refer to the thickness of the p-side and n-side space charge region respectively. Before discussing the analytic model, we present all the physical parameters of the studied structure. It is a p-n junction of doped silicon with $N_a = 1 \cdot 10^{16} cm^{-3}$, $N_d = 1.5 \cdot 10^{18} cm^{-3}$, $n_{i,0} = 9.65 \cdot 10^{9} cm^{-3}$ before band gap narrowing according to [19]. The diffusion length in the emitter is fixed to $L_n = 20 \mu m$ and we use optical

data for silicon by Green. The diffusion length in the base varies in order to point out different physical aspects.

The first step of modelling is the analytic solution of the diffusion equations for minority carriers [14].

The presence of illumination impacts more minority carrier density then majority one. Hence, for electrons in the p region, which represent the most important contribution to photocurrent, and with no electric field neither from applied voltage nor from potential drop across the junction, we have

$$D_p \frac{d^2 \Delta n}{dz^2} - \frac{\Delta n}{\tau_p} + g(z, E) = 0 \tag{2.2.1}$$

where D_p is the diffusion constant in the p side, τ_p is the electrons lifetime and they are related by $L_p = \sqrt{D_p \tau_p}$.

The boundary condition for the above equation are

$$\Delta n = \frac{n_i^2}{N_a}(e^{qV/k_B T} - 1) \tag{2.2.2}$$

and

$$D_p \frac{d\Delta n}{dz} = -S_{rec} \Delta n \quad (z = w) \tag{2.2.3}$$

where S_{rec} refers to the surface velocity recombination, but it will be discussed in details in the next section.

At the boundary of the space charge region the carrier concentration satisfies eq. 2.2.2 hence, in this case, for $z = w_{scr} + w_n$. This boundary condition comes from the requirement that $E_{F_n} - E_{F_p} = qV_j$ throughout the SCR. The differential equation for diffusion is solved at $V = 0$, so the zero-order boundary condition reduced to $\Delta n = 0$. This approximation is justified since we are interested in the short-circuit current which is defined at zero voltage.

After that, according to the superposition approximation, we will calculate the J-V curve including the voltage dependence in the dark current. However, if several recombination mechanisms are considered we will notice that a voltage-dependent treatment is necessary to describe correctly the J-V curve and then the efficiency of the solar cell. These effects will be shortly described in the chapter four.

The second boundary condition is provided by the surface recombination at the outer surface

$$J_p = qD_p \frac{d\Delta n}{dz} = -qS_{rec} \Delta n \quad (z = w). \tag{2.2.4}$$

In the other quasi neutral region holes follow the same treatment:

$$D_n \frac{d^2\Delta p}{dz^2} - \frac{\Delta p}{\tau_n} + g(z,E) = 0 \tag{2.2.5}$$

where D_n is the diffusion constant for holes in the n side, τ_n is the lifetime and they are related by $L_n = \sqrt{D_n \tau_n}$.
The boundary condition for the above equation are

$$\Delta p(z = w_p) = 0 \tag{2.2.6}$$

and

$$D_n \frac{d\Delta p}{dz} = S_{rec}\Delta p \quad (z = 0) \tag{2.2.7}$$

because of

$$\Delta p = \frac{n_i^2}{N_a}(e^{qV/k_BT} - 1) \tag{2.2.8}$$

and

$$J_n = qD_p \frac{d\Delta p}{dz} = qS_{rec}\Delta p \quad (z = 0). \tag{2.2.9}$$

Solutions with Light Trapping carrier generation rate

These equations are important in reducing the transport problem of textured solar cells from a 3D problem to a 1D problem [33], so that an analytic solution can be found. Solving the partial differential equation for $V = 0$ we can find the explicit solution for Δn and the integration constants.

$$\Delta n(z,E) = \frac{\alpha_{lt}\Phi_{AM1.5}(R_b e^{\alpha_{lt}z}e^{-2\alpha_{lt}w} + e^{-\alpha_{lt}z})}{D_p[1 - R_b e^{-2\alpha_{lt}w}](1 - \alpha_{lt}^2 L_p^2)} + c_1 e^{z/L_p} + c_2 e^{-z/L_p} \tag{2.2.10}$$

where

$$\begin{aligned} c_1 = \frac{\alpha_{lt}\Phi_{AM1.5}L_p^2}{D_p[1 - R_b e^{-2\alpha_{lt}w}](1 - (1/n^2))(\alpha_{lt}^2 L^2 - 1)} & \left[e^{-\alpha_{lt}w}\left(R_b\left(\alpha_{lt} + \frac{S_{rec}}{D_p}\right) - \alpha_{lt} + \frac{S_{rec}}{D_p}\right)\right. \\ & \left. + e^{-\alpha_{lt}h - w_p/L_p}\left(\frac{1}{L_p} - \frac{S_{rec}}{D_p}\right)\left(1 + R_b e^{-2\alpha_{lt}w}\right)\right] \\ & \Big/ \left[e^{w/L_p}\left(\frac{1}{L_p} + \frac{S_{rec}}{D_p}\right) + e^{(2h-w)/L_p}\left(\frac{1}{L_p} + \frac{S_{rec}}{D_p}\right)\right] \end{aligned} \tag{2.2.11}$$

and

$$c_2 = \frac{\alpha_{lt}\Phi_{AM1.5}L_p^2}{D_p[1-R_b e^{-2\alpha_{lt}w}](1-(1/n^2))(\alpha_{lt}^2L^2-1)}(1+R_b e^{-2\alpha_{lt}w})e^{-\alpha_{lt}h+h/L_p} + c_1 e^{2h/L_p} \quad (2.2.12)$$

The same quantities for holes can also be extracted.

External Quantum Efficiency

Once the analytic solution for Δn is found, the diffusion current is easy to calculate according to eq. 2.2.3 and the *external quantum efficiency* is assumed equal to the diffusion current, so

$$EQE_p(E) = \frac{D_p}{\Phi_{AM1.5}}\frac{d\Delta n}{dz}|_{z=w_n+w_{scr}}. \quad (2.2.13)$$

A similar treatment holds for minority carriers, holes, in the emitter (n type quasi neutral region). As far as boundary conditions are concerned, several changes should be taken into account: the zero-order condition must be evaluated at the n side of the space charge region, so at $z = w_n$, whereas the first-order condition is calculated at the end of the n layer, at $z = 0$. Moreover, we assume that carriers generated inside the SCR are collected with a quantum efficiency of unity [38], thanks to the sweeping action of the built-in electric field. Once they come to one egde of the SCR, then they are drifted to the other qn region where they are majority carriers. The EQE contribution from the SCR is obtained by integrating the normalized carrier generation rates over the width of the SCR.

$$EQE_{scr}(E) = \int_{w_n}^{w_{scr}+w_n} \frac{g(z,E)}{\Phi_{AM1.5}}\,dz \quad (2.2.14)$$

Hence, the total short-circuit current is given by:

$$J_{scr} = \int_0^\infty q(EQE_n(E) + EQE_{scr}(E) + EQE_p(E))\Phi_{AM1.5}dE \quad (2.2.15)$$

In fig. 2.2.1 EQE in a 1μm solar cell is shown up to its different contributions. They are the external quantum efficiency for the quasi-neutral n and p region and the space charge region one's. Since the emitter (qn n layer) and the space charge region are very thin, their contribution are quite small for low energies. This effect is much more visible for thicker cells. EQE values vary from 0 to 1 and for high energies we notice that the EQE is equal to one.

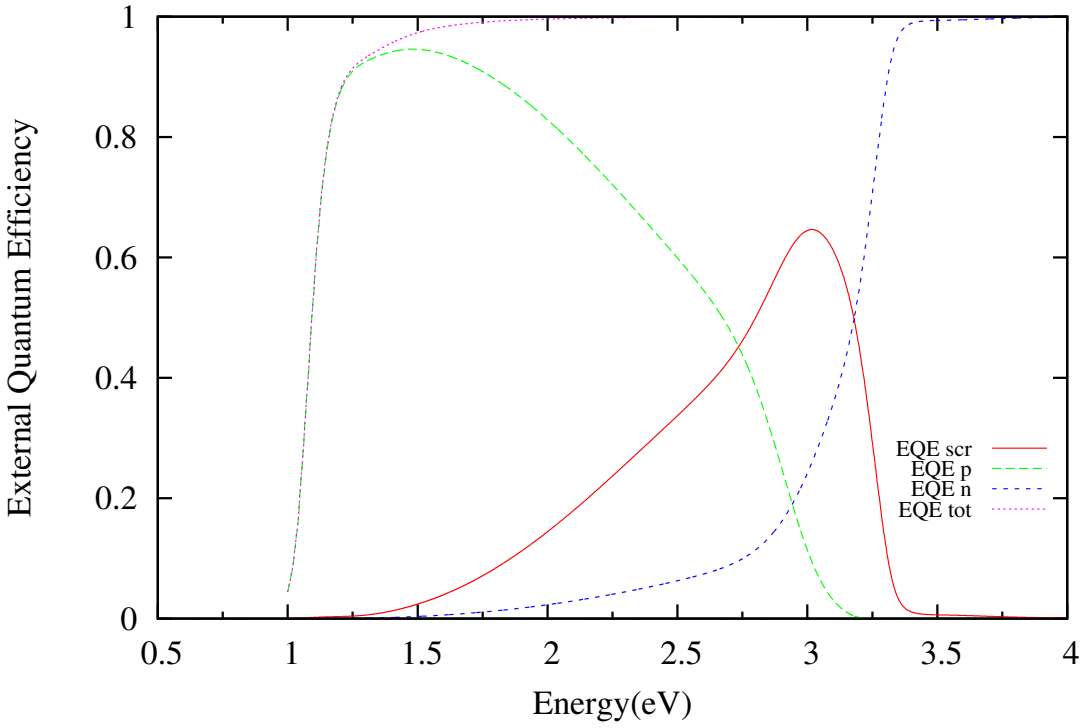

Figure 2.2.2: External quantum efficiency for $1\mu m$ silicon solar cell with $50nm$ emitter, $D_p = 40cm^2/s$, $D_n = 4cm^2/s$, $L_p = 200\mu m$, $L_n = 20\mu m$, $N_d = 10^{19}cm^{-3}$ and $N_a = 10^{16}cm^{-3}$

J(V) curve of the device: including the effects of thickness

We know that $J = J_{sc} - J_{dark}(V)$. Once J_{sc} has been calculated illumination has already been taken into account, so we can focus on J_{dark}.
The dark current density J_{dark} is expressed as the sum of three contributions from the qn regions and SCR, as for the case of the J_{sc}.

$$J_{dark,tot} = J_{dark,scr} + J_{dark,e} + J_{dark,h} \tag{2.2.16}$$

where $J_{dark,e}$ is the dark current due to electrons from the n side to the p side and $J_{dark,h}$ is related to holes which come from p to n. Dark $J(V)$ terms from qn regions are proportional to e^{qV/k_BT} and include the effects of thickness and SRH recombinations, both in the bulk and at the surfaces.
The diffusion equation can be solved with no source term (dark current) and using the voltage-dependent zero-order boundary condition eq. 2.2.2. Following this approach and calculating $J_n = qD_p\dfrac{d\Delta p}{dz}$ electrons and holes current can be find as follows:

$$J_e = \frac{qD_p n_0(exp(qV/kBT) - 1)}{L_p} \left(\frac{\frac{S_{rec}L_p}{D_p}\cosh(w_p/L_p) + \sinh(w_p/L_p)}{\frac{S_{rec}L_p}{D_p}\sinh(w_p/L_p) + \cosh(w_p/L_p))} \right) \tag{2.2.17}$$

$$J_h = \frac{qD_n p_0(exp(qV/k_BT) - 1)}{L_n} \left(\frac{\frac{S_{rec}L_n}{D_n}cosh(w_n/L_n) + sinh(w_n/L_n)}{\frac{S_{rec}L_n}{D_n}sinh(w_n/L_n) + cosh(w_n/L_n))} \right) \tag{2.2.18}$$

In fig. 2.2.1 the different contributions to J_{dark} are shown using a log scale. As said before talking about the EQE, the most important contribution to the J_{dark} still comes from the minority diffusive carriers in the qn p regions (electrons) because it is the thickest part of the cell. It is hard to distinguish between the total J_{dark} and the electrons' contribution.
Usually, the dark current from the p-type silicon is the dominant term, as this qn region is typically the thicker one in the device.
The contribution from the SCR has a different bias dependence, and it is proportional to $\sinh(eV/2k_BT)/(Vbi - V)$, according to [5], where V_{bi} is the built-in voltage determined by the selected dopings.

$$J_{scr}(V) = \frac{qn_i(w_p + w_n)}{\sqrt{\tau_n\tau_p}} \frac{2\sinh(qV/2k_BT}{q(V_{bi} - V)/k_BT})\xi \tag{2.2.19}$$

where the factor ξ tends to π for large forward bias. In fig. 2.2.1 the J-V curve and the gen-

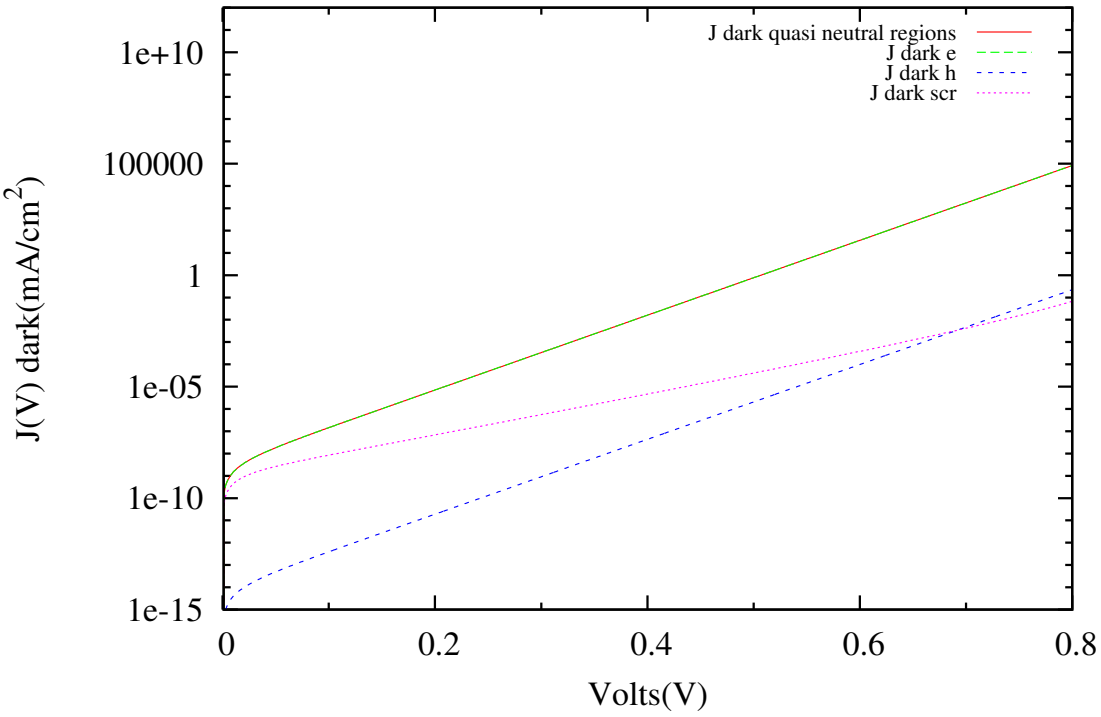

Figure 2.2.3: Different contributions to J_{dark} current for $1\mu m$ silicon solar cell with $50nm$ emitter, $D_p = 40cm^2/s$, $D_n = 4cm^2/s$, $L_p = 200\mu m$, $L_n = 20\mu m$, $N_d = 10^{19}cm^{-3}$ and $N_a = 10^{16}cm^{-3}$.

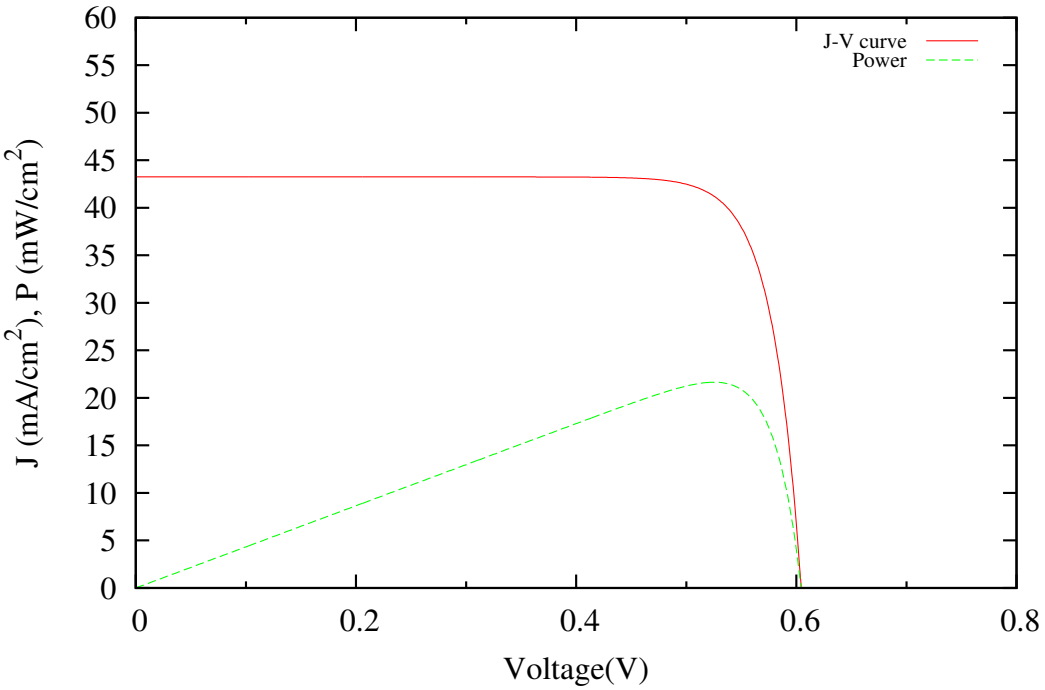

Figure 2.2.4: J-V curve for $1\mu m$ silicon solar cell with $50nm$ emitter, $D_p = 40cm^2/s$, $D_n = 4cm^2/s$, $L_p = 200\mu m$, $L_n = 20\mu m$, $N_d = 10^{19}cm^{-3}$ and $N_a = 10^{16}cm^{-3}$

erated power as a function of voltage are presented. The calculations are done implementing the superposition approximation discussed previously. For voltage higher than the open-circuit voltage the generated power is negative and the device performs as an LED. In the graph we can easily recognize the maximum power point and the open-circuit voltage too.

2.2.2 Effects of recombination

In a photovoltaic device one kind of generation is much more important then the others (photogeneration is much more important than thermal generation) [1], but as far as recombination is concerned, several mechanisms are involved. By *recombination* we think about the loss of mobile carriers by one of the following mechanisms.
There is a basic difference: *unavoidable* recombination and *avoidable* processes. The former is due to essential physical processes that take place inside the intrinsic material, the latter is largely due to imperfect material.
In particular we will focus on the main important recombination mechanisms:

- Radiative recombination

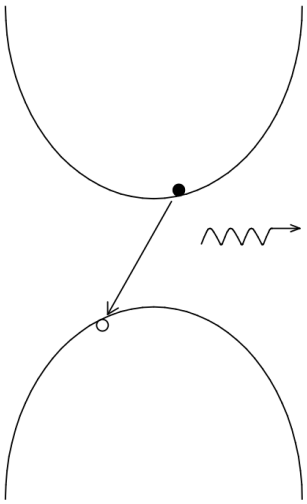

Figure 2.2.5: Schematic representation of radiative recombination.

- Auger recombination
- Shockley-Read-Hall bulk recombination
- Surface recombination

and they are physically different. Radiative recombination and Auger mechanisms depend on intrinsic properties of the semiconductor, on the other hand, the SRH process is due to defects in the crystal structure: the higher the quality, the lower the density of impurities in the sample and the less SRH recombination. Similarly, surface recombination depends on the quality of the interfaces.

Radiative recombination

Radiative recombination is due to an electron in the conduction band which recombines with a hole in the valence band. A schematic representation of radiative recombination is shown in fig. 2.2.5. It depends only on intrinsic properties. Normally, it is important in direct band gap semiconductors, since in indirect gap semiconductors, like silicon, a three bodies interaction is required for recombination and a phonon must be involved. Usually, radiative recombination is negligible in silicon solar cells, but it is very important when Gallium Arsenide is concerned.

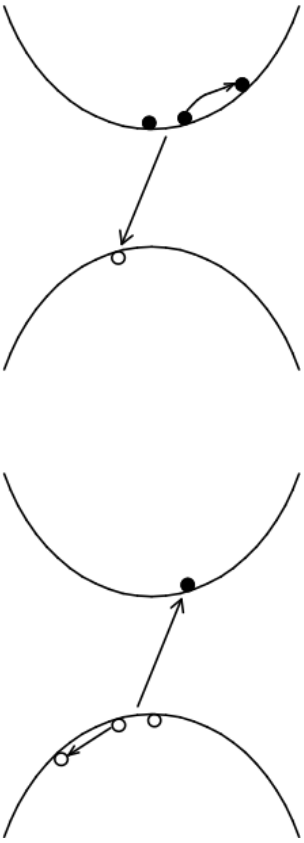

Figure 2.2.6: Schematic representation of Auger recombination for both electrons and holes.

Auger recombination

When two carriers of the same type interact, one gives part of its kinetic energy to the second one. Then the first carrier recombines across the band gap while the second one increases its energy and then relaxes towards the band edge giving away the extra amount of energy as heat. This is Auger mechanism and it depends only on semiconductor properties. A schematic representation of Auger recombination is shown in fig. 2.2.6.
Its recombination rate is given by:

$$U_{Auger}(\mathbf{r}) = B_{Auger}[n(\mathbf{r})p(\mathbf{r}) - n_i^2(\boldsymbol{r})] \tag{2.2.20}$$

where the constant B_{Auger} changes value accordingly to the polarity on the two carriers colliding.
Since it is a non radiative four-bodies process it may be important in both direct and indirect band gap semiconductors because the extra momentum is given to the promoted carrier. It is

a crucial factor in high-quality silicon solar cells, as the long radiative lifetimes results in a high carrier concentration. If the semiconductor is doped the above equation can be simplified to:

$$U_{Auger}(\mathbf{r}) = \frac{p(\mathbf{r}) - p_0(\mathbf{r})}{\tau_{p,Aug}}$$

$$U_{Auger}(\mathbf{r}) = \frac{n(\mathbf{r}) - n_0(\mathbf{r})}{\tau_{n,Aug}} \tag{2.2.21}$$

where the electron and holes lifetimes are:

$$\tau_{p,Auger} = \frac{1}{B_{Aug} N_d^2}$$

$$\tau_{n,Auger} = \frac{1}{B_{Aug} N_a^2} \tag{2.2.22}$$

Auger lifetimes are proportional to the square of the doping level: the higher the doping, the higher the Auger losses.

In our analytic approach a different treatment of Auger recombination has been taken into account and a semi-empirical model by Richter *et al.* [22] is used. It describes the Auger recombination rate in a general manner as a function of the dopant concentration. It also considers Coulomb-enhanced Auger recombination according to [22] and it further includes radiative recombination. This advanced parametrization for the intrinsic lifetimes $\tau_{intr,adv}$ gets:

$$\tau_{intr,adv} = \frac{\Delta n}{\left(np - n_{i,eff}^2\right)\left(2.5 \cdot 10^{-31} g_{eeh} n_0 + 8.5 \cdot 10^{-32} g_{ehh} p_0 + 3.0 \cdot 10^{-29} \Delta n^{0.92} + B_{rel} B_{low}\right)} \tag{2.2.23}$$

with the enhancement factors

$$g_{eeh}(n_0) = 1 + 13 \left\{ 1 - tanh \left[\left(\frac{n_0}{N_{0,eeh}} \right)^{0.66} \right] \right\} \tag{2.2.24}$$

and

$$g_{ehh}(p_0) = 1 + 7.5 \left\{ 1 - tanh \left[\left(\frac{p_0}{N_{0,ehh}} \right)^{0.63} \right] \right\} \tag{2.2.25}$$

and $N_{0,eeh} = 3.3 \cdot 10^{17} cm^{-3}$ and $N_{0,ehh} = 7.0 \cdot 10^{17} cm^{-3}$.

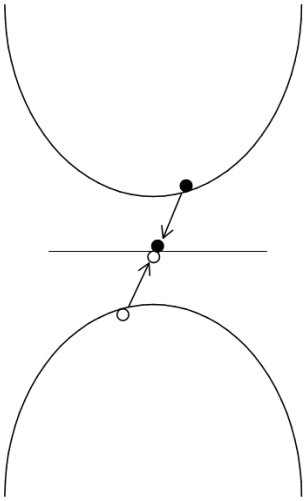

Figure 2.2.7: Schematic representation of SRH recombination.

Shockley-Read-Hall (SRH) recombination

Among the extrinsic recombination mechanisms, the SRH process is the most important one. A schematic representation of Auger recombination is shown in fig. 2.2.7. It is due to the presence of *traps* inside the sample. Usually broken crystal bonds, defects and impurities give rise to energy levels inside the band gap. When there are some trap, a carrier (an electron or a hole) is captured by localized traps and if both are captured by the same trap they recombine. The *Shockley-Read-Hall* recombination rate is given by:

$$U_{SRH}(\mathbf{r}) = B_{SRH} \frac{n(\mathbf{r})p(\mathbf{r}) - n_i^2(\mathbf{r})}{\tau_{n,SRH}(p(\mathbf{r}) - p_t(\mathbf{r})) + \tau_{p,SRH}(n(\mathbf{r}) - n_t(\mathbf{r}))} \tag{2.2.26}$$

where $p_t(\mathbf{r})$ and $n_t(\mathbf{r})$ are the hole and electron densities when their corresponding quasi-Fermi levels equal impurity energy level E_t:

$$n_t(\mathbf{r}) = n_i(\mathbf{r}) e^{(E_t - E_i)/k_B T}$$

$$p_t(\mathbf{r}) = p_i(\mathbf{r}) e^{(E_i - E_t)/k_B T}. \tag{2.2.27}$$

As for Auger recombination, when the semiconductor is doped these equation can be simplified to

$$U_{SRH}(\mathbf{r}) = \frac{p(\mathbf{r}) - p_0(\mathbf{r})}{\tau_{p,SRH}}$$

$$U_{SRH}(\mathbf{r}) = \frac{n(\mathbf{r}) - n_0(\mathbf{r})}{\tau_{n,SRH}}. \tag{2.2.28}$$

SRH strongly depends on the presence of defects in the sample; the lower the fabrication quality, the higher the recombination rate.
SRH and Auger recombination mechanisms are the most significant processes in silicon solar cells.

Surface recombination

During the fabrication processes the number of defects is usually higher near the interfaces then in the bulk. Hence, the importance of SRH recombination will be higher at the interfaces and there is a different expression for 2D-SRH recombination rate.

$$U_{SRH}\delta x = \frac{n_s p_s - n_i^2}{\frac{1}{S_n}(p_s + p_t) + \frac{1}{S_p}(n_s - n_t)} \tag{2.2.29}$$

where S_n and S_p are proportional to the number of traps at the interface and they are called *Surface Recombination Velocities*.
As usual, in doped semiconductors the previous relation becomes:

$$U_s\delta x = S_n[n(s) - n_0]$$

for p-type material

$$U_s\delta x = S_p[p(s) - p_0] \tag{2.2.30}$$

for n-type material.
This kind of recombination is also included in our analytic model through boundary conditions eq. 2.2.3 and eq. 2.2.7.

2.2.3 Effects of illumination on carrier concentration and Quasi-Fermi levels

According to chapter 1, we know that:

$$n = N_c\, e^{(E_F - E_c)/k_B T} \tag{2.2.31}$$

and in the same way for hole density

$$p = N_v\, e^{(E_v - E_F)/k_B T} \quad . \tag{2.2.32}$$

These equations say that electron and hole densities vary exponentially according to the position of the Fermi level in the band gap.

Quasi-Fermi levels

Calculating carrier concentration in the different regions of the solar cell allows us to extract the position of the Fermi level in the band gap as a function of z since

$$E_{F,e}(z) = E_C + k_B T \log\left(\frac{n(z)}{N_c}\right) \tag{2.2.33}$$

$$E_{F,h}(z) = E_V - k_B T \log\left(\frac{p(z)}{N_V}\right) \tag{2.2.34}$$

where n and p refer to carrier concentration in a specific region and E_C and E_V are the bottom of the conduction band and the top of the valence band. The point is: how can we calculate carrier concentrations? The analytic model provides informations about *quasi-neutral regions*, but what about the *space charge region*?
We will follow a different approach: in qn regions we calculate carrier concentrations from the analytic solution of the drift-diffusion equation first, then we extract quasi-Fermi levels. On the contrary, in SCR we first extrapolate a model for quasi-Fermi level, then we derive carrier concentrations.
First, let us focus on qn regions. We start with the qn n region so we are interested in minority holes and majority electrons. We would like to remind that we are under illumination at zero voltage.
As far as majority electrons are concerned, the total carrier concentration is due to both the doping and the mass action law, so:

$$n_N \approx N_d \tag{2.2.35}$$

since the contribution to majority carriers due to illumination seems to be negligible with these doping levels ($\approx 10^{19} cm^{-3}$ for donors) .

On the other hand, for minority holes we have:

$$p_N = p_{ill,N} + p_0 \tag{2.2.36}$$

where $p_{ill,N}$ is hole concentration due to illumination in the N side. It is obtained by integrating $p_{ill,N}(z, E)$ over energy:

$$p_{ill,N} = \int p_{ill,N}(z, E)\, dE\,. \tag{2.2.37}$$

Now we can calculate quasi-Fermi levels as:

$$E_{F,e,N}(z) = E_C + k_B T \log\left(\frac{n_N(z)}{N_c}\right) \tag{2.2.38}$$

$$E_{F,h,N}(z) = E_V - k_B T \log\left(\frac{p_N(z)}{N_V}\right)\,. \tag{2.2.39}$$

Now, we are interested in the qn p region. We have the opposite situation: minority electrons and majority holes. According to the same treatment we have:

$$p_P = N_a \tag{2.2.40}$$

since the contribution to majority carriers due to illumination seems to be negligible with these doping levels ($\approx 10^{16} cm^{-3}$ for acceptors).
On the other hand, for minority electrons we have:

$$n_P = n_{ill,P} + n_0 \tag{2.2.41}$$

where $n_{ill,P}$ is electron concentration due to illumination in the P side. It is obtained by integrating $n_{ill,P}(z, E)$ over energy:

$$n_{ill,P} = \int n_{ill,P}(z, E)\, dE\,. \tag{2.2.42}$$

Now we can calculate quasi-Fermi levels as:

$$E_{F,e,P}(z) = E_C + V_{bi} + k_B T \log\left(\frac{n_{ill,P} + n_0(z)}{N_c}\right) \tag{2.2.43}$$

$$E_{F,h,P}(z) = E_V + V_{bi} - k_B T \log\left(\frac{p_P(z)}{N_V}\right)\,. \tag{2.2.44}$$

Let us move now across the SCR. In principle the SCR is divided into two parts: the $n-type$ SCR and the $p-type$ SCR. With these doping levels, the thickness of the SCR in the N side is very low with respect to the p-type of the SCR. Hence, we are going to consider the quasi-Fermi level in the n side of the SCR to be constant.
We developed a simple model to describe directly quasi-Fermi level in the SCR. This simple model interpolates the solution for the electrostatic potential dividing the depletion layer into two parts: before and after the crossing point for quasi-Fermi levels.

$$E_{F,e,SCR_N}(z) = F_{e,N} \tag{2.2.45}$$

$$E_{F,h,SCR_N}(z) = F_{h,N} + qN_d\frac{(z-w_n)^2}{2\epsilon_{Si}} \tag{2.2.46}$$

and for the p side of the SCR before the crossing point:

$$E_{F,e,SCR_P}(z) = F_{e,N} \tag{2.2.47}$$

$$E_{F,h,SCR_P}(z) = F_{h,N} + V_{bi} - qN_a\frac{(z-h)^2}{2\epsilon_{Si}} \tag{2.2.48}$$

while after the crossing point we have:

$$E_{F,e,SCR_P}(z) = F_{e,N} + V_{bi} - qN_a\frac{(z-h)^2}{2\epsilon_{Si}} - F_{h,N} \tag{2.2.49}$$

$$E_{F,h,SCR_P}(z) = F_{e,N} - 0.022 \tag{2.2.50}$$

where this energy shift depends on where we put the origin in the energy scale.

Charge carrier concentration

Thanks to the solutions of the drift diffusion equations we already know carrier concentrations in the qn region (they are shown in fig. 2.2.8 for a 1μm silicon structure), but now we are going to calculate carrier densities inside the SCR.
In the n side of the SCR we have:

$$n(z) = N_c\, e^{(E_{Fe,N}(z)-E_c)/k_BT} \tag{2.2.51}$$

and in the same way for hole density,

$$p(z) = N_v\, e^{(E_v-E_{Fh,N}(z))/k_BT} \tag{2.2.52}$$

while in the p side, before the crossing point, we have:

$$n(z) = N_c\, e^{(E_{Fe,P}(z) - E_C + V_{bi} - qN_a \frac{(z-h)^2}{2\epsilon_{Si}})/k_B T} \tag{2.2.53}$$

and in the same way for hole density

$$p(z) = N_v\, e^{(E_V + V_{bi} - qN_a \frac{(z-h)^2}{2\epsilon_{Si}} - E_{Fh,P}(z))/k_b T} \tag{2.2.54}$$

and in the P side, after the crossing point, we have:

$$n(z) = N_c\, e^{(E_{Fe,P}(z) - E_C + V_{bi} - qN_a \frac{(z-h)^2}{2\epsilon_{Si}})/k_B T} \tag{2.2.55}$$

and in the same way for hole density

$$p(z) = N_v\, e^{(E_V + V_{bi} - qN_a \frac{(z-h)^2}{2\epsilon_{Si}} - E_{Fh,P}(z))/k_B T} \,. \tag{2.2.56}$$

In fig. 2.2.9, fig. 2.2.10 and fig. 2.2.11 there is a comparison between the analytic way to calculate quasi-Fermi levels and Silvaco ATLAS results. We did the comparison for three different cell thicknesses: $1\mu m$, $10\mu m$ and $100\mu m$, all of them with a $50nm$ emitter, but we do not report any graph for the thickest structure because the corresponding plot is dominated by the quasi neutral p region thanks to the very large difference between the base and emitter thickness, hence it does not provide any useful information.
In fig. 2.2.9 we show the comparison between quasi-Fermi levels across the whole device, while in fig. 2.2.10 we focus only on a 2 μm layer. In fig. 2.2.11 we show the same quantities infig. 2.2.10, but looking at the entire structure. Material parameter are given in captions. As far as the qn regions are concerned the validation is good and although the space-charge region is a bit tricky the agreement improves on increasing the cell's thickness (reducing the importance of the SCR).
From statistical thermodynamics we know that Fermi levels are well-defined for system under equilibrium. If we are out of equilibrium (e.g. we are under illumination or under applied bias) the built in potential barrier is reduced and more majority carriers are able to diffuse across the junction, so that there is now a net current of electrons from n to p and holes from p to n. The Fermi levels are split by the applied bias, but their difference stays constant [1].
When the junction is illuminated, light creates electron-hole pairs in all three regions. Carrier densities are enhanced above their equilibrium values and the electron and hole quasi Fermi

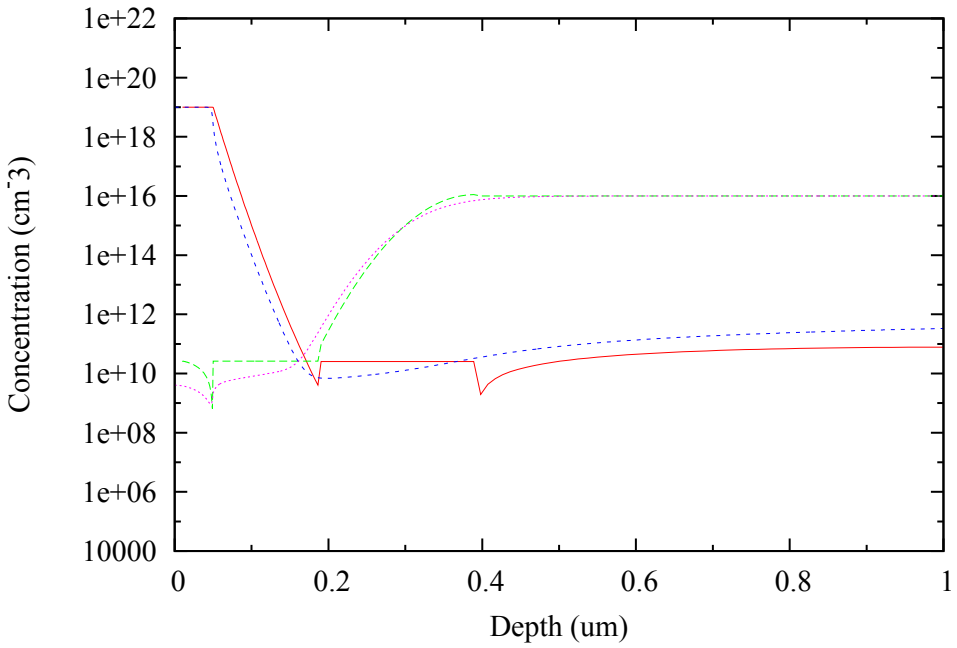

Figure 2.2.8: Carrier concentration for $1\mu m$ silicon solar cell with $50nm$ emitter, $D_p = 40cm^2/s$, $D_n = 4cm^2/s$, $L_p = 200\mu m$, $L_n = 20\mu m$, $N_d = 10^{19}cm^{-3}$ and $N_a = 10^{16}cm^{-3}$ under illumination at V=0. Dotted lines are calculated using a finite-elements method software (Silvaco [39]): the blue one refers to electrons and the pink one to holes. Solid red curve comes from the analytic model and it is related to electrons, while green dashed line refers to holes. There are some kinks due to the different parametrization of carriers concentrations across the structure.

levels are split. The electric field at the junction acts to separate the pairs by driving minority carriers across the junction. In this condition V=0 so that, within the depletion approximation the two quasi Fermi levels remain nearly constant across the SCR. This is what we observe in the next figures.

If we are both under illumination and applied bias (regime we did not studied since the analytic model works at zero voltage), the SCR is reduced because of the shrinkage due to forward bias, hence there are two effects: the splitting of the quasi Fermi levels and the reduction of the importance of the SCR, both caused by the applied bias. Therefore the difference between the quasi-Fermi levels becomes more and more constant, as it is far from the junction.

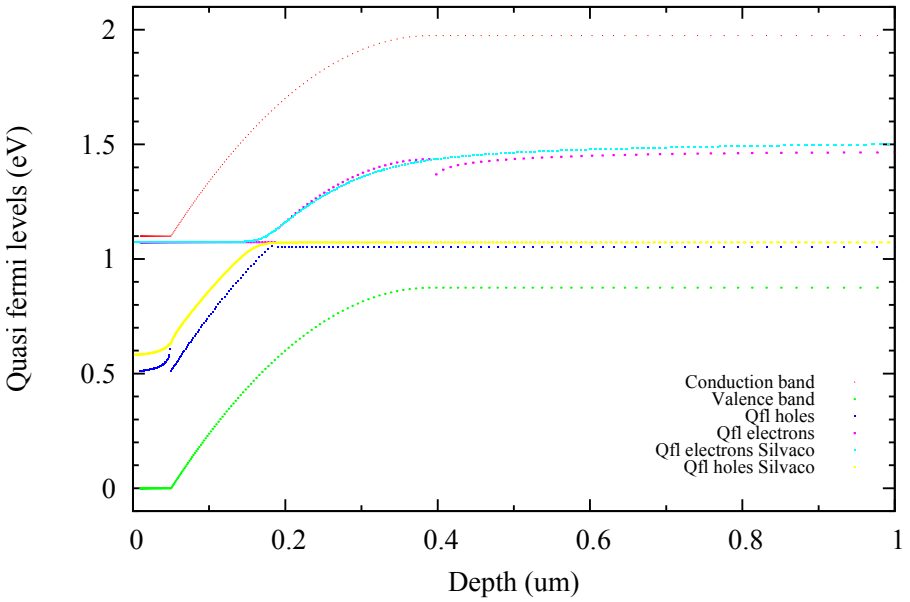

Figure 2.2.9: Quasi Fermi levels for $1\mu m$ silicon solar cell with $50nm$ emitter, $D_p = 40cm^2/s$, $D_n = 4cm^2/s$, $L_p = 200\mu m$, $L_n = 20\mu m$, $N_d = 10^{19}cm^{-3}$ and $N_a = 10^{16}cm^{-3}$ under illumination at V=0.

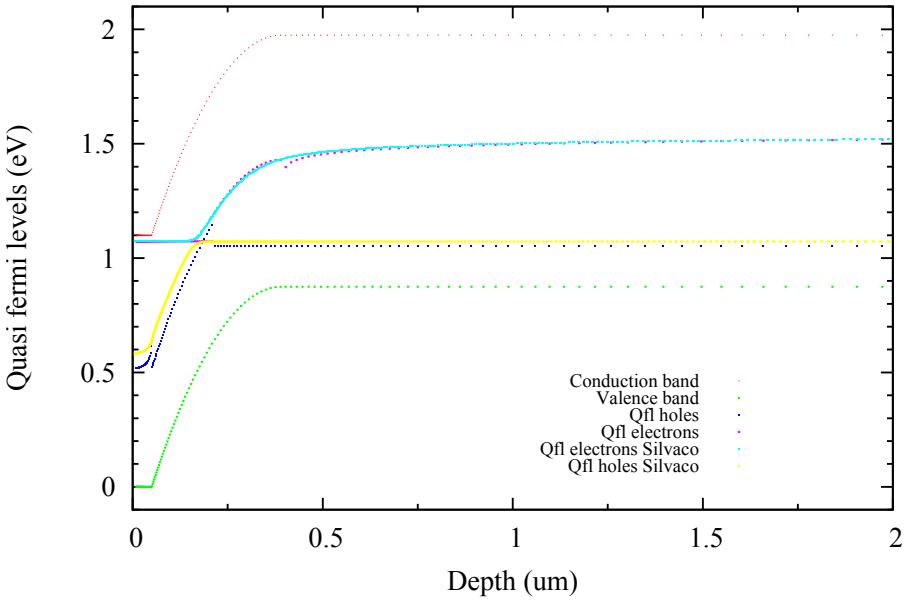

Figure 2.2.10: Quasi Fermi levels for $10\mu m$ silicon solar cell with $50nm$ emitter, $D_p = 40cm^2/s$, $D_n = 4cm^2/s$, $L_p = 200\mu m$, $L_n = 20\mu m$, $N_d = 10^{19}cm^{-3}$ and $N_a = 10^{16}cm^{-3}$ under illumination at V=0 (zoom up to $2\mu m$).

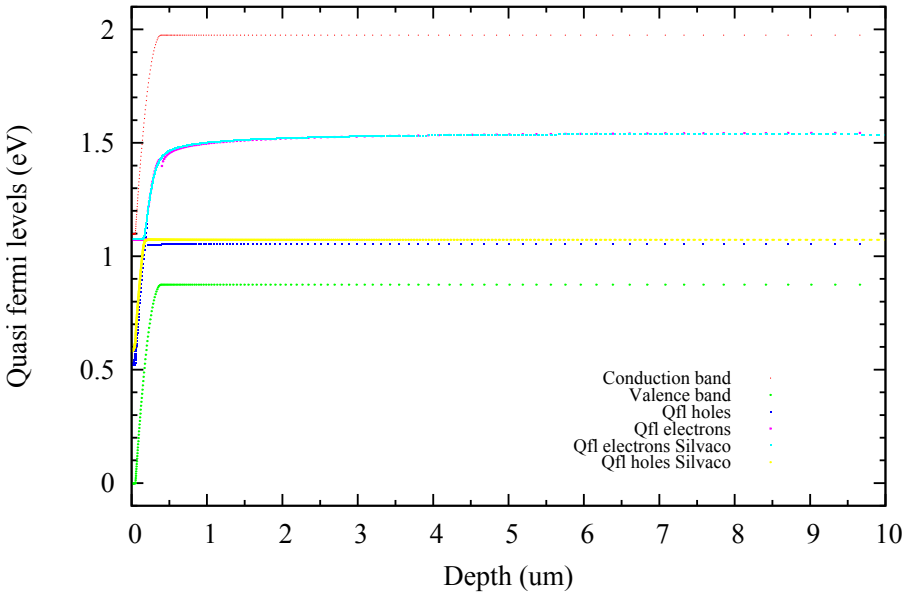

Figure 2.2.11: Quasi Fermi levels for $10\mu m$ silicon solar cell with $50nm$ emitter, $D_p = 40cm^2/s$, $D_n = 4cm^2/s$, $L_p = 200\mu m$, $L_n = 20\mu m$, $N_d = 10^{19}cm^{-3}$ and $N_a = 10^{16}cm^{-3}$ under illumination at V=0.

2.3 Validation of the model and efficiency limits

In this section we present a validation of the analytic model we have just described against Silvaco ATLAS numerical simulator. Silvaco is a general purpose simulator which solves drift-diffusion equation with finite-elements method assuming neither superposition approximation nor depletion region assumption with a finite layer for the potential drop.
All the Silvaco numerical calculations for this work have been provided by Dr. P. Kowalczewski at the Physics Department of the University of Pavia.
At first we focus on general aspects of standalone silicon solar cells and then we go deeply into the role of recombination mechanisms which limit the efficiency.
Now we study a different structure with $5nm$ emitter and different doping levels:
$N_a = 10^{16}cm^{-3}$ and $N_d = 1.5 \cdot 10^{18}cm^{-3}$. We calculated the quantities of the next figures for the same structure shown in 1 with a silver back reflector with a real reflectance.

2.3.1 Auger recombination

We start by considering solar cells limited by intrinsic Auger losses. We treat Auger recombination using the parametrization reported by Richter *et al.* [22]. We also consider band gap

narrowing (BGN) according to the model by Schenk [19]. Since silicon is an indirect band gap material, we neglect radiative recombination, which may give an appreciable effect only for very thick cells.

In fig. 2.3.1 we show the short-circuit current, the open-circuit voltage, the fill factor and

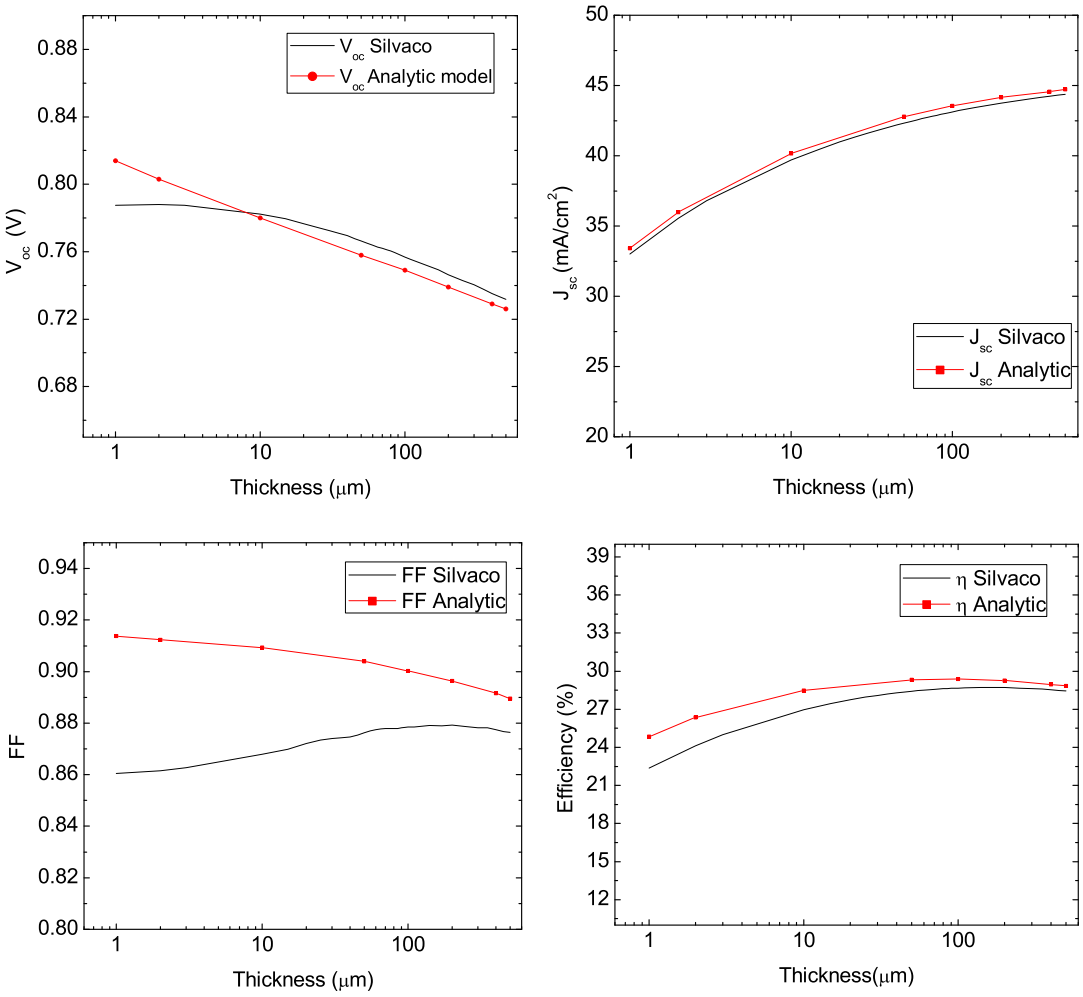

Figure 2.3.1: Analytic and numerical results including only Auger recombination for $5nm$ emitter and $N_a = 10^{16}cm^{-3}$, $N_d = 1.5 \cdot 10^{18}cm^{-3}$.

the limiting efficiency of c-Si solar cells as a function of the absorber thickness. The maximum efficiency is equal to 28.5% and it is obtained for the $80\mu m$ thick cell. This is a bit lower then the efficiency limit of 29.43% reported recently in literature [20]. This was obtained with ideal diode equation and assuming undoped silicon, while in our solution of drift-diffusion equations for real structure the base doping increases Auger losses and decreases the limiting efficiency.

These results are compared with Silvaco ATLAS numerical simulations and we show a very good agreement as long as the thickness is increased because the effects of all the approximations made are less important for thicker structures.
The aim of this validation is to check the impact of the approximations used to arrive at analytic results. As shown in fig. 2.3.1, the agreement is satisfactory for J_{sc} , proving that the assumption of ideal collection from the SCR does not lead to a substantial overestimation of photo-generated current. V_{oc} and efficiency are systematically over-estimated in the analytic model, but the relative difference is always less than 10%. This is mainly due to the superposition approximation used in the calculation of the JV curve. In fact, the approximation over-estimates the photogenerated current, and underestimates the dark current, at the same time. This affects all the cell's calculated electrical parameters. However, we see that the discrepancy in efficiency is nearly independent of the cell thickness, and that the general trend is well reproduced. A full validation of the model, in the presence of surface recombination, is presented in the next sections.

2.3.2 Auger and SRH recombination

So far, we have considered an idealized material, and therefore the cell performance was limited by intrinsic Auger recombination. Now we consider also extrinsic losses related to SRH recombination. The primary reason of this choice is that when we are dealing with the short-circuit current, which has been calculated at zero voltage in this case, we can consider only SRH recombination since Auger lifetime tends to infinity according to [22]. As a consequence, diffusion length is limited by only SRH. On the other hand, when we move to the dark current we consider the effects of voltage, obviously, so we must take into account both recombination mechanisms.
With such a thin emitter ($5nm$), the cell efficiency is limited by the diffusion length $L_{p,SRH}$ of the minority carriers (electrons) in the base.
The diffusion length of holes in the highly-doped emitter is taken equal to $L_{n,SRH} = L_{p,SRH}/10$. It can be seen that thicker cells are more sensitive to SRH recombination.
Since we are now considering two different recombination mechanisms in the base, we must calculate an effective diffusion length as follows:

$$L_{p,eff} = \sqrt{D_p \cdot \tau_{eff,p}} \tag{2.3.1}$$

and

$$\tau_{eff,p} = \frac{(\tau_{SRH,p} \cdot \tau_{AUG,p})}{(\tau_{SRH,p} + \tau_{AUG,p})} \tag{2.3.2}$$

with $D_p = 25cm^2/s$.
On the other hand, as far as the emitter is concerned, we do not consider Auger recombination since the bulk losses are negligible because of the very small thickness. We inserted a different treatment for n side and p side in our analytic model. The diffusion length value in the qn N region is set to be $L_n = 2 \cdot 10^{-5}$ m. In fig. 2.3.2 we show the short-circuit current, the

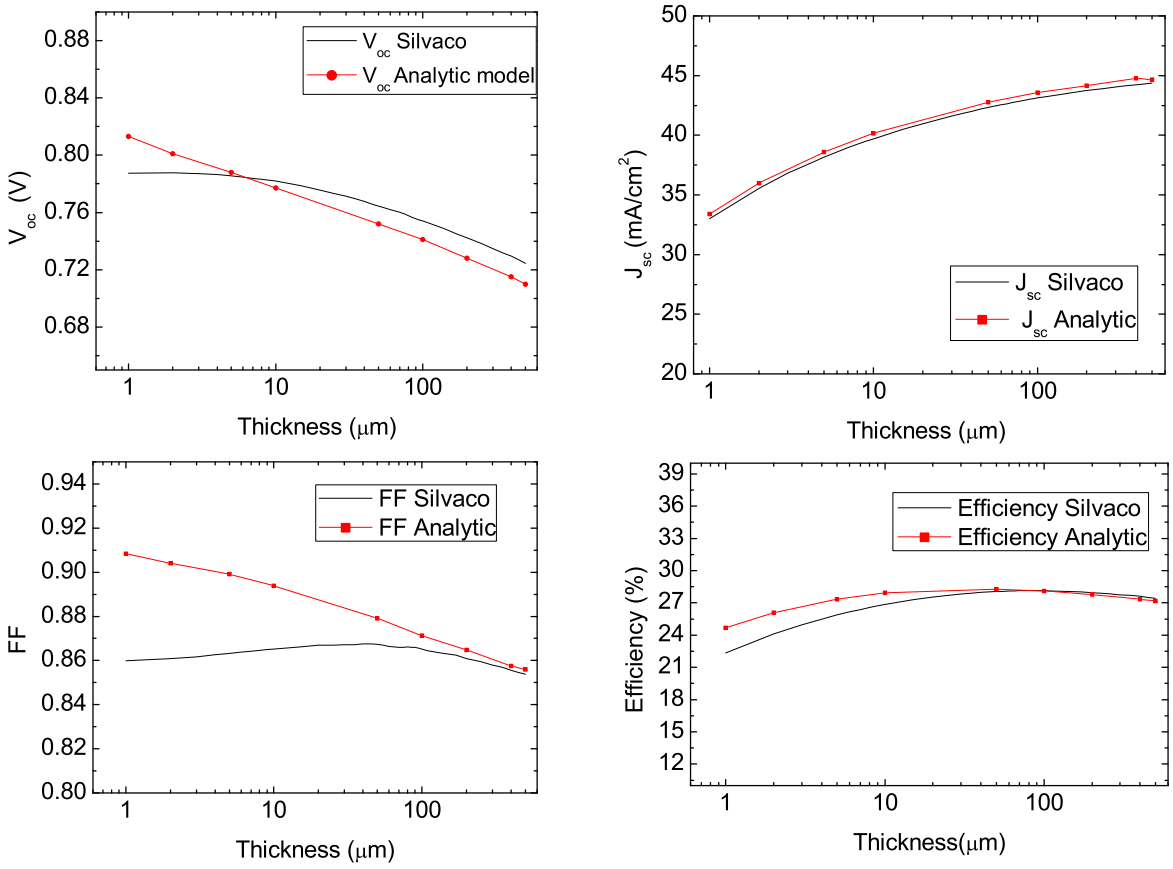

Figure 2.3.2: Analytic and numerical results including Auger and SRH recombination for $5nm$ emitter and $N_a = 10^{16}cm^{-3}$, $N_d = 1.5 \cdot 10^{18}cm^{-3}$ with $L_{p,SRH} = 3.48mm$.

open-circuit voltage, the fill factor and the limiting efficiency of c-Si solar cells as a function of the absorber thickness. The results allow us to estimate the optimal thickness as $60\mu m$ and it is lower than with only Auger. This is due to the presence of two different recombination mechanisms. The thicker the cell, the more important recombination, hence to achieve a high efficiency a smaller thickness is required.

As in the previous validation, these results are compared with Silvaco ATLAS numerical simulations and we notice a very good agreement as far the thickness is increased since the effects of all the approximations made are less important for thick structures.

2.3.3 Including surface recombination

Now we also focus on surface recombination, which is another extrinsic loss mechanism related to trap states at the surface. In the next figures we report the efficiency as a function of front or back surface recombination velocity (SRV) and of the absorber thickness.
In the first part of the paragraph we include only Auger as a bulk recombination mechanism, but then we add also the effect of SRH recombination.

Auger and surface recombination

In fig. 2.3.3 we include surface recombination at the back surface, setting surface recombination at the front to zero. We show a contour plot which represents the efficiency as a function of thickness and of back surface recombination velocity. The maximum efficiency is around 29% and it is achieved by a 100 μm cell with very low surface recombination velocity.
In fig. 2.3.4 we included surface recombination at the front surface, setting surface recombination at the back to zero. We show a contour plot which represents the efficiency as a function of thickness and of front surface recombination velocity. The maximum efficiency is slightly higher, around 30% and it is achieved by a 100 μm cell with a quite wide range of surface recombination velocity.
We conclude that solar cells are more sensitive to recombination at the rear interface rather than to recombination at the front. The reason is that most of the light is absorbed in the base and the corresponding minority carriers (i.e. electrons in the thick p-type base) recombine at the rear interface. Thus, the solar cell is more tolerant to surface recombination at the front interface, even if in the presence of texturization which moderatly increases the effective surface at the front. From now we focus on front surface recombination, neglecting recombination at the back, which has anyway to be of the order of a few cm/s to target high efficiency. In realistic devices, there is usually an oxide passivating layer at the back and point contacts are implemented [40]. For this reason, back SRV can be significantly reduced. On the other hand, front SRV may be increased due to the texturing.
In the calculations above, we assumed a very high material quality ($L_p = 3.47mm$, L_n does not matter since the emitter is 50 nm thin) and the higher is the material quality, the more important are losses at the surfaces.
All these calculations are made to compare and validate the analytic model against Silvaco

ATLAS results for the same structure published in [40] and the agreement is very good.

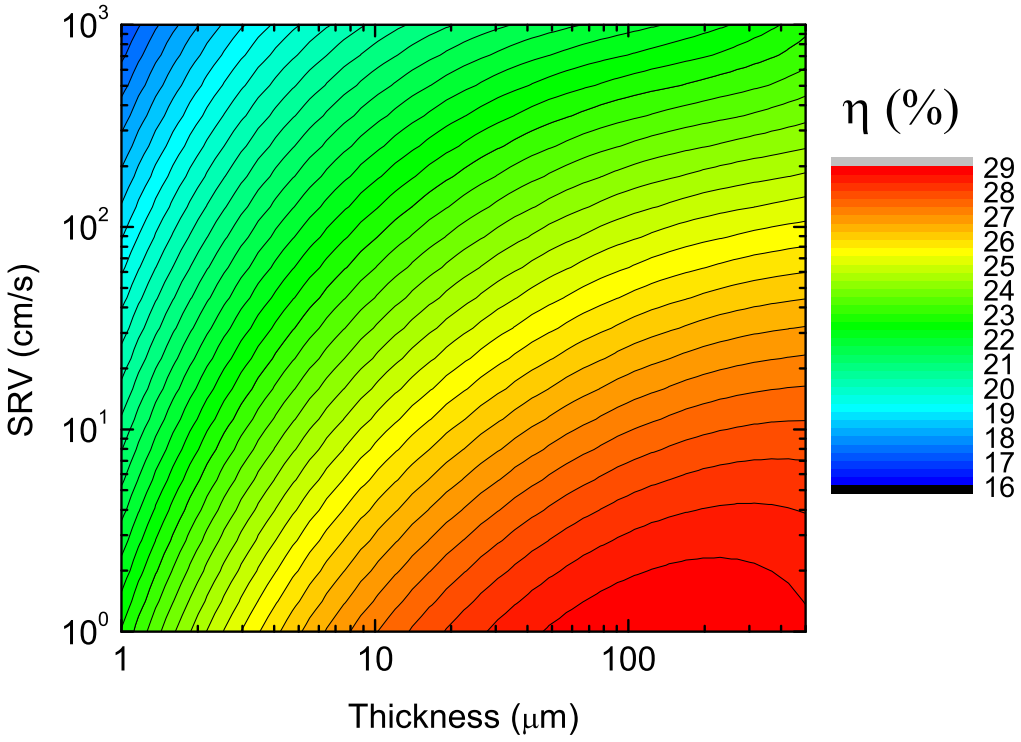

Figure 2.3.3: Analytic results for the conversion efficiency including only Auger and SRV back recombination with $L_p = 3.47mm$.

Auger, SRH and surface recombination

From now on we focus only on front surface recombination, neglecting recombination at the back, which has anyway to be of the order of a few cm/s to target high efficiency.
Our results are another validation of the analytic model in the presence of an additional recombination mechanism due to bulk recombination and they should be compared with Silvaco ATLAS numerical results presented in [40].
In this part of our study we also include SRH recombination. It is included since the diffusion lengths we used are the same reported in [40] for the same physical situations.
In fig. 2.3.5 we show a contour plot which represents the efficiency as a function of thickness and of front surface recombination velocity for $L_p = 1.78mm$. The highest efficiency is around 27% and it is achieved by a few tens microns cell with a quite wide surface recombination ve-

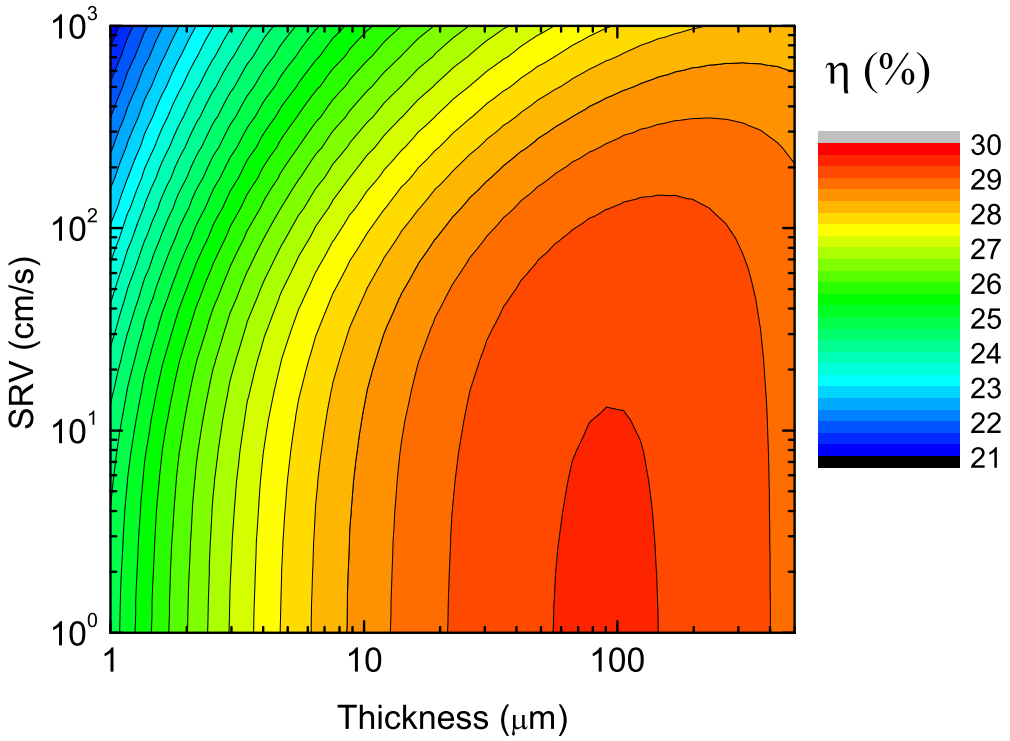

Figure 2.3.4: Analytic results for the conversion efficiency including only Auger and SRV front recombination with $L_p = 3.47mm$.

locity range. In fig. 2.3.6 we show a contour plot which represents the efficiency as a function of thickness and of front surface recombination velocity for $L_p = 0.675mm$, so we decreased material quality. The maximum possible efficiency is around 25% which is obtained for a few tens microns cell with a wider surface recombination velocity range.
This study tries to answer the following question: having a given material quality, what is the maximum value of the front SRV to reach a certain efficiency?

The results indicate that a front SRV below 100 cm/s is required to reach an efficiency around 27%, while the front SRV is limited to about 1000 cm/s when the efficiency target is around 25%. It should be noticed, however, that this conclusions refer to an ideal situation of full Lambertian light trapping and no parasitic optical losses: in real situations part of the incident light is lost by reflection at the front and by absorption losses in the transparent conductive layers, so that the final efficiencies are lower than the ideal ones. Still, the trends shown in this section give an indication of the tolerance of the solar cell efficiency against surface recom-

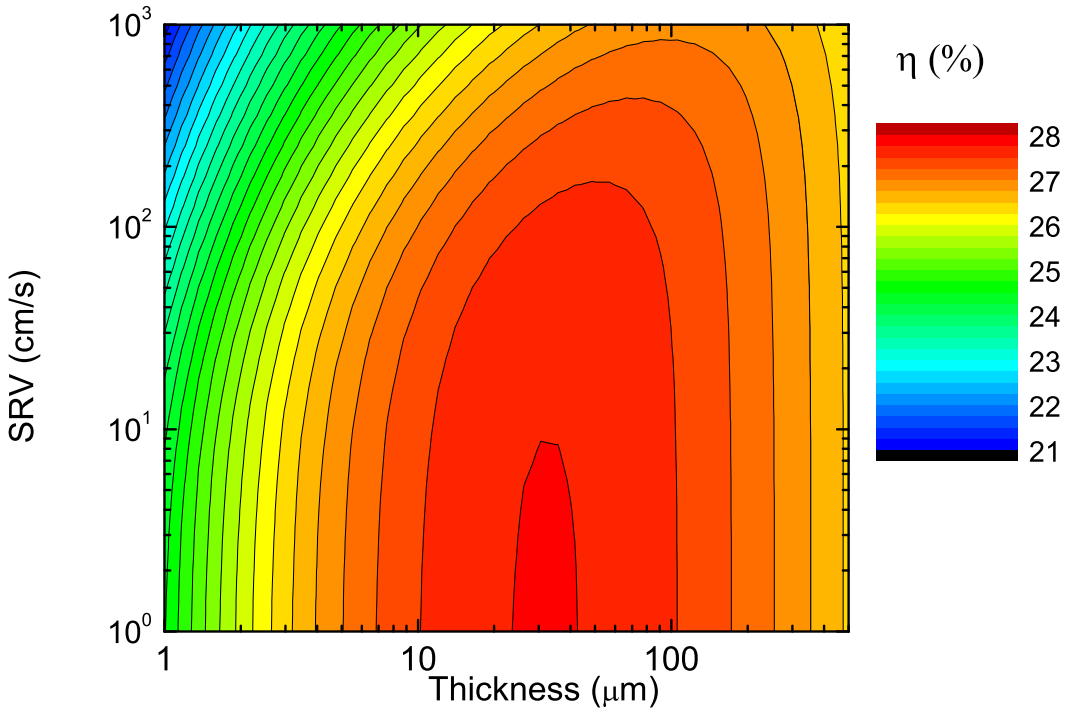

Figure 2.3.5: Efficiency as a function of the thickness and diffusion length $L_{p.SRH}$ of the minority carriers (electrons) in the base, calculated for the structures with a Lambertian light trapping with long $L_p = 1.78mm$.

bination. Moreover, by comparing with [40], they provide a further validation of the analytic model in the presence of all recombination mechanisms. In the following chapter, the model is extended in order to perform a similar study for the silicon/perovskite tandem structure.

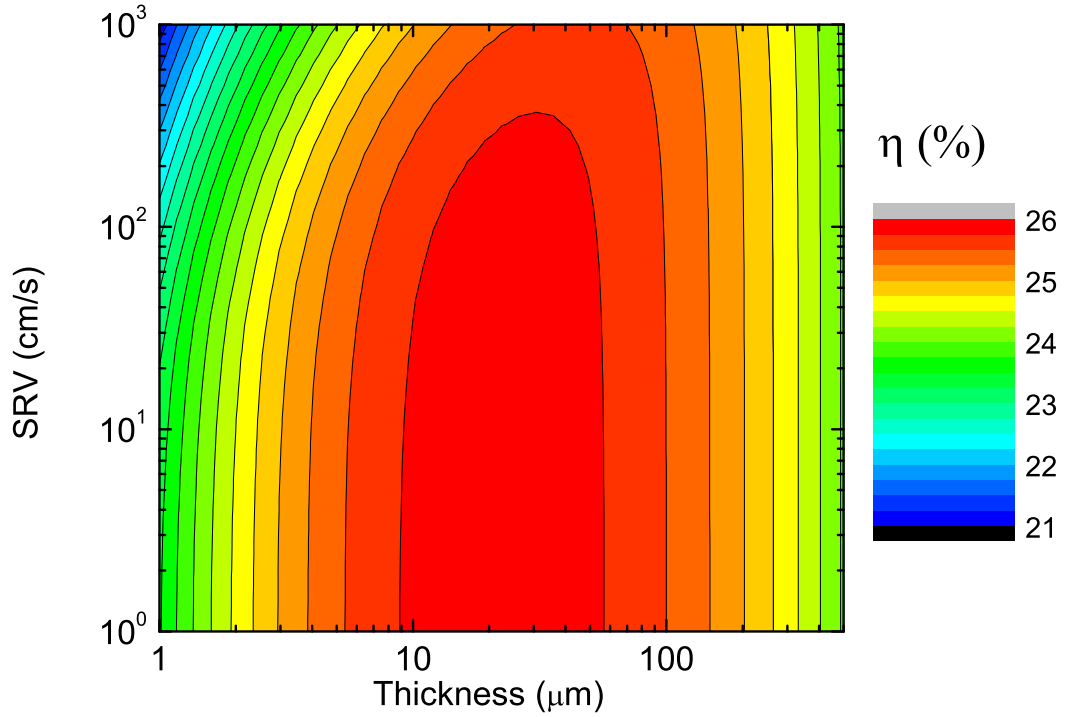

Figure 2.3.6: Efficiency as a function of the thickness and diffusion length $L_{p.SRH}$ of the minority carriers (electrons) in the base, calculated for the structures with a Lambertian light trapping with short $L_p = 0.675mm$.

Chapter 3

Tandem solar cells

3.1 Perovskite top cell

To make photovoltaics fully competitive with conventional energy sources, further progress towards ultrahigh efficiency low-cost solar modules is required [15]. The most straightforward way to accomplish this goal lies in combining existing high-efficiency c-Si solar cell technology with a high-band gap top cell to create a tandem solar cell. This depends on the presence of an appropriate efficient top cell. Recently, organic-inorganic halide perovskite solar cells were born, which are appropriate for complementing c-Si solar cell, in a tandem structure.
In the following subsections we will investigate some general properties of perovskite solar cells and we will discuss a very simple model to treat the perovskite top cell.

3.1.1 Generalities on perovskite solar cells

Perovskite is a calcium titanium oxide mineral composed of calcium titanate, with the chemical formula $CaTiO_3$. It also lends its name to a very wide class of compounds which have the same type of crystal structure as $CaTiO_3$, known as the *perovskite structure*.
A perovskite solar cell is a type of solar cell which includes a perovskite structured compound, most commonly a hybrid organic-inorganic lead or tin halide-based material, as the light-harvesting active layer. Perovskite materials such as the methylammonium lead halides are cheap to produce and simple to manufacture. Solar cell efficiencies of devices using these materials increased from 3.8% in 2009 to a certified 20.1% in 2014 [41] [42] making this the fastest-advancing solar technology to date (see 3.1.1). According to detailed balance analysis, the efficiency limit of perovskite solar cells is about 31%, which approaches to Shockley-Queisser detailed balance limit as the band gap is slightly higher than the optimal value. The most commonly perovskite absorber is methylammonium lead trihalide $CH_3NH_3PbX_3$ (see fig. 3.1.2),

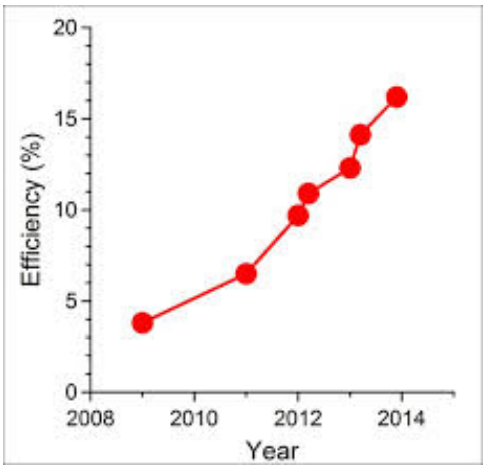

Figure 3.1.1: Efficiency in Perovskites during last years - www.OxfordPV.com

where X is a halogen ion such as I^-, Br^-, Cl^-, and it has an optical direct band gap between $2.3eV$ and $1.6eV$ depending on halide content. An important characteristic of the methylammonium lead halides, is a controllable band gap by the halide content.
The materials also display a diffusion length for both holes and electrons of over one micron [16]. The long diffusion length means that these materials can function effectively in a thin-film architecture, and that charges can be transported in the perovskite itself over relatively long distances (as compared to organic compounds or other thin-film solar materiarls). It has recently been reported that charges in the perovskite material are predominantly present as free electrons and holes, rather than as bound excitons, since the exciton binding energy is low enough to enable charge separation at room temperature [43] [44].
According to the detailed balance model by Shockley and Queisser, the maximal output power of a solar cell can be achieved if the following set of hypotheses are fulfilled:

- Carrier populations obey Maxwell–Boltzmann statistics. Particularly, the quasi-Fermi levels of electrons and holes are uniformly split through the cell and the splitting equals the applied voltage. The assumption is reasonable if mobility of photocarriers (electrons and holes) are sufficiently large. Regarding perovskite materials, charge carrier mobility as high as $10cm^2V^{-1}s^{-1}$ has been observed.

- Radiative band-to-band recombination mechanism is the only existing one. Non radiative recombination, such as Auger recombination and trap (defect) assisted recombination are ignorable.
  Different from silicon with an indirect band gap, perovskite material has a direct band gap. Therefore, Auger recombination is sufficiently suppressed, which has been verified

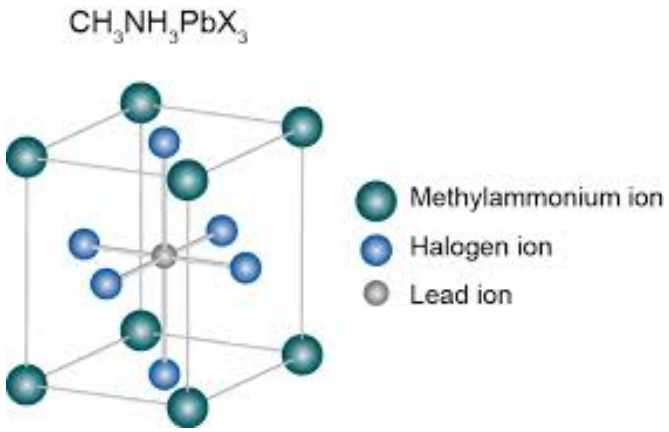

Figure 3.1.2: Perosvkite structure - www.OxfordPV.com

in recent experimental results. Moreover, light emission from perovskite solar cells is dominated by a sharp band-to-band transition that has a radiative efficiency much higher than that of organic solar cells.

- Internal conversion efficiency reaches 100%. When one photon is absorbed, it produces one electron-hole pair; and when one electron-hole pair recombines, it produces one photon. For perovskite solar cells, the internal quantum efficiency approaches 100%.

3.1.2 Silicon/perovskite tandem solar cells: state of the art

Silicon/perovskite tandem solar cells are a promising challenge of photovoltaics. They are assumed to be the next step to overcome the old silicon single junction efficiency limits and they are cheaper and easier then inorganic-inorganic tandem solar cells to be fabricated. This is why there is a strong interest among scientists who work on photovoltaics. In the last few years several works involving organic-inorganic tandems have been published, here we focus on the most significant ones which consider perovskites.
In [45], Loper *et al.* present a four-terminal tandem solar cell consisting of a methylammoniumleadtriiodide top cell and a c-Si heterojunction bottom cell. The four-terminal tandem solar cell yields an efficiency of 13.4% (top cell: 6.2%, bottom cell: 7.2%). They employ the four-terminal tandem solar cell for a detailed investigation of the optical losses and to derive guidelines for further efficiency improvements. Based on a power loss analysis, they estimate

that tandem efficiencies of 28% are attainable using an optically optimized system based on current technology, whereas a fully optimized, ultimate device with matched current could yield up to 31.6%. However, no light trapping is implemented in this work.

Another improvement is given by [46], which uses a transparent silver nanowire electrode on perovskite solar cells to achieve a semi-transparent device. The semi-transparent cell is placed in a mechanically-stacked tandem configuration onto copper indium gallium diselenide (CIGS) and low-quality multicrystalline silicon to achieve solid-state polycrystalline tandem solar cells with a net improvement in efficiency over the bottom cell alone. This work paves the way for integrating perovskites into a low-cost and high-efficiency (25%) tandem cell.

Mailoa *et al.* [47] fabricated a monolithic tandem by developing a silicon-based interband tunnel junction that facilitates majority-carrier charge recombination between the perovskite and silicon sub-cells. They achieve a stable 13.7% power conversion efficiency with the perovskite as the current-limiting sub-cell and identify key challenges for this device architecture to reach efficiencies over 25%.

In [48] Filipic *et al.* analyse and discuss the optical properties of various tandem architectures: mechanically stacked (four-terminal) and monolithically integrated (two-terminal) tandem devices, consisting of a methylammoniumleadtriiodide perovskite top solar cell and a crystalline silicon bottom solar cell. They provide layer thickness optimization guidelines. Their characterization based simulations predict that with optimized layer thicknesses the four-terminal configuration enables efficiencies over 30%, well above the current single-junction crystalline silicon cell record of 25.6%. Efficiencies over 30% can also be achieved with a two-terminal monolithic integration of the sub-cells, combined with proper selection of layer thicknesses.

On the other hand, as far as light trapping is concerned, Schneider *et al.* [49] present a practical tandem cell structure combining conventional pyramidal surface texturing on the Si bottom cell with a wavelength-selective intermediate reflector. This design satisfies the three optical requirements for high-performance perovskite-on-silicon tandem solar cells: low front surface reflectance, light-trapping of short wavelength light, and high transmission of long wavelength light to the bottom cell. This performance corresponds to absolute efficiency increases of 2-4% compared to a planar tandem cell with a single layer ARC on the front surface. Using a simple tandem cell efficiency model, they showed that efficiencies as high as 35% may be achievable with an optimal high-band gap perovskite top cell.

Our aim is to calculate the efficiency for silicon/perovskite tandem solar cell using our analytic model to describe silicon bottom cell which takes into account several recombination mechanisms. In this way we can check how the different recombination mechanisms affect the efficiency. Moreover, we also treat perovskite top cell analytically using ideal diode equation and studying the behaviour of its efficiency as a function of the band gap. We also consider

light trapping and a high quality material for the bottom cell. Thanks to these improvements and to the band gap optimization we can approach a final $\approx$ 38 % efficiency limit for that tandem. In conclusion, we are going to develop an analytic model to describe a tandem system with light trapping, recombination and top cell band gap optimization.

3.1.3 Semi-empirical model to treat perovskite solar cells

Owing to the recent discovery of one of the most promising perovskite structures, methylammonium-lead-triiodide (MALI), as photoactive material and its yet unknown band structure and recombination properties, we cannot access the fundamental J_0 or V_{oc} limit of this material at the present stage. There are two alternative ways to proceed: the first consists of using published V_{oc} values and the following relation to derive a relevant range of the diode saturation current density (see fig. 3.1.3). The record value is $J_0 = 1.76082 \cdot 10^{-17} mA/cm^2$, calculated from the illuminated I–V curve and $V_{oc} = 1.07V$ and $J_{sc} = 21.5 mA/cm^2$ presented by Liu *et al.* [16] with a planar device prepared by evaporation. We chose another way to proceed: our perovskite top cell material has a direct band gap of 1.55 eV, a open-circuit voltage of 1.1 V and a 140 nm thickness, these value being taken from literature [15]. To model perovskite top

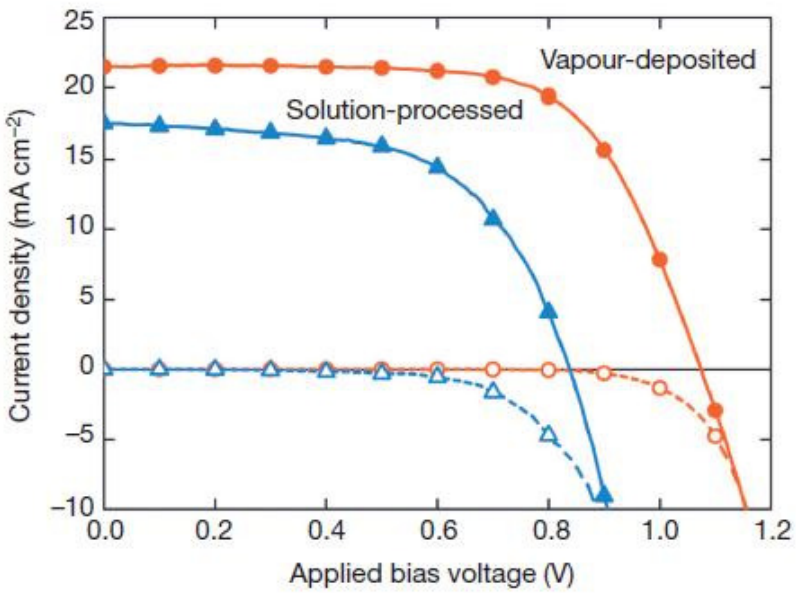

Figure 3.1.3: Experimental JV curve of the best performing solutions-processed (blue lines, triangles)and vapour-deposited (red lines, circles) planar heterojunction perovskite solar cells measured under simulated AM 1.5 (solid lines) and in the dark (dashed lines) [16].

cell performance we use ideal diode equation, hence:

$$\eta = \frac{J_{sc} V_{oc}}{P_s} \tag{3.1.1}$$

and we calculated the short-circuit current as follows:

$$J_{sc} = \int q \Phi_{AM1.5} A_p E dE \tag{3.1.2}$$

where

$$A_p = (1 - e^{(-\alpha_p w_{op}))} + R_{sm} e^{(-\alpha_p w_{op})} (1 - e^{(-\alpha_p w_{op})}) / (1 - R_{sm} e^{(-2\alpha_p w_{op})} \cdot (1 - (1/n_p^2))) \ . \tag{3.1.3}$$

It follows applying the Green's formalism to our tandem structure and it will be explained in the next subsection.
In this way we are able to calculate the efficiency for our perovskite top cell.
Since we based our perovskite's analysis on experimental published values we cannot include the effects of thickness in our theoretical framework. Obviously thickness matters because top cell efficiency is deeply related to the absorption in the active layer which depends on its dimensions, but from the mathematical point of view it is very difficult to be studied since we know the V_{oc} only for a specified thickness (140 nm) [15].

3.2 Optical coupling

3.2.1 Light trapping in tandems: a simple device structure

To explore light trapping in tandems with c-Si, we model a four-terminal tandem cell, see fig. 3.2.1, with a c-Si rear cell and a thin high-band gap top cell. This top cell is made of perovskite.
We manage light in tandems reflecting short wavelength light via an intermediate selective reflector that is transparent for long wavelength light which incises onto the silicon bottom cell. We consider an intermediate reflector characterized by a step function reflectance:

$$R(E) = 1 \ \ , \ E \geq E_{E_{gap,perovskite}} \tag{3.2.1}$$

and

$$R(E) = 0 \ \ , \ E \leq E_{E_{gap,perovskite}} \ . \tag{3.2.2}$$

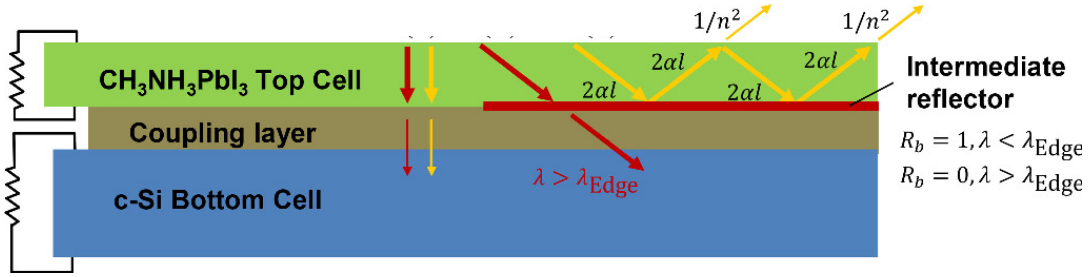

Figure 3.2.1: 4-Terminal tandem structure

We model a perovskite absorber obtained by vapour deposition with a thickness of $140nm$.
For this structure we can consider the optical coupling between the two cells with a selective coupling reflector, but on the other hand we can study both cells separately from the electronic point of view, since we have four terminals. As far as the electronic behaviour is concerned, we are going to study the perovskite top cell using the ideal diode equation to calculate its efficiency, whilst our analytic model is implemented to study the silicon bottom cell.
From the optical point of view, light trapping is implemented in both cells and we use the Green's formalism which described in chapter two. For the silicon bottom cell, the solar spectrum which gives rise to the carrier generation rate is filtered by both the top cell and the selective mirror. In the next subsection we will go more in details into optics of our tandem system.

3.2.2 Lambertian formalism to describe tandems

We have already presented analytical equations for broadband light trapping in planar films, but they require an opaque back reflector which is unsuitable for tandems. We introduce here a selective reflector and we extend the formalism by Green.
According to Green [13], we calculate the infinite sum of optical events for a rear reflector randomizing the internal path of light within the absorbing material.
We also introduce the possibility of the rear reflector to transmit light ($T_b(\lambda) + R_b(\lambda) = 1$). We neglect absorption in the rear reflector. With an appropriate choice of the wavelength-dependent terms we allow for selective light trapping.
Summing the infinite series of events [24], we are able to write the total reflection (R_T), absorption in the semiconductor (A_S) and total transmission (T_T) of both top cell and selective mirror for the structure in fig. 3.2.2. In fig. 3.2.2 we can notice the front surface with texturization which increases the effective surface and randomizes light. In comparison with a usual double

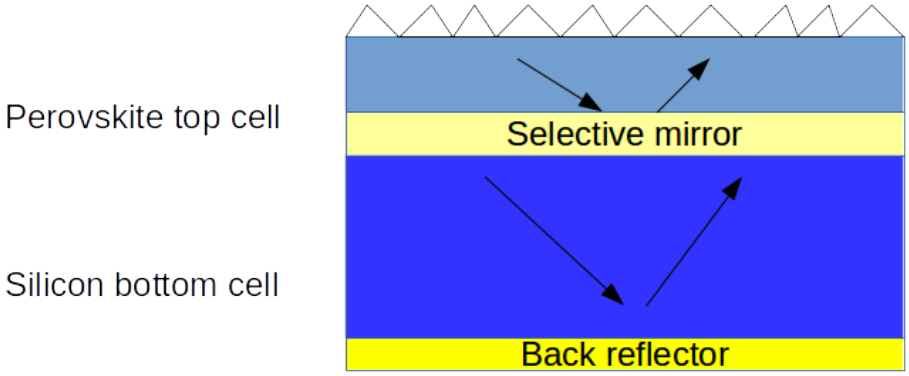

Figure 3.2.2: Silicon-perovskite tandem solar cell with light trapping.

pass due to a back reflector, randomization increases the absorption since we introduce a $\cos\theta$ factor in the light path. Look at fig. 2.1.1 for comparison.
According to [15] we can calculate

$$R_T = R_{ext} + \frac{(1-R_{ext})R_b(1-R_f)T^+T^-}{1-T^+T^-R_fR_b} \tag{3.2.3}$$

$$T_T = \frac{(1-R_{ext})T^+T_b}{1-T^+T^-R_fR_b} \tag{3.2.4}$$

$$A_S = \frac{(1-R_{ext})(1-T^+)+T^+R_b(1-T^-)}{1-T^+T^-R_fR_b} \tag{3.2.5}$$

and

$$R_{ext} = 0 \tag{3.2.6}$$

$$T^+, T^- = e^{-\alpha W_{op}} \tag{3.2.7}$$

$$W_{op} = \left(\frac{2+x}{1+x}\right) \tag{3.2.8}$$

$$x = a(\alpha W)^b \tag{3.2.9}$$

using Green's approximate solution with $a = 0.935$ and $b = 0.67$ for high refractive index materials.
We can calculate a new carrier generation rate for the silicon bottom cell in the tandem as follows:

$$T_T = \frac{(1-R_{ext})T^+T_b}{1-T^+T^-R_fR_b} \tag{3.2.10}$$

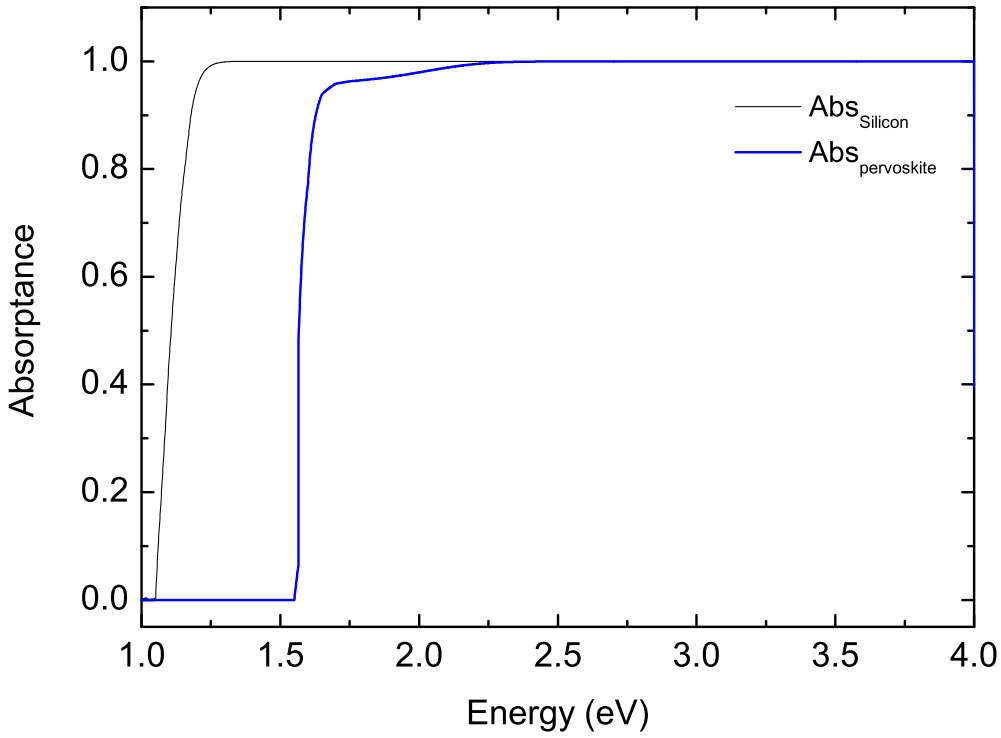

Figure 3.2.3: Absorption in silicon and perovskite. They are both calculated with Lal's formalism [50]. Absorption is a property of the material and it does not depend on the reflectivity of the selective mirror, that is why absorption in silicon is still one even if for energies higher than perovskite's band gap.

$$g(z,E) = [\frac{\alpha_{lt}(R_b e^{2\alpha_{lt}W} e^{\alpha_{lt}z} + e^{-\alpha_{lt}z})\Phi_{AM1.5}(E)}{1 - R_b e^{2\alpha_{lt}W}\left(1 - \frac{1}{n^2}\right)}] \cdot T_T \tag{3.2.11}$$

and now we can apply the same formalism developed above to study tandems.

In fig. 3.2.3 we show how the solar spectrum is absorbed by the two active materials and we can now calculate the absorption in silicon and in perovskite solar cell by using the formalism by Lal [50]. Absorption is a property of the material and it does not depend on the reflectivity of the selective mirror, that is why absorption in silicon is still one even if for energies higher than perovskite's band gap.

Then, in the same way described in the second chapter we can calculate the external quantum efficiency for the silicon bottom cell. In fig. 3.2.4 and fig. 3.2.5 we present two different results for external quantum efficiency as a function of energy: the first one refers to a $100\mu m$ bottom

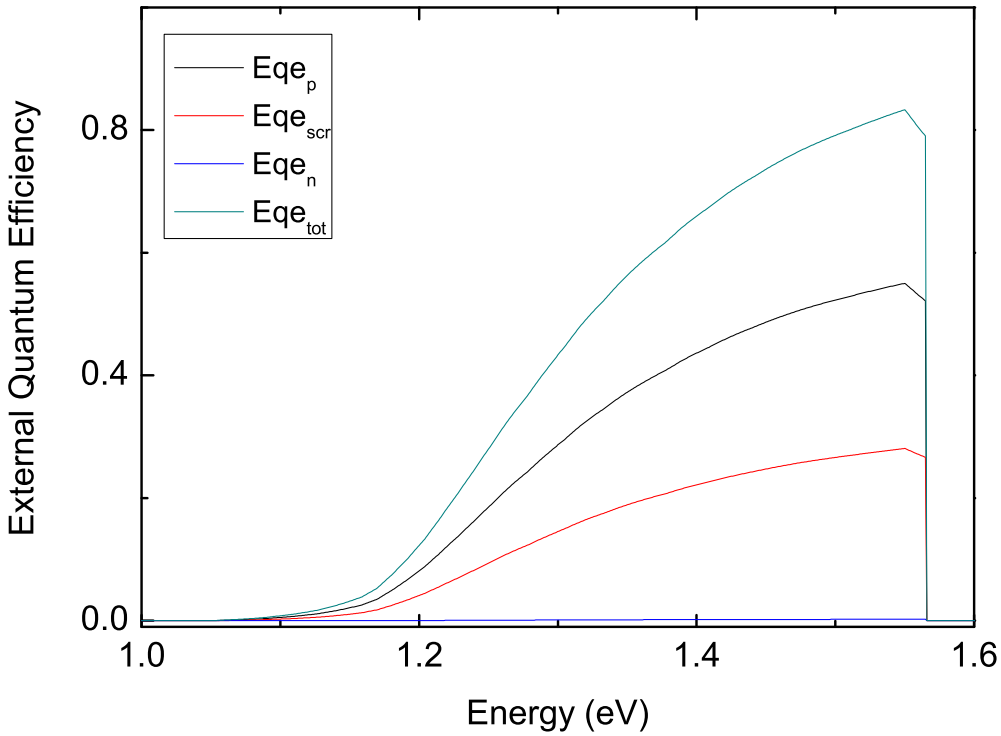

Figure 3.2.4: External Quantum efficiency in silicon bottom cell for $1\mu m$ thickness with both Auger and SRH. The diffusion length in the quasi neutral p region is equal to $L_p = 3.485mm$, while the diffusion length in the quasi neutral n region is equal to $L_n = 20\mu m$.

cell while the second one is calculated for $1\mu m$ silicon thickness. We can notice that in the second case, $1\mu m$ silicon bottom cell the three contributions for external quantum efficiency (electrons in the p-side, holes in the n-side and carriers in the space charge region) are quite similar, while in the first thicker structure electron's external quantum efficiency dominates all other quantities. This is due to the thickness of the base which is around 100 μm while the emitter is a very thin $50nm$ layer.

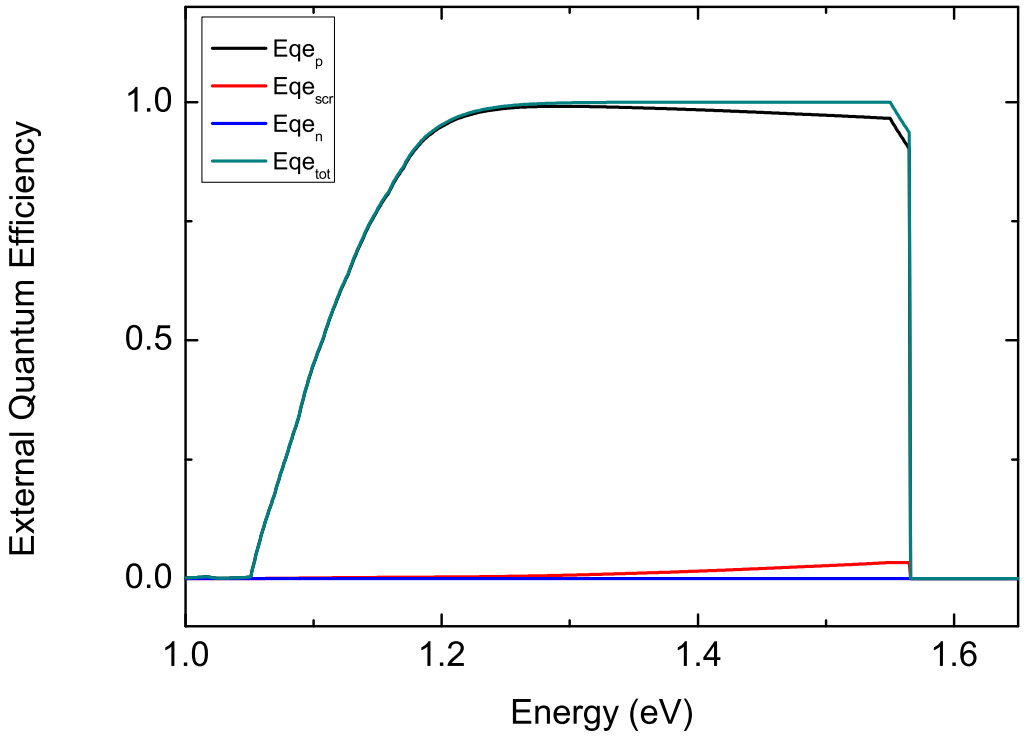

Figure 3.2.5: External Quantum efficiency in silicon bottom cell for $100\mu m$ thickness with both Auger and SRH. The diffusion length in the quasi neutral p region is equal to $L_p = 3.485mm$, while the diffusion length in the quasi neutral n region is equal to $L_n = 20\mu m$.

3.3 Efficiency limits in tandems

Let us now study the efficiency limits for tandem solar cells with our 4-terminal structure.
As we have already said, for the perovskite top cell we investigate the efficiency using the ideal diode equation. For the silicon bottom cell we follow the same treatment used for the standalone silicon bottom cell. Here we present our results.
In fig. 3.3.1 and fig. 3.3.2 we present J_{sc} and V_{oc} as a function of silicon bottom cell thickness using a log scale. At first, we studied tandem solar cell including in the dark current only Auger recombination, then we included also SRH recombination. The primary reason of this choice is that when we are dealing with the short-circuit current, which has been calculated at zero voltage in this case, we can consider only SRH recombination since Auger lifetime tends to infinity according to [22]. As a consequence, diffusion length is limited by only SRH. On the other hand, when we move to the dark current we consider the effects of voltage, obviously, so we must take into account both recombination mechanisms. Auger recombination has been studied according to the Richter model, while SRH has been introduced throughout an effective diffusion length. In particular we have:

$$t_{eff} = (t_{effsrh} \cdot t_{auger})/(t_{eff\,srh} + t_{auger}) \tag{3.3.1}$$

where

$$t_{effsrh} = L^2_{p\,srh}/D_p \tag{3.3.2}$$

and $L_{p,srh} = 3.47mm$.
By the way, the J_{sc} which has been calculated according to the analytic model are derived at zero voltage, where Auger recombination has a negligible effect. For V_{oc}, FF and efficiency, which require a calculation at finite voltage, Auger is included too. The V_{oc} calculated in fig. 3.3.1 including also SRH recombination is slightly lower then the same quantity with only intrinsic losses. That is why the efficiency will be lower in the first condition. On the other hands, as far as J_{sc} is concerned in fig. 3.3.2, the two curves are identical as Auger recombination is negligible at zero voltage. In fig. 3.3.3 we have FF for tandem system and, since

$$FF = V_{oc}J_{sc}/P_{max} \tag{3.3.3}$$

we have the same trend as in fig. 3.3.1 and fig. 3.3.2: the more important are the recombination mechanisms, the lower the FF.
In fig. 3.3.4 we present the efficiency for perovskite-silicon tandems as a function of silicon bottom cell thickness on a log scale. There are several curves: the efficiency of perovskite top cell, which is a constant because it does not depend on the silicon thickness according to ideal

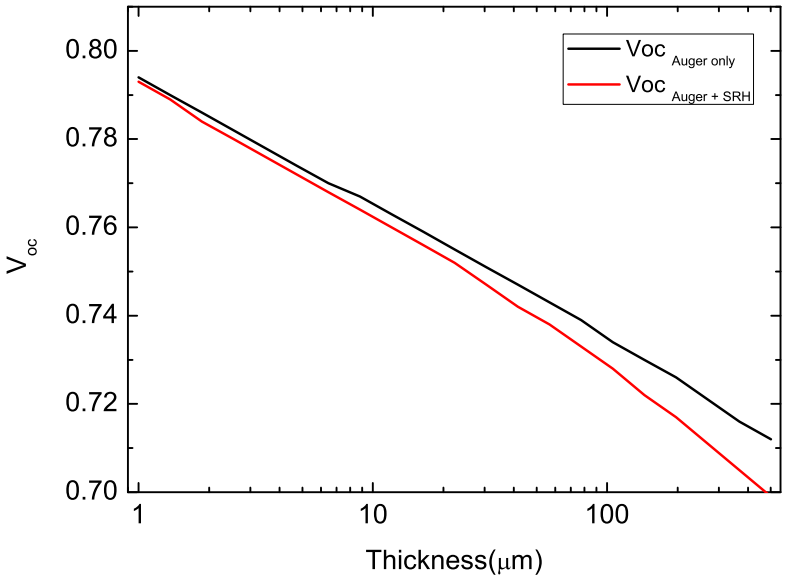

Figure 3.3.1: Analytic results for V_{oc} including recombination with $L_p = 3.47mm$.

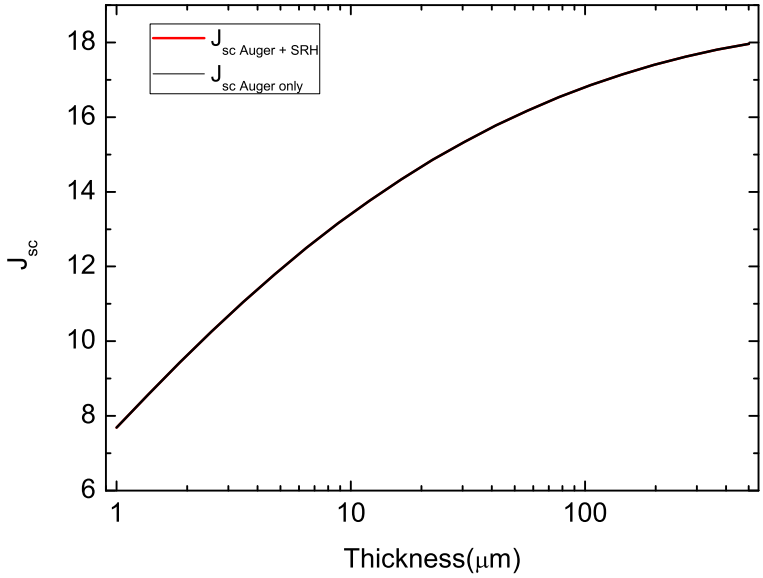

Figure 3.3.2: Analytic results for J_{sc} including recombination with $L_p = 3.47mm$.

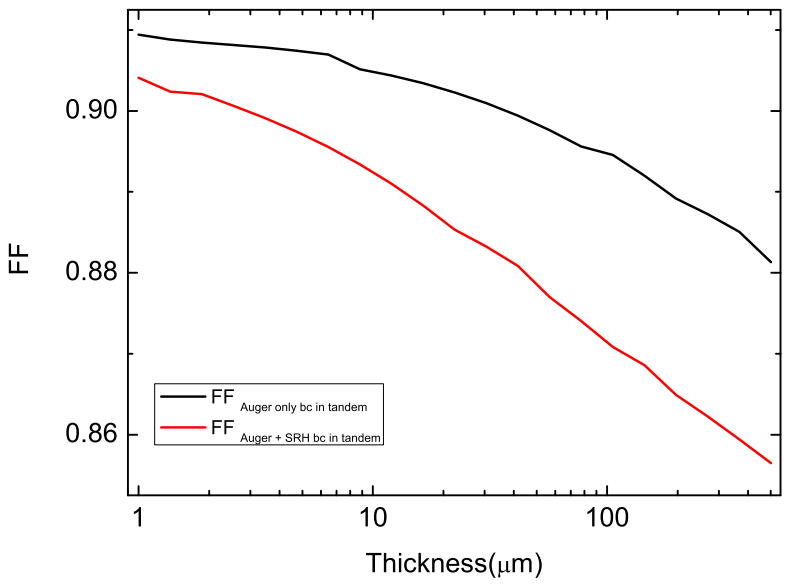

Figure 3.3.3: Analytic Fill Factor including recombination with $L_p = 3.47mm$.

diode equation and to experimental data [15], the efficiency of bottom cell including intrinsic (Auger) and extrinsic losses (SRH) and their simple sum. It is because of our unconstrained configuration: in a 4T structure the two solar cells are connected in series fig. 3.2.1 so the total efficiency is the simple sum of each one efficiency. We chose such a configuration because it does not require current matching which is quite hard to be studied from the analytic point of view since there are two active layers and a selective mirror.
Therefore, we can notice several behaviours:

- Increasing the importance of recombination, the optimal thickness of the silicon bottom cell decreases
- We cannot work on perovskite optimal thickness because we can access experimental values only for a 140 nm layer.

Hence, the efficiency of perovskite top cell is constant (we remind that the perovskite thickness is fixed to 140 nm) and it simply shifts the efficiency of silicon bottom cell to the efficiency of the tandem.
Recombination affects efficiency but its presence is more important for thick cells than for thin

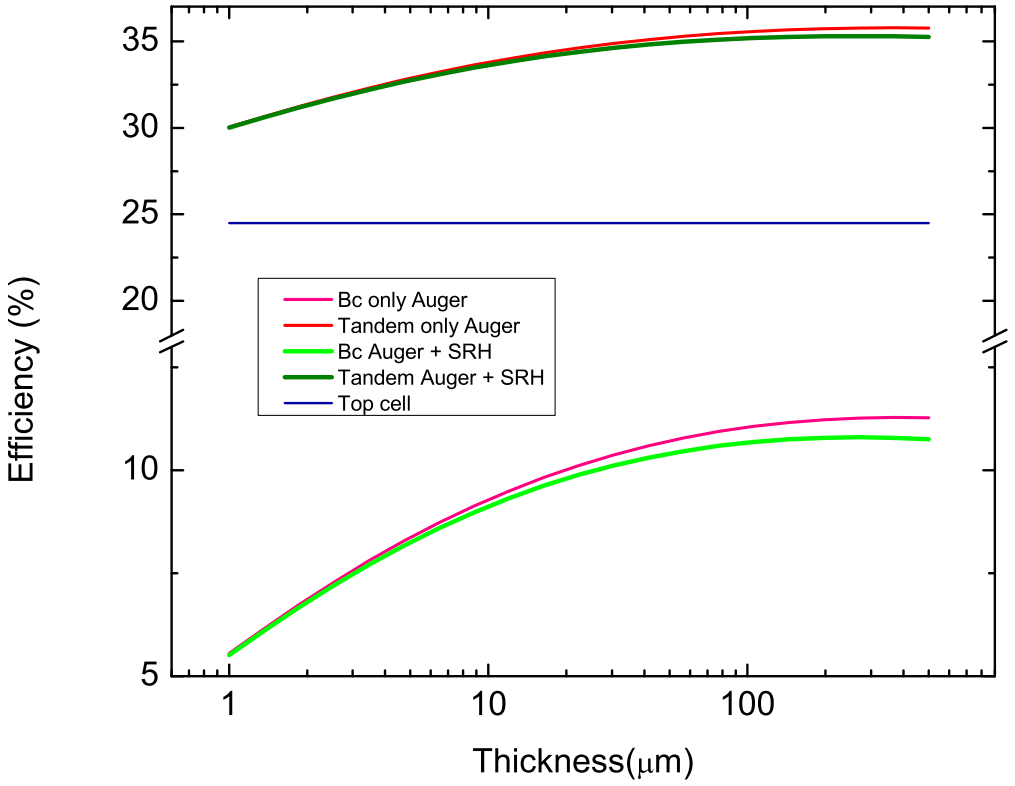

Figure 3.3.4: Efficiency limits for silicon-perovskite tandem cell. Blue line: efficiency of perovskite top cell. Pink line: efficiency of silicon bottom cell in the presence of only Auger recombination. Light green line: efficiency of silicon bottom cell in the presence of both Auger and SRH recombination. Red line: efficiency of the tandem system in the presence of only Auger recombination. Dark green line: efficiency of the tandem system in the presence of both Auger and SRH recombination.

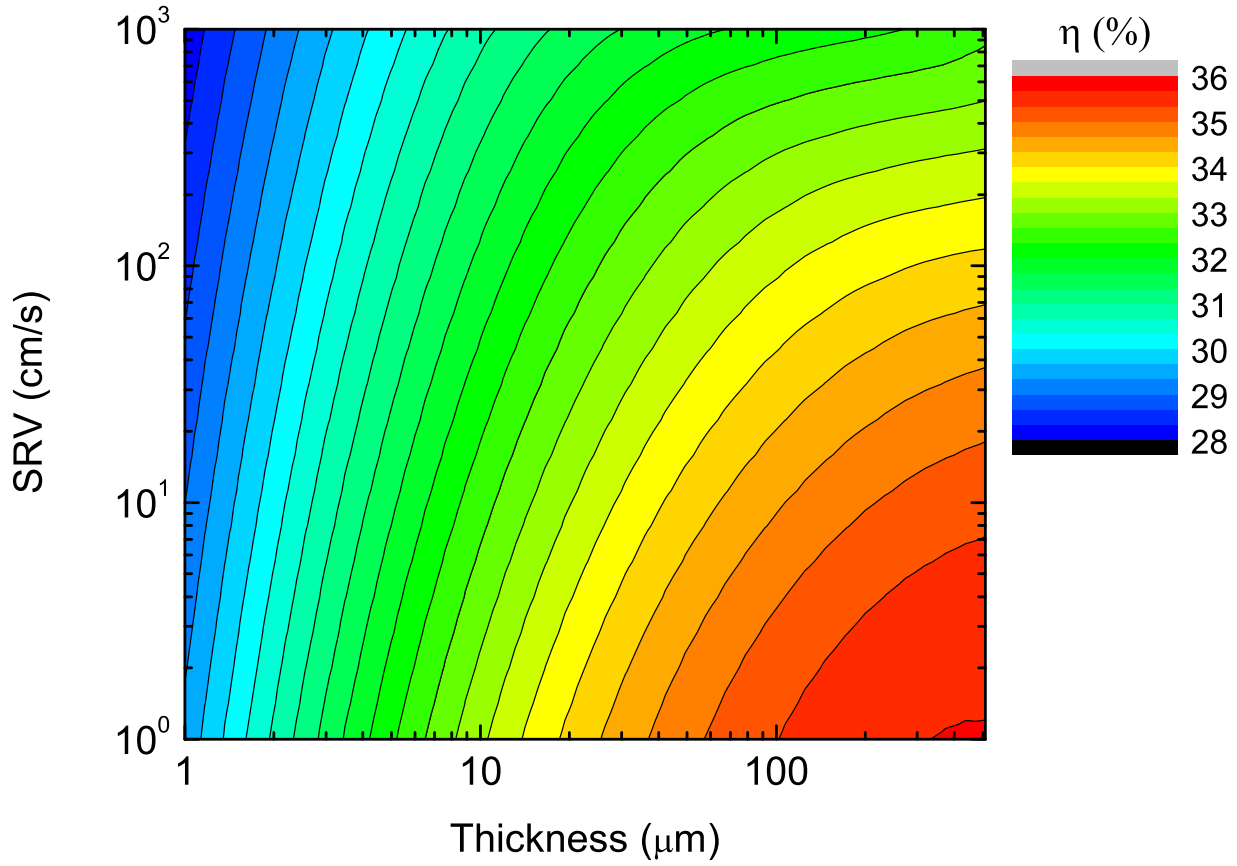

Figure 3.3.5: Analytic results including only Auger and SRV back recombination with $L_p = 3.47mm$

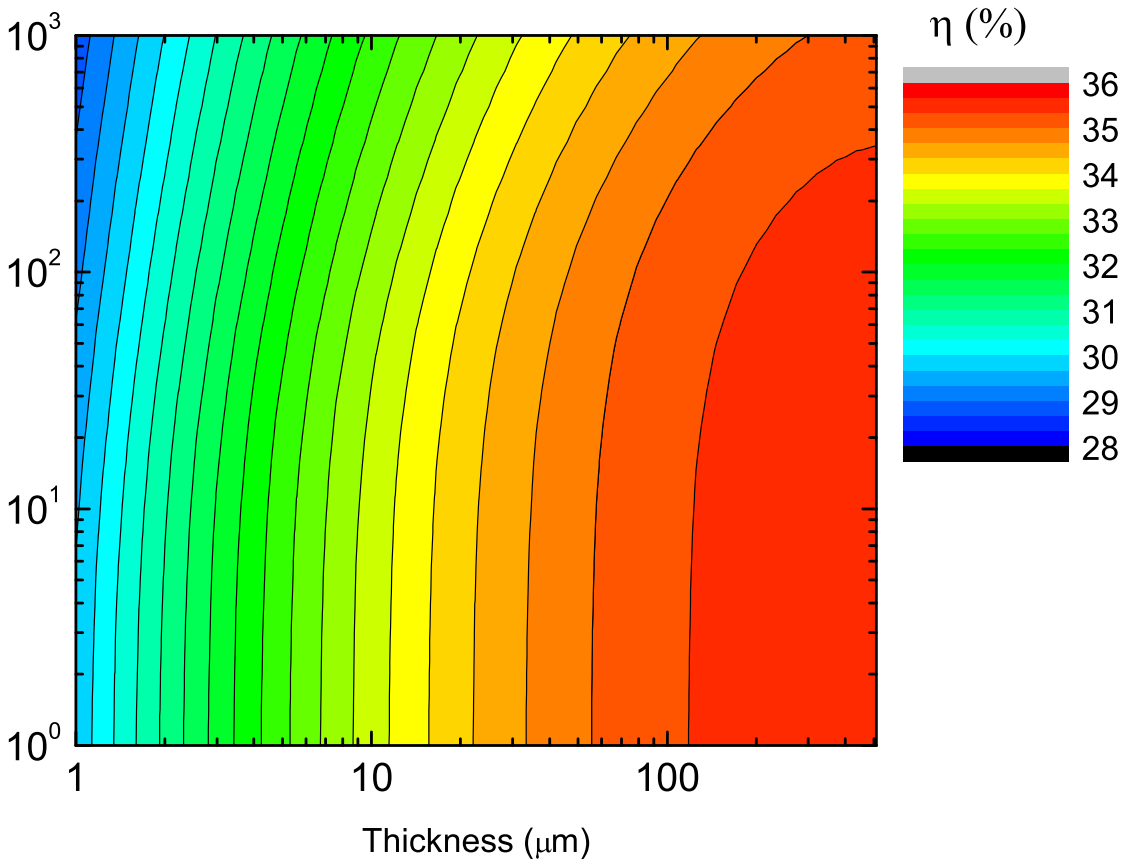

Figure 3.3.6: Efficiency of perovskite-silicon tandems including Auger and SRV front recombination with long $L_p = 3.47mm$

cells because bulk recombination is reduced for thin cells.
At a second stage, surface recombination has been taken into account and we studied it both with only Auger recombination and including bulk SRH.
We set different surface recombination velocities for the back and the front surfaces, to be able to study the separate effects occurring at the front and rear surfaces of the solar cell.
In fig. 3.3.5 we present efficiency of silicon/perovskite tandem as a function of both silicon bottom cell thickness and surface recombination in the bottom cell with only intrinsic bulk losses as Auger recombination and surface recombination. We use two log scales to show our results. The maximum possible efficiency is around 36%, which is obtained for $L_p = 3.47mm$. With this material quality the maximum efficiency can be achieved for the thickness range between 100 and $500\mu m$. In this case, back SRV should be below a few tens of cm/s.
In fig. 3.3.6 we have the same plot with the same diffusion length and the maximum possible efficiency is still around 36% even if we consider front surface recombination instead of back one. We can notice that the conditions for surface recombination at the front interface are relaxed: in this case, to achieve an efficiency of 36% we tolerate a slightly higher SRV. If we include also bulk recombination (SRH), as we did for the standalone solar cell, the total efficiency is a bit lower. For bulk transport losses, we assume Auger and SRH recombination. The maximum achievable efficiency is reduced to a certain value which depends on the diffusion length used to describe SRH. In fig. 3.3.7 and fig. 3.3.8 we present efficiency of the tandem as a function of silicon thickness and SR, but we use two different diffusion length for SRH recombination which have been used to calculate an effective diffusion length according to the equations reported at the beginning of this section.
The efficiency limits are around 35% for the higher diffusion length and around 34% for the lower one. In this case too the conditions for surface recombination at the front interface are relaxed since we tolerate also a few hundreds cm/s.

3.4 Toward higher efficiencies: band gap optimization

The most common perovskite absorber is methylammonium lead trihalide $CH_3NH_3PbX_3$, where X is a halogen ion such as I^-, Br^-, Cl^-, with an optical bandgap between $1.56eV$ and $2.3eV$ depending on halide content.
This motivates us to study the effect of **modifying the band gap** in order to determine the value of the optimal band gap for reaching the highest efficiency limits. We want to study how the band gap affects the total efficiency of the structure. However, ideally, one can select materials with optimum band gaps, but the choices are restricted for example by lattice mismatch and vastly different material growth conditions. As a consequence, it is important

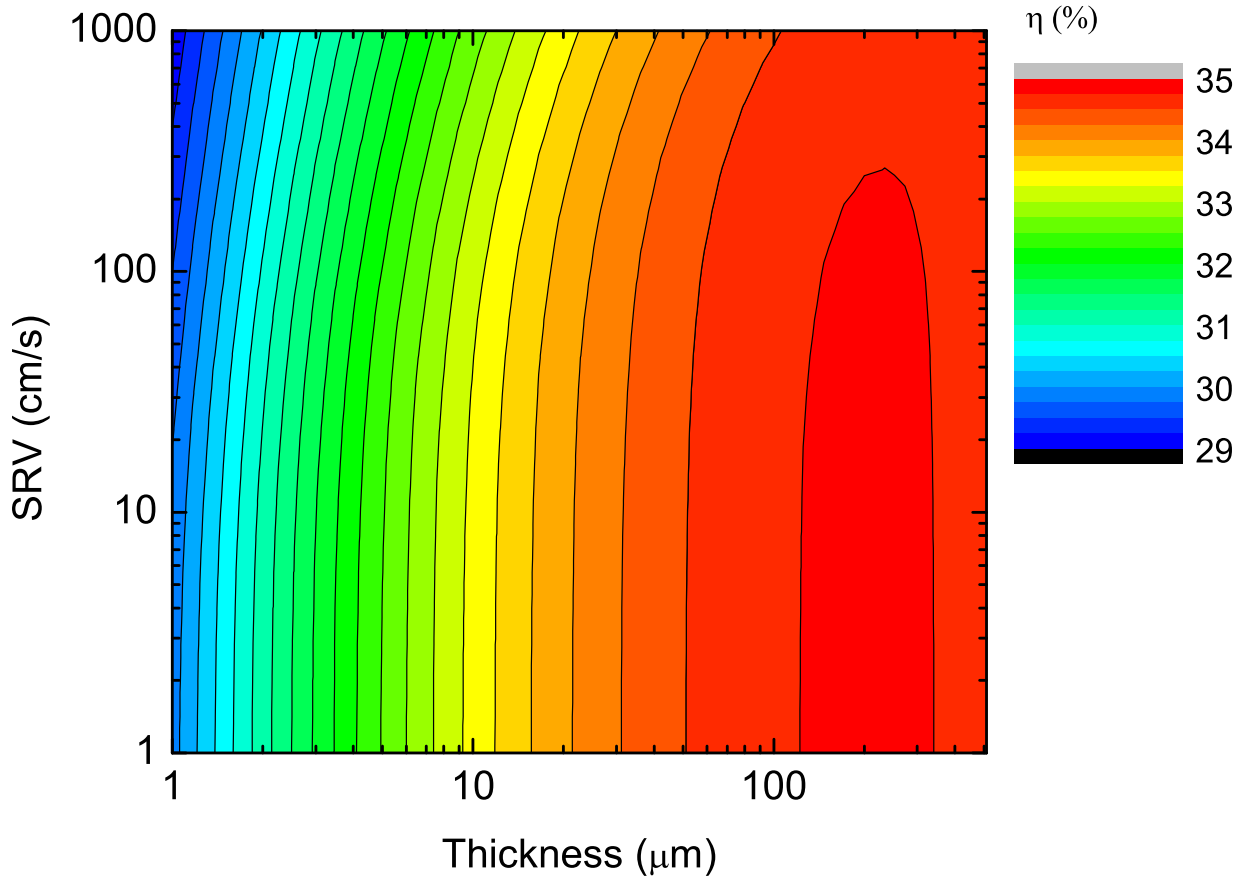

Figure 3.3.7: Efficiency of perovskite-silicon tandems including Auger, SRH and SRV front recombination and no back surface recombination. The diffusion length is the quasi neutral p region is set to $L_p = 1.78mm$

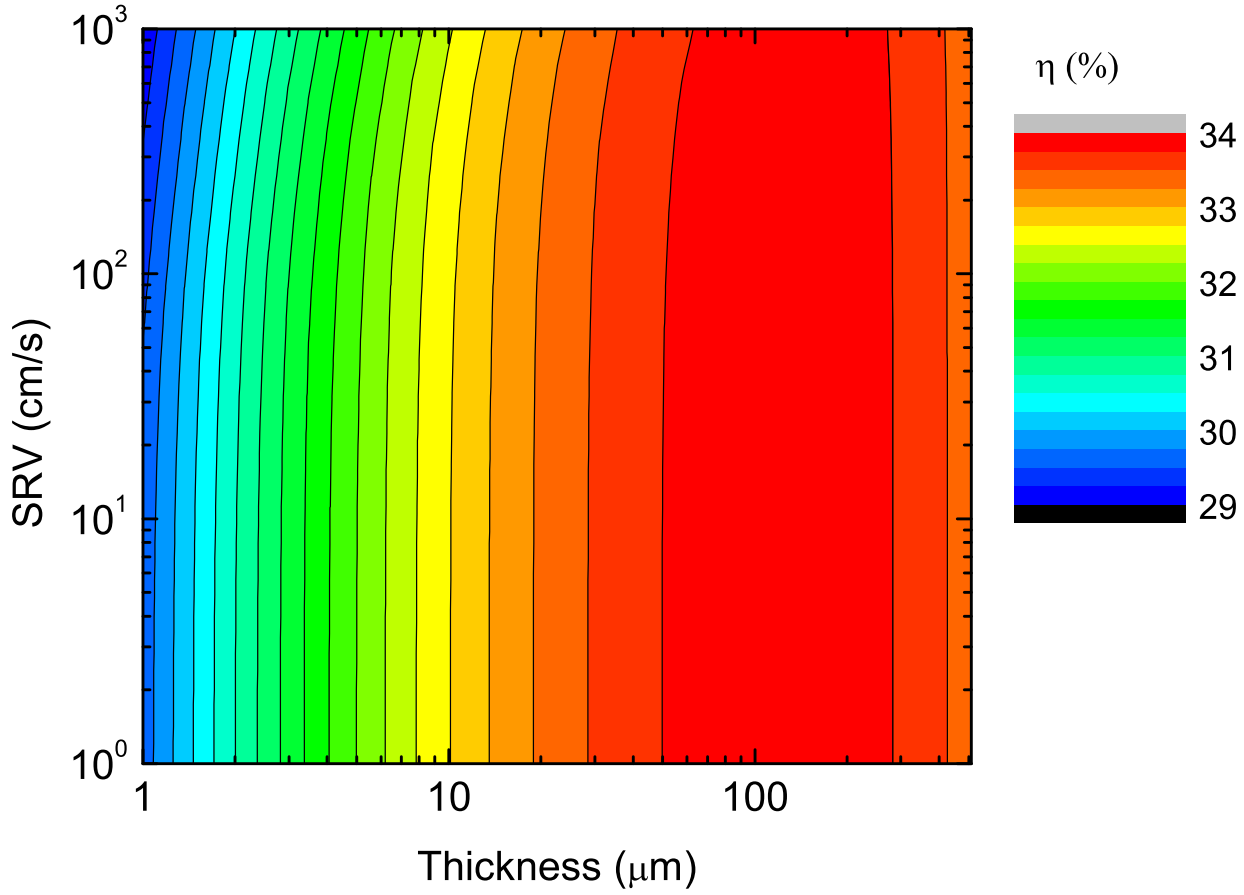

Figure 3.3.8: Efficiency of perovskite-silicon tandems including Auger, SRH and SRV front recombination and no back surface recombination. The diffusion length is the quasi neutral p region is set to $L_p = 0.675mm$.

to know the sensitivity of the efficiency of a solar cell stack to variations in the band gap of any of the solar cells.
Hence, we studied how the top cell efficiency depends on perovskite band gap modifying the energy gap from $1.55eV$ to $2.2eV$. We modified the absorption coefficient and the refractive index of perovskite according to [50] and then we changed the experimental J_{sc} for $1.56eV$ as:

$$J_0 = J_0(E_{gap,1.55}) \cdot e^{(-(E_{gap,1.55}-1.55)/k_BT)} \tag{3.4.1}$$

and, as a consequence,

$$V_oc = V_{oc}(E_{gap,1.55}) + (E_{gap,1.55} - 1.55)\,. \tag{3.4.2}$$

Following this model we calculate the efficiency of silicon/perosvkite tandems solar cell as a function of the bottom cell's thickness and of perovskite's band gap.
In fig. 3.4.1 we present the efficiency of silicon/perovskite tandem as a function of bottom cell's thickness using a log scale. In addition, there are several curves which differ from one to another according to the perovskite's band gap. For $E_g = 1.5$ eV and 110 μm thick bottom cell, we obtain the efficiency around 36.7%, which is in a very good agreement with calculations performed for the same parameters, reported in [15] (see Tab. 1 in the reference work). The highest efficiency, close to 40 %, is obtained for the perovskite band gap of 1.8 eV. This value of the optimal band gap is in agreement with the results presented by [28], concerning the efficiency limits of tandem solar cells (in particular, see Fig. 4(b) in the reference work).
In general, the detailed balance limit for unconstrained tandem stack with two cells is 45.7 % [51]. Yet, this limit excludes intrinsic Auger recombination. Moreover, the band gap of silicon is not exactly optimal for the bottom cell.
The higher the perovskite's band gap, the lower the optimal thickness of silicon bottom cell. This is due to absorption. With a higher perovskite band gap, the silicon bottom cell is required to absorb light at higher energy and a thinner silicon cell is required. On the contrary, if we use a lower value for the perovskite band gap (i.e. 1.55 eV) we need to increase absorption just above the silicon band gap and a thicker layer of silicon is required. This explains the slightly lower value we obtain for the efficiency limit with respect to [51].

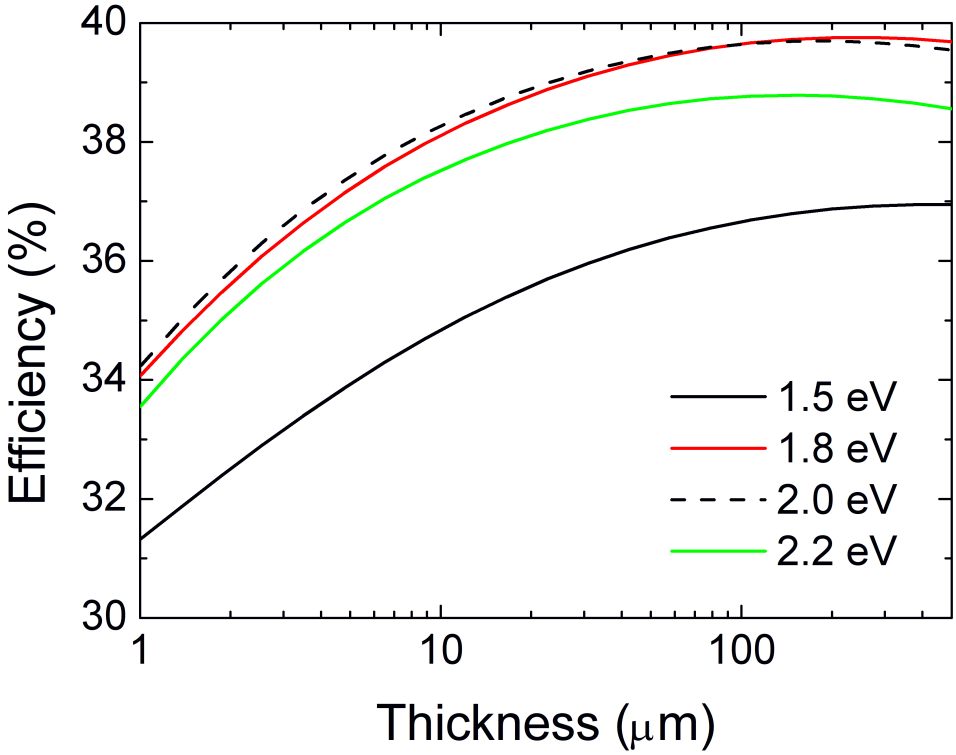

Figure 3.4.1: Efficiency of silicon/perovskite tandem solar cell as a function of perovskite band gap

Chapter 4

Further developments

In this last chapter we present a comparison between three different approaches to model the solar cell performance [52]. They are the diode equation, a generalization of the well-known Hovel model, and a complete device modelling. In each approach we implement a Lambertian light trapping, which is often considered as a benchmark for the optical design of solar cells. The generalized Hovel model can also be referred to as a previous model [14] including the effects of voltage for the short-circuit current. Here we are going to show briefly the analytic calculations which stand behind that new model.
It will be used to describe the silicon bottom cell both as a standalone cell and as a bottom cell in a tandem structure.

4.1 Ideal diode equation

First, we present the idealized diode equation method. The ideal diode equation is given by:

$$J(V) = J_{sc} - qwR(V) \tag{4.1.1}$$

where J_{sc} is the short-circuit current density calculated assuming unity electron-hole pair collection efficiency (i.e., it corresponds to the photogenerated current density), w is the cell thickness, and R is the total recombination rate per unit volume.
The short-circuit current density is given as

$$J_{sc} = \int q\frac{I(E)}{E}A(E)\,dE \tag{4.1.2}$$

where A(E) is the total absorption in the active layer, calculated using the Green's formalism in order to include light trapping. Moreover, I(E) is the spectral irradiance corresponding to

the AM1.5G solar spectrum in fig. 1.2.1. The integration is performed with respect to the whole spectral range corresponding to the solar spectrum.
Total recombination rate R is the sum of recombination rates is the bulk and at the surfaces. Bulk recombination rate R_{bulk} is related to the intrinsic Auger recombination and defect-based Shockley-Read-Hall (SRH) recombination. Here we assume that Auger recombination is the only bulk loss mechanism. To calculate R_{bulk} we use the parametrization recently reported by Richter et al. [22], i.e., eq. (20) in the reference work.
To include surface recombination in the diode equation, we calculate surface lifetime as [53]

$$\tau_s = \frac{w}{SRV} + \frac{4}{D}\left(\frac{w}{\pi}\right)^2 \tag{4.1.3}$$

where SRV is the surface recombination velocity and D is the diffusion constant. Here we assume that carriers recombine only at one surface (the rear one, as explained in previously), and the other surface is perfectly passivated. Then, the recombination rate at the surface is calculated as

$$R_{surf} = \frac{\Delta n}{\tau_s} \tag{4.1.4}$$

where Δn is the excess carrier concentration [22] (in this approach we assume that Δn at the surface is equal to Δn in the bulk).

4.2 The generalized Hovel model

In the second chapter we presented an electronic description of the silicon bottom cell which takes into account two important approximations: the superposition approximation and performing all calculations related to illumination at zero voltage. At a first stage we neglected the effects of voltage on the short-circuit current. This enters into the zero-order boundary condition

$$\Delta n(z = w_{scr} + w_n) = \frac{n_i^2}{N_a}(e^{qV/kT} - 1) \tag{4.2.1}$$

which has been reduced to:

$$\Delta n(z = w_{scr} + w_n) = 0\ . \tag{4.2.2}$$

Now, we are interested in considering the effects of voltage on the short-circuit current too [52]. Before the new calculation, let us first present the general structure of our solar cell and fix a specific reference frame. We propose a new formalism which does not depend on a specific base-emitter doped semiconductor: we just refer to base and emitter in general and they can be either n-doper or p-doped. In fig. 4.2.1 a schematic representation of a p-n junction solar cell

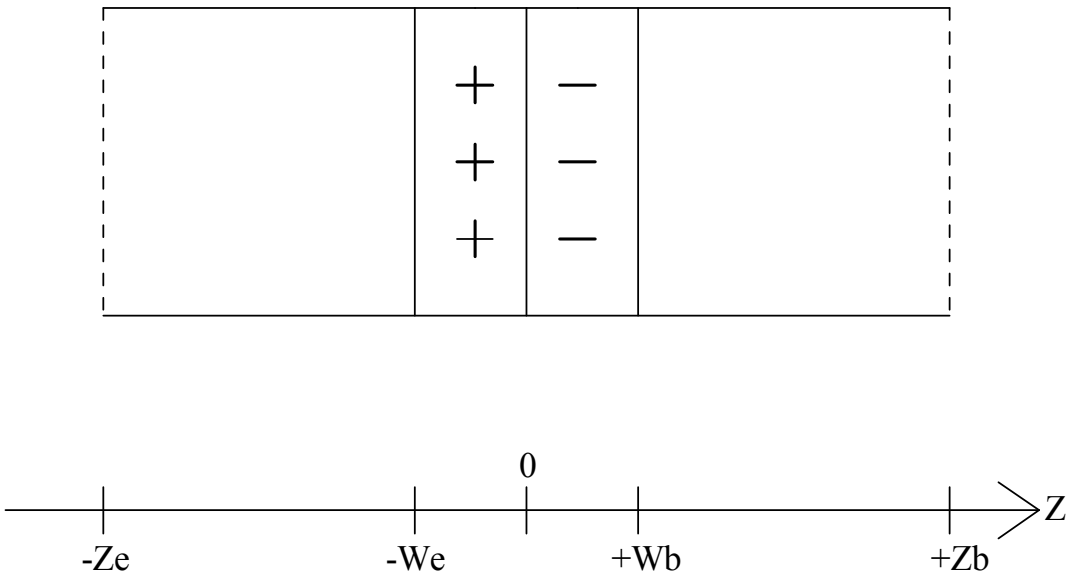

Figure 4.2.1: Solar cell with our reference frame. The total thickness of the cell is given by w, while w_{scr} refers to the thickness of the space charge region. W_e and W_b are the thickness of the quasi neutral regions.

is shown. The origin of the reference frame is put across the junction interface. We emphasize that the thickness of depleted regions in the SCR, denoted as w_E and w_B, have to be taken as voltage-dependent (eq. 1.1.38) with V_{bi} replaced by $V_{bi} - V$ in the present model, which is meant to be applicable for any voltage. The first step of modelling is the analytic solution of the diffusion equations for minority carriers. The presence of illumination impacts more minority carrier density then the majority one.
For minority carriers in the base with no electric field neither from applied voltage nor from potential drop across the junction, we have

$$D_B \frac{d^2 \Delta n_B}{dz^2} - \frac{\Delta n_B}{\tau_B} + g(z, E) = 0 \tag{4.2.3}$$

where D_B is the diffusion constant in the base. In the others part of this work we included SRH as the only recombination mechanisms in the short-circuit current, whilst in the dark current we put also Auger recombination. The primary reason of this choice is explained in chapter 2. Here we follow a different approach: since the drift-diffusion equations are solved at any voltage, we can consider a finite Auger diffusion length, so we have both SRH and Auger in dark current and short-circuit too using an effective diffusion constant.

As far as the emitter is concerned, the situation is not the same because of the thickness. In fact, with a very thin emitter Auger losses are negligible and we can deal with only SRH recombination.
The boundary condition for the above equation are

$$\Delta n_B(z = w_B) = \frac{n_i^2}{M_B}(e^{qV/kT} - 1) \tag{4.2.4}$$

where M_B means the majority carrier concentration in the base which is not only the doping, but it also takes into account the contribution from Δn, which depends on voltage and illumination. This helps us to move from a low-level injection condition to a high-level one. In the first case the contribution from majority carriers is given by the only doping, whilst in the second one we must add also the photogenerated majority carriers since their contribution is not negligible with respect to the doping level with our parameters.
We can carry on the low-level injection condition in two different ways: increasing the doping level or decreasing material quality rising the importance of SRH recombination by adding traps. In that way the photogenerated minority carriers will be affected more and more by trap-assisted recombination decreasing their concentration. It follows

$$D_B \frac{d\Delta n_B}{dz} = -S_B \Delta n_B \quad (z = z_B) \tag{4.2.5}$$

where S_{rec} refers to the surface velocity recombination in the base.
The carrier generation rate is given by a general formula:

$$g(z, E) = a_- e^{-\alpha_{lt}(z+z_E)} + a_+ e^{+\alpha_{lt}(z+z_E)} \tag{4.2.6}$$

where a_- and a_+ are

$$a_- = \frac{\alpha_{lt}\Phi_{AM1.5}}{1 - R_b e^{2\alpha_{lt}w}\left(1 - \frac{1}{n^2}\right)} \tag{4.2.7}$$

and they take into account light trapping.

$$a_+ = a_- \cdot R_b e^{2\alpha_{lt}w} \tag{4.2.8}$$

The general solution for this kind of differential equation can be written as:

$$\Delta n_B = A_B \cosh\left(\frac{z - w_B}{L_B}\right) + B_B \sinh\left(\frac{z - w_B}{L_B}\right) + \gamma_B(a_- e^{-\alpha_{lt}(z+z_E)} + a_+ e^{+\alpha_{lt}(z+z_E)}) \tag{4.2.9}$$

where $\gamma_B = \dfrac{L_B^2}{D_B(1-\alpha_{lt}^2 L_B^2)}$.

Implementing the two boundary conditions we find:

$$A_B = \frac{n_i^2}{N_B}(e^{qV/kT}-1) - \gamma_B(a_- e^{-\alpha_{lt}(w_B+z_E)} + a_+ e^{+\alpha_{lt}(w_B+z_E)}) \tag{4.2.10}$$

and

$$\begin{aligned} B_B = &-A_B\left(\frac{D_B}{L_B}\sinh(x_B) + S_B\cosh(x_B)\right) \\ &- \gamma_B\left(a_- e^{-\alpha_{lt}(w_B+z_E)}(S_B-\alpha_{lt}D_B) + a_+ e^{+\alpha_{lt}(w_B+z_E)}(S_B+\alpha_{lt}D_B)\right) / \\ &\left[\frac{D_B}{L_B}\cosh(x_B) + S_B\sinh(x_B)\right] \end{aligned} \tag{4.2.11}$$

where $x_B = \dfrac{z_B - w_B}{L_B}$.
Then we can calculate

$$J_B = qD_B\frac{d\Delta n_B}{dz}. \tag{4.2.12}$$

In the same way we can reproduce our calculations for the emitter:

$$D_E\frac{d^2\Delta n_E}{dz^2} - \frac{\Delta n_E}{\tau_E} + g(z,E) = 0 \tag{4.2.13}$$

where D_E is the diffusion constant in the emitter.
The boundary condition for the above equation are

$$\Delta n_E(z=-w_E) = \frac{n_i^2}{M_E}(e^{qV/kT}-1) \tag{4.2.14}$$

where M_E means the majority carrier concentration in the emitter which is not only the doping, but it also takes into account the contribution from Δn, which depends on voltage and illumination. and

$$D_E\frac{d\Delta n_E}{dz} = +S_E\Delta n_E \quad (z=-z_E) \tag{4.2.15}$$

where S_{rec} refers to the surface velocity recombination in the emitter.
The carrier generation rate is given by a general formula:

$$g(z,E) = a_- e^{-\alpha_{lt}(z+z_E)} + a_+ e^{+\alpha_{lt}(z+z_E)} \tag{4.2.16}$$

where a_- and a_+ are coefficients which take into account light trapping.
The general solution for this kind of differential equation can be written as:

$$\Delta n_E = A_E \cosh\left(\frac{-z-w_E}{L_E}\right) + B_E \sinh\left(\frac{-z-w_E}{L_E}\right) + \gamma_E(a_- e^{-\alpha_{lt}(z+z_E)} + a_+ e^{+\alpha_{lt}(z+z_E)}) \tag{4.2.17}$$

where $\gamma_E = \dfrac{L_E^2}{D_E(1-\alpha_{lt}^2 L_E^2)}$.

Implementing the two boundary conditions we find:

$$A_E = \frac{n_i^2}{N_E}(e^{qV/kT}-1) - \gamma_B(a_- e^{-\alpha_{lt}(-w_E+z_E)} + a_+ e^{+\alpha_{lt}(-w_E+z_E)}) \tag{4.2.18}$$

and

$$\begin{aligned} B_E = &-A_E\left(\frac{D_E}{L_E}\sinh(x_E) + S_E\cosh(x_E)\right) \\ &- \gamma_E\left(a_-(S_E-\alpha_{lt}D_E) + a_+(S_E-\alpha_{lt}D_E)\right) / \\ &\left[\frac{D_E}{L_E}\cosh(x_E) + S_E\sinh(x_E)\right] \end{aligned} \tag{4.2.19}$$

where $x_E = \dfrac{z_E - w_E}{L_B}$.
Then we can calculate

$$J_E = \int_0^\infty j_E(E,V)dE\ . \tag{4.2.20}$$

As far as the SCR is concerned, we must consider two different contributions: J_{gen} and J_{rec}.

$$J_{gen} = \int_0^\infty q j_{gen} dE \tag{4.2.21}$$

where

$$j_{gen} = \int_{-w_E}^{w_B} q g(z,E)dz \tag{4.2.22}$$

which gives

$$j_{gen} = q/\alpha_{lt}\left(a_-(e^{-\alpha_{lt}(-w_E+z_E)} - e^{-\alpha_{lt}(w_E+z_E)}) + a_+(e^{+\alpha_{lt}(w_E+z_E)} - e^{-\alpha_{lt}(-w_E+z_E)})\right). \tag{4.2.23}$$

On the other hand, if we consider J_{rec} we must calculate

$$J_{rec}(V) = \frac{q n_i (w_E+w_B)}{\sqrt{\tau_E \tau_B}} \frac{2\sinh(qV/2kT)\xi}{q(V-V_{bi})/kT} \tag{4.2.24}$$

according to [1] where ξ tends to $\pi/2$ for large bias.
The total current in the SCR, for a given voltage, is given as

$$J_{SCR}(V) = \int_0^\infty j_{gen}(E)dE - J_{rec}(V) \ . \tag{4.2.25}$$

Finally, the JV characteristic of the device is calculated as a sum of the three contributing currents:

$$J(V) = J_E(V) + J_B(V) + J_{SCR}(Vvoltage) \ . \tag{4.2.26}$$

We note that using the notation above (index "B" for the base, and "E" for the emitter), we formulate the model in the most general way, i.e., the type of doping in each region is not explicitly defined. Therefore, the model can be used to study p-n, as well as n-p architectures. Using such a model we obtain a better agreement between that analytic model (see fig. 4.3.1), which we called *generalized Hovel model* (we included light trapping in the Hovel's framework).

4.3 Solar cell modelling: from simplicity to complexity

In the generalized Hovel model, we first analytically calculate the Lambertian photogeneration rate using 2.1.3. Then, the photogeneration rate is integrated with respect to energy (over the solar spectrum) and used as the generation term in the drift-diffusion equations, which are solved using Finite-Element method (FEM). We solve the equations using FEM implemented in the commercial device simulator Silvaco Atlas [39]. This approach is analogous to the one described in our previous work [14].
In the increasing order of complexity we have discussed [52]

- **The diode equation**: the biggest advantages of this method are speed and simplicity: typically the calculations are orders of magnitude faster, comparing to the other two methods. The main limitation is that the carrier collection efficiency is assumed to be unity, which is not the case when bulk recombination impacts the collection efficiency.

- **The generalized Hovel model**: in terms of the computational speed it is intermediate between the diode equation and the complete device modelling. It removes the previous assumption that carrier collection efficiency is always unity. The main limitation is that the method is not suitable to model cells operating in the high injection regime when surface recombination is included.

- **Complete device modelling — Finite Element method**: as long as the conditions for convergence are fulfilled (e.g., proper finite-element mesh and voltage step), this

method can be consider as exact. The main limitation are the computational speed and its costs.

In all three approaches we have used the same material parameters and physical models describing the transport of carriers. To include intrinsic Auger recombination, we use the parametrization recently reported by Richter et al. [22]. Moreover, we neglect free carrier absorption, as it has only a minor impact on the cell performance [20]. Finally, we neglect photon recycling and radiative recombination, as these two effects are likely to compensate each other [40].
We take intrinsic carrier concentration equal to $n_i = 9.65 \cdot 10^9 cm^{-3}$, and we include band gap narrowing (BGN) according to the model by Schenk [19]. The diffusion coefficient in the p-type base is equal to $D_B = 25 cm^2/s$ and in the n-type emitter $D_E = 12.5 cm^2/s$. We assume optimal doping values for this structure [40] the emitter doping is equal to $N_d = 1.5 \cdot 10^{18} cm^{-3}$, and the base doping is equal to $N_a = 10^{16} cm^{-3}$. We also take a 5 nm thick emitter to minimise recombination losses in this heavily doped layer.

The panels in fig. 4.3.1 show an excellent agreement between the results obtained using all the three methods [52]. As long as the diode equation is considered, we essentially reproduce the results presented in [22], except that we neglect radiative recombination and photon recycling. The only (small) discrepancy is in the calculations of V_{oc} and FF for very thin cells. The opposite trends of V_{oc} and J_{sc} result in an optimal absorber thickness. The optimal thickness is very sensitive to the input parameters, and even a small change can substantially shift the nominal optimal thickness. In panel fig. 4.3.1, figure (d) shows that the maximum achievable efficiency is around 29.2%. This value is slightly higher than the maximum efficiency calculated in our previous contribution [40]. This is because previously we had assumed surface recombination velocity equal to 1 cm/s.
This makes us confident in applying such a new improvement to the tandem model in order to get clearer and more precise results for efficiency limits. In [52] we report a complete study including surface recombination for standalone solar cells and we have used a combination of the diode equation and the Hovel model to calculate the efficiency limits of tandem silicon-perovskite solar cells. We have extrapolated the experimental data available in the literature to consider perovskite cells with different energy band gap, which is important in the synthesis of new materials.

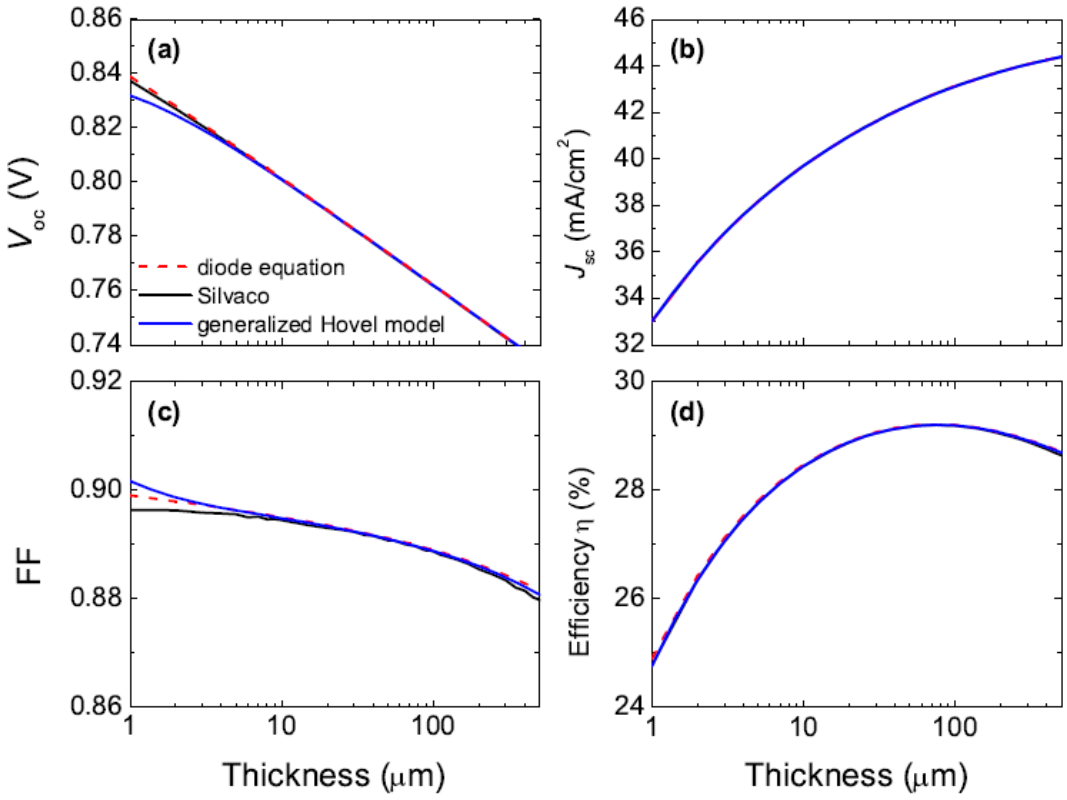

Figure 4.3.1: (a) Open-circuit voltage V_{oc} , (b) short-circuit current J_{sc} , (c) fill factor FF, and (d) efficiency η as a function of the absorber thickness. The red dashed lines refer to the results obtained using the diode equation, the black solid lines refer to the results obtained by numerically solving the drift-diffusion equations using finite- element method, the blue solid lines present results obtained using the generalized Hovel model. The base doping is equal to $N_a = 10^{16} cm^{-3}$. We include only intrinsic Auger recombination, and assume that both surfaces are perfectly passivated (i.e. there is no surface recombination). Simulations have been calculated by Dr. P. Kowalczewski (Dept. of Physics - University of Pavia.

Conclusions

Our primary goal was to extend the analytic model presented in [14], to the case of a silicon/perovskite tandem system to calculate the efficiency limits of such a photovoltaic device. We wanted to deeply investigate the role of light trapping, recombination and perovskite top cell band gap.
Part of this work has been done in close collaboration with Piotr Kowalczewski, who perfomed the Silvaco-ATLAS simulations that have been used for comparison with the analytic model. Here I shall try to emphasize my own contributions in this collaborative work.

At first I studied in details the analytic model for the silicon bottom cell and I implemented it to determine the efficiency limits of the bottom cell. Then I extended it by calculating the quasi-fermi levels and the carrier concentrations analytically and I also validated my results against the numerical simulator Silvaco ATLAS. Several recombination mechanisms have been included in this study in order to find out the most efficient parameters for a silicon solar cell in the presence of light trapping. I studied the Auger and the trap-assisted recombination too, including surface recombination in both cases.
I calculated that the maximum efficiency for a standalone silicon bottom cell in the presence of light trapping is around 29% with only Auger recombination and 27% if we include also SRH. I studied surface recombination separately in order to point out what surface loss impacts more on the efficiency. It is the back one.

Then, I modified and applied the Green's formalism for a Lambertian scatterer to study the optical part of a tandem solar cells system in order to calculate the carrier generation rate for such a system in the presence of light trapping. I neglected the absorption of the selective mirror, but I took into account the three-layer tandem structure to calculate the absorption in the silicon bottom cell. I used this function as the source term in the partial differential equations of the old model which describes charge transport in the quasi-neutral regions to obtain the short-circuit current. We decided to treat perovksite top cell as an ideal diode using published

values for the V_{oc} because of the lack of theory and models involving perovskite structures.
We found several interesting results: taking into account three different recombination mechanisms (Auger, SRH and surface recombination). We calculated that the efficiency limits for such a tandem are around 36 % if we neglect material imperfections in the bulk and consider only Auger and surface recombination, but they fall by 1-2 % if we include SRH.
Moreover, we know that the thermodynamic limit is around 33% for a single junction and around 42% for a double junction and since we also proved that the thermodynamic limit for a single silicon solar cell with intrinsic losses falls down to 29%, we must focus on the high band gap top cell. We calculated that, including Auger and trap-assisted recombination, the most convenient perovskite band gap is around 1.8 eV ($\approx 40\%$) since for higher values the efficiency drops rapidly. The higher the perovskite's band gap, the lower the optimal thickness of silicon bottom cell. This is due to absorption. With a higher perovskite band gap, the silicon bottom cell is required to absorb light at higher energy and a thinner silicon cell is required. On the contrary, if we use a lower value for the perovskite band gap (i.e. 1.55 eV) we need to increase absorption just above the silicon band gap and a thicker layer of silicon is required.

I also developed a new analytic model for the silicon bottom cell which takes into account the effects of a finite voltage when we solve drift-diffusion equation to obtain the short-circuit current. It has already been implemented and its agreement with Silvaco becomes even better. This makes us confident in applying such a new improvement to the tandem model in order to get clearer and more precise results for efficiency limits.

In [52] we report a complete study including surface recombination for standalone solar cells and we have used a combination of the diode equation and the Hovel model to calculate the efficiency limits of tandem silicon-perovskite solar cells. We have extrapolated the experimental data available in the literature to consider perovskite cells with different energy band gap, which is important in the synthesis of new materials.

Acknowledgements

First of all, I am extremely grateful to both my supervisors: Prof.ssa Beatrice Fraboni and Prof. Lucio Claudio Andreani. The former for her continuous encouragements, practical support and advice during my studies, from the bachelor thesis to my master one. The latter for having accepted me in his reasearch group and for having always supervised all of my work with care, helpfulness and a great patience. All of your comments, advice and suggestions really inspired me and clarified many subtle points during this work.
Working with the Photonics and Nanostructure research group at the University of Pavia has been a challenging, stimulating experience and a real pleasure. Although I am really grateful to everyone of you, a heartfelt thanks goes to my collegues Dr. Piotr A. Kowalczewski and Dr. Angelo Bozzola: thanks for our long computational trainee, physical discussions and for continuous checking of every single development of my work.
I also want to thank Prof.ssa Elisa Ercolessi for her precious thoughts during my master degree and her comprehension, for reading the manuscript and encouraging me to start such a project. For the same last reason a special thank goes to both Prof. Luca Ciotti, Director of the Collegio Superiore of Bologna, and Prof. Andrea Belvedere, Head of Collegio Ghislieri in Pavia, for their cooperation: without your personal help and support this work would not have been possible.

List of Figures

Bibliography

[1] J. Nelson, *The Physics of Solar Cells* (Imperial College Press, London, 2003). 11, 15, 20, 24, 30, 42, 51, 91

[2] T. Repmann, B. Sehrbrock, C. Zahren, H. Siekmann, and B. Rech, "Microcrystalline silicon thin film solar modules on glass," Solar energy materials and solar cells **90**, 3047–3053 (2006). 11

[3] K. Yamamoto, M. Yoshimi, Y. Tawada, Y. Okamoto, A. Nakajima, and S. Igari, "Thin-film poly-si solar cells on glass substrate fabricated at low temperature," Applied Physics A **69**, 179–185 (1999). 11

[4] M. Bazilian, I. Onyeji, M. Liebreich, I. MacGill, J. Chase, J. Shah, D. Gielen, D. Arent, D. Landfear, and S. Zhengrong, "Re-considering the economics of photovoltaic power," Renewable Energy **53**, 329–338 (2013). 11

[5] W. Shockley and H. J. Queisser, "Detailed balance limit of efficiency of p-n junction solar cells," Journal of Applied Physics **32**, 510–519 (1961). 12, 27, 29, 40, 99

[6] G. Cody, T. Tiedje, B. Abeles, B. Brooks, and Y. Goldstein, "Disorder and the optical-absorption edge of hydrogenated amorphous silicon," Physical Review Letters **47**, 1480 (1981). 12

[7] R. King, D. Law, K. Edmondson, C. Fetzer, G. Kinsey, H. Yoon, R. Sherif, and N. Karam, "40% efficient metamorphic gainp/gainas/ge multijunction solar cells," Applied physics letters **90**, 183516–183900 (2007). 12

[8] M. S. Leite, R. L. Woo, J. N. Munday, W. D. Hong, S. Mesropian, D. C. Law, and H. A. Atwater, "Towards an optimized all lattice-matched inalas/ingaasp/ingaas multijunction solar cell with efficiency¿ 50%," Applied Physics Letters **102**, 033901 (2013). 12

[9] B. N. E. Finance, "Renewable energy now cheaper than new fossil fuels in australia," Bloomberg New Energy Finance (2013). 12

[10] T. P. White, N. N. Lal, and K. R. Catchpole, "Tandem solar cells based on high-efficiency c-si bottom cells: top cell requirements for¿ 30% efficiency," Photovoltaics, IEEE Journal of **4**, 208–214 (2014). 12

[11] C. Battaglia, C.-M. Hsu, K. Söderström, J. Escarré, F.-J. Haug, M. Charrieére, M. Boccard, M. Despeisse, D. T. L. Alexander, M. Cantoni, Y. Cui, and C. Ballif, "Light trapping in solar cells: can periodic beat random?" ACS Nano **6**, 2790–2797 (2012). 12, 31

[12] C. Rockstuhl, S. Fahr, F. Lederer, F.-J. Haug, T. Söderström, S. Nicolay, M. Despeisse, and C. Ballif, "Light absorption in textured thin film silicon solar cells: A simple scalar scattering approach versus rigorous simulation," Applied Physics Letters **98**, 051102 (2011). 12

[13] M. A. Green, "Lambertian light trapping in textured solar cells and light-emitting diodes: analytical solutions," Progress in Photovoltaics: Research and Applications **10**, 235–241 (2002). 12, 31, 32, 33, 69

[14] A. Bozzola, P. Kowalczewski, and L. Andreani, "Towards high efficiency thin-film crystalline silicon solar cells: The roles of light trapping and non-radiative recombinations," Journal of Applied Physics **115**, 094501 (2014). 12, 13, 32, 36, 85, 91, 95

[15] P. Loper, B. Niesen, S.-J. Moon, S. Martin de Nicolas, J. Holovsky, Z. Remes, M. Ledinsky, F.-J. Haug, J.-H. Yum, S. De Wolf *et al.*, "Organic–inorganic halide perovskites: Perspectives for silicon-based tandem solar cells," Photovoltaics, IEEE Journal of **4**, 1545–1551 (2014). 12, 13, 63, 67, 68, 70, 76, 83

[16] M. Liu, M. B. Johnston, and H. J. Snaith, "Efficient planar heterojunction perovskite solar cells by vapour deposition," Nature **501**, 395–398 (2013). 13, 64, 67, 101

[17] "Solar radiation maps," http://solargis.info/doc/free-solar-radiation-maps-GHI. 24

[18] P. Kowalczewski, M. Liscidini, and L. C. Andreani, "Light trapping in thin-film solar cells with randomly rough and hybrid textures," Optics Express **21**, A808–A820 (2013). 29, 31

[19] P. P. Altermatt, A. Schenk, F. Geelhaar, and G. Heiser, "Reassessment of the intrinsic carrier density in crystalline silicon in view of band-gap narrowing," Journal of Applied Physics **93**, 1598–1604 (2003). 30, 35, 55, 92

[20] T. Tiedje, E. Yablonovitch, G. D. Cody, and B. G. Brooks, "Limiting efficiency of silicon solar cells," IEEE Transactions on Electron Devices **31**, 711–716 (1984). 30, 55, 92

[21] M. J. Kerr, A. Cuevas, and P. Campbell, "Limiting efficiency of crystalline silicon solar cells due to Coulomb-enhanced Auger recombination," Progress in Photovoltaics: Research and Applications **11**, 97–104 (2003). 30

[22] A. Richter, M. Hermle, and S. Glunz, "Reassessment of the limiting efficiency for crystalline silicon solar cells," IEEE Journal of Photovoltaics **3**, 1184–1191 (2013). 30, 45, 54, 56, 74, 86, 92

[23] K. Söderström, G. Bugnon, F.-J. Haug, S. Nicolay, and C. Ballif, "Experimental study of flat light-scattering substrates in thin-film silicon solar cells," Solar Energy Materials and Solar Cells **101**, 193–199 (2012). 30

[24] M. Boccard, C. Battaglia, S. Hänni, K. Söderström, J. Escarré, S. Nicolay, F. Meillaud, M. Despeisse, and C. Ballif, "Multiscale transparent electrode architecture for efficient light management and carrier collection in solar cells," Nano Letters **12**, 1344–1348 (2012). 30, 69

[25] C. Battaglia, M. Boccard, F.-J. Haug, and C. Ballif, "Light trapping in solar cells: When does a lambertian scatterer scatter lambertianly?" Journal of Applied Physics **112**, 094504 (2012). 30

[26] H. Sai, K. Saito, N. Hozuki, and M. Kondo, "Relationship between the cell thickness and the optimum period of textured back reflectors in thin-film microcrystalline silicon solar cells," Applied Physics Letters **102**, 053509 (2013). 30

[27] C. Trompoukis, O. El Daif, P. Pratim Sharma, H. Sivaramakrishnan Radhakrishnan, M. Debucquoy, V. Depauw, K. Van Nieuwenhuysen, I. Gordon, R. Mertens, and J. Poortmans, "Passivation of photonic nanostructures for crystalline silicon solar cells," Progress in Photovoltaics: Research and Applications (2014). 30, 31

[28] F. Meillaud, A. Shah, C. Droz, E. Vallat-Sauvain, and C. Miazza, "Efficiency limits for single-junction and tandem solar cells," Solar energy materials and solar cells **90**, 2952–2959 (2006). 30, 83

[29] A. Bozzola, M. Liscidini, and L. C. Andreani, "Broadband light trapping with disordered photonic structures in thin-film silicon solar cells," Progress in Photovoltaics: Research and Applications (2013). 31

[30] M. Ghebrebrhan, P. Bermel, Y. Avniel, J. D. Joannopoulos, and S. G. Johnson, "Global optimization of silicon photovoltaic cell front coatings," Optics express **17**, 7505–7518 (2009). 31

[31] A. Maradudin and T. Michel, "The transverse correlation length for randomly rough surfaces," Journal of Statistical Physics **58**, 485–501 (1990). 31

[32] E. Yablonovitch, "Statistical ray optics," JOSA **72**, 899–907 (1982). 31

[33] E. Yablonovitch and G. D. Cody, "Intensity enhancement in textured optical sheets for solar cells," Electron Devices, IEEE Transactions on **29**, 300–305 (1982). 31, 37

[34] A. Bozzola, M. Liscidini, and L. C. Andreani, "Photonic light-trapping versus lambertian limits in thin film silicon solar cells with 1D and 2D periodic patterns," Optics Express **20**, A224–A244 (2012). 31

[35] A. Abass, C. Trompoukis, S. Leyre, M. Burgelman, and B. Maes, "Modeling combined coherent and incoherent scattering structures for light trapping in solar cells," Journal of Applied Physics **114**, 033101 (2013). 31

[36] O. Isabella, F. Moll, J. Krč, and M. Zeman, "Modulated surface textures using zinc-oxide films for solar cells applications," Physica Status Solidi (a) **207**, 642–646 (2010). 31

[37] G. Gomard, R. Peretti, E. Drouard, X. Meng, and C. Seassal, "Photonic crystals and optical mode engineering for thin film photovoltaics," Optics Express **21**, A515–A527 (2013). 31

[38] R. Brendel, *Thin-film crystalline silicon solar cells: physics and technology* (John Wiley & Sons, 2011). 38

[39] "Silvaco Atlas Manual," http://www.silvaco.com/products/ tcad/device_simulation/atlas/atlas.html (2014). 52, 91, 100

[40] P. Kowalczewski and L. C. Andreani, "Towards the efficiency limits of silicon solar cells: How thin is too thin?" Solar Energy Materials and Solar Cells **143**, 260–280 (2015). 58, 59, 61, 92

[41] H.-S. Kim, C.-R. Lee, J.-H. Im, K.-B. Lee, T. Moehl, A. Marchioro, S.-J. Moon, R. Humphry-Baker, J.-H. Yum, J. E. Moser *et al.*, "Lead iodide perovskite sensitized all-solid-state submicron thin film mesoscopic solar cell with efficiency exceeding 9%," Scientific reports **2** (2012). 63

[42] S. D. Stranks, G. E. Eperon, G. Grancini, C. Menelaou, M. J. Alcocer, T. Leijtens, L. M. Herz, A. Petrozza, and H. J. Snaith, "Electron-hole diffusion lengths exceeding 1 micrometer in an organometal trihalide perovskite absorber," Science **342**, 341–344 (2013). 63

[43] M. M. Lee, J. Teuscher, T. Miyasaka, T. N. Murakami, and H. J. Snaith, "Efficient hybrid solar cells based on meso-superstructured organometal halide perovskites," Science **338**, 643–647 (2012). 64

[44] P. Docampo, J. M. Ball, M. Darwich, G. E. Eperon, and H. J. Snaith, "Efficient organometal trihalide perovskite planar-heterojunction solar cells on flexible polymer substrates," Nature communications **4** (2013). 64

[45] P. Löper, S.-J. Moon, S. M. De Nicolas, B. Niesen, M. Ledinsky, S. Nicolay, J. Bailat, J.-H. Yum, S. De Wolf, and C. Ballif, "Organic–inorganic halide perovskite/crystalline silicon four-terminal tandem solar cells," Physical Chemistry Chemical Physics **17**, 1619–1629 (2015). 65

[46] C. D. Bailie, M. G. Christoforo, J. P. Mailoa, A. R. Bowring, E. L. Unger, W. H. Nguyen, J. Burschka, N. Pellet, J. Z. Lee, M. Grätzel *et al.*, "Semi-transparent perovskite solar cells for tandems with silicon and cigs," Energy & Environmental Science **8**, 956–963 (2015). 66

[47] J. P. Mailoa, C. D. Bailie, E. C. Johlin, E. T. Hoke, A. J. Akey, W. H. Nguyen, M. D. McGehee, and T. Buonassisi, "A 2-terminal perovskite/silicon multijunction solar cell enabled by a silicon tunnel junction," Applied Physics Letters **106**, 121105 (2015). 66

[48] M. Filipič, P. Löper, B. Niesen, S. De Wolf, J. Krč, C. Ballif, and M. Topič, "Ch 3 nh 3 pbi 3 perovskite/silicon tandem solar cells: characterization based optical simulations," Optics express **23**, A263–A278 (2015). 66

[49] B. W. Schneider, N. N. Lal, S. Baker-Finch, and T. P. White, "Pyramidal surface textures for light trapping and antireflection in perovskite-on-silicon tandem solar cells," Optics express **22**, A1422–A1430 (2014). 66

[50] N. N. Lal, T. P. White, and K. R. Catchpole, "Optics and light trapping for tandem solar cells on silicon," Photovoltaics, IEEE Journal of **4**, 1380–1386 (2014). 71, 83, 101

[51] A. S. Brown and M. A. Green, "Detailed balance limit for the series constrained two terminal tandem solar cell," Physica E: Low-dimensional Systems and Nanostructures **14**, 96–100 (2002). 83

[52] P. Kowalczewski, L. Redorici, A. Bozzola, and L. C. Andreani, "Silicon solar cells reaching the efficiency limits: from simple to complex modelling," submitted to Journal of Optics (2015). 85, 86, 91, 92, 96

[53] A. Sproul, "Dimensionless solution of the equation describing the effect of surface recombination on carrier decay in semiconductors," Journal of Applied Physics **76**, 2851–2854 (1994). 86